

Long Term Durability of Glass Reinforced Composites

Jason J. Cain

Dissertation submitted to the faculty of the Virginia Polytechnic Institute and State University in
partial fulfillment of the requirements for the degree of

Doctor of Philosophy In
Engineering Mechanics

Scott W. Case
John J. Lesko
Michael W. Hyer
Saad A. Ragab
Judy S. Riffle

April 4th, 2008
Blacksburg, Virginia

Keywords: Composite, Durability, FRP, R-ratio, Fatigue, Hygrothermal

Copyright 2008 Jason Cain

Long Term Durability of Glass Reinforced Composites

Jason J. Cain

ABSTRACT

This dissertation discusses topics related to the performance and long-term durability of glass-reinforced composites.

The first portion of this dissertation describes work to assess the effect that post-curing has on widely used E-glass/vinyl-ester composites (E-glass/Derakane 510-A and E-glass/Derakane 8084). It is shown that post-curing can have significant positive effects on the initial material properties of glass-reinforced vinyl ester composites. Furthermore, the post-cure of 82°C for four hours stabilizes the matrix, and as such reduces matrix-related material property evolution. By stopping or nearly stopping material property evolution due to matrix curing over time, the post-cure regime isolates and allows the study of other time-dependent effects, such as fatigue or hygrothermal degradation, and aids designers by establishing an unchanging base set of initial (undamaged) material design properties.

The second portion of this dissertation discusses the effects that mean stress and R-ratio have on the fatigue performance of the same material. Qualitative and quantitative differences are seen in the performance as a function of the loading ratio. A residual strength based life prediction model developed at Virginia Tech is applied to the fatigue data, characterizing the material under constant-amplitude loading. Three curve-fitting parameters are then used along with the model to predict variable-amplitude fatigue lives, with remarkably good results.

The final portion of the dissertation concerns the effect of hygrothermal and accelerated aging on glass-reinforced composites. A meta-study is performed on data from the literature, and a glass-degradation-based life-prediction model is applied to the data. It is seen that a static fatigue-based activation energy approach to residual strength can predict activation energies associated with glass-reinforced composite strength degradation in the case of glass-reinforced concrete quite well, predicting values of 80-100 kJ/mol, which are similar to those expected for glass dissolution via silica ring opening. The model may also hold some promise for doing the same for glass-reinforced polymer composites.

Acknowledgements

I would like to express my sincere thanks to my committee members, particularly Scott Case and Jack Lesko, without whose patience and guidance this document would not be possible. They truly have been a wonderful pair of people to work with.

I would also like to thank Mac McCord who has been of incalculable help in advancing my research on an almost daily basis, and David Simmons who has always been willing to squeeze in a little shop work for me when I'm in a rush.

Thank you to Bev Williams, who somehow manages to keep track of the schedules of some extremely busy people, and who generally keeps the Materials Response Group running efficiently.

And most of all I am profoundly grateful to my mom, Cheryl Cain, my dad Jim Cain, and my grandmother Doris James, who have been a constant source of love, support and encouragement at all times for longer than I can remember.

Table of Contents

Abstract.....	ii
Acknowledgements.....	iii
Table of Contents.....	iv
List of Figures.....	vi
List of Tables.....	viii
1. Introduction.....	1
2. Literature Review.....	3
2.1. The effect of post-cure on the short- and long-term material properties of GRP.....	3
2.2. The effect of the R-ratio on the fatigue behavior of polymer-matrix composites.....	6
2.2.1. Introduction to composite fatigue.....	6
2.2.2. Fatigue life predictions based on micromechanical considerations and damage accumulation laws.....	8
2.2.3. Residual strength approaches.....	12
2.2.4. The effect of R-ratio and mean stress on fatigue life: data and models.....	16
2.2.5. Figures and Tables.....	19
2.3. Long-term moisture damage in glass-reinforced composites.....	22
2.3.1. Moisture-induced degradation of glass fibers and the static fatigue model.....	27
2.3.2. A method of GRP life prediction adapted from a GRC model.....	27
3. Paper: Post-curing Effects on Marine VARTM FRP Composite Material Properties for Test and Implementation.....	28
3.1. Abstract.....	29
3.2. Introduction.....	30
3.3. Literature Review.....	30
3.4. Materials, Fabrication and Post-curing.....	32
3.5. Experiments.....	33
3.5.1. Degree of Cure Characterization.....	33
3.5.2. Viscoelastic Characterization.....	34
3.5.3. Quasi-Static Mechanical Characterization.....	34
3.5.4. Laminate Fatigue Characterization.....	35
3.6. Results and Discussion.....	36
3.6.1. Panel Temperature Histories.....	36
3.6.2. FTIR Matrix Cure Measurements.....	36
3.6.3. Viscoelastic Characterization.....	36
3.6.4. Tensile Characterization of Pseudo-Quasi-Isotropic Laminates.....	38
3.6.5. Characterization of Angle Ply Laminates.....	38
3.6.6. Tensile Fatigue Characterization.....	38
3.7. Summary and Conclusions.....	39
3.8. Acknowledgements.....	40
3.9. Figures and Tables.....	41
4. The Effect of Mean Stress and the R-ratio on the Fatigue Performance of E-glass/Vinyl-ester Composites for Naval Applications.....	54
4.1. Introduction.....	54
4.2. Material description.....	57

4.3.	Details of the Case and Reifsnider residual strength model and its application to fatigue data	57
4.4.	Testing plan for constant- and variable-amplitude fatigue of E-glass/510-A and E-glass/8084 composites	60
4.4.1.	Constant-amplitude fatigue testing	60
4.4.2.	Variable-amplitude fatigue testing.....	61
4.5.	Constant-amplitude experimental results.....	62
4.5.1.	Data and analysis for the E-glass/510-A constant-amplitude testing	62
4.5.2.	Data and analysis for the E-glass/8084 constant-amplitude testing.....	65
4.6.	Variable-amplitude experimental results	66
4.7.	Conclusions.....	67
4.8.	Figures and Tables	70
5.	Testing of Hygrothermally Aged E-glass/Epoxy Cylindrical Laminates Using a Novel Fixture for Simulating Internal Pressure.....	95
5.1.	Abstract.....	96
5.2.	Introduction.....	96
5.3.	Material/testing description	98
5.3.1.	Axial tension and compression testing	99
5.3.2.	Hoop tension (burst) testing.....	100
5.4.	Mechanics Analysis of PTFE Seal and Composite Cylindrical Hoop Tension Samples .	101
5.4.1.	Elasticity Analysis of PTFE Ring Seal	102
5.4.2.	Donnell Theory Laminate Analysis of Cylindrical Composite Sample	104
5.5.	Results.....	105
5.6.	Axial compression and tension tests	106
5.7.	Hoop tension tests	108
5.8.	Conclusions.....	109
6.	The Application of a Static-Fatigue-Based Model for Accelerated Aging of Glass Fiber Reinforced Composites	111
6.1.	Introduction.....	111
6.2.	The Static Fatigue Model of Glass Degradation in the Presence of Moisture.....	113
6.3.	The Purnell Model	114
6.4.	Previously reported activation energies for the strength degradation of glass-reinforced composites and the dissolution of silica glass.....	116
6.5.	Review of the sources of the data sets to be analyzed	119
6.6.	Results.....	120
6.7.	Conclusions.....	121
6.8.	Tables and Figures	122
7.	Conclusions.....	128
8.	Bibliography	129

List of Figures

Figure 1: A typical sinusoidal loading curve	19
Figure 2: Example of loading curves for three common R-ratios.	19
Figure 3: An example of fatigue-to-failure data plotted on an S-N curve, in terms of normalized applied stress, Fa	20
Figure 4: An example of a Goodman diagram.....	20
Figure 5: Illustration of linear (Miner's rule) and nonlinear damage laws. (Excerpted from [23]).	21
Figure 6: An example of a fatigue failure envelope for a hypothetical material expressed in terms of mean stress and stress amplitude. (Excerpted from [54]).....	21
Figure 7: Resin oligomer and styrene monomer reaction to the vinyl ester network. The disappearance of styrene and methacrylate C=C are tracked by FTIR to assess the degree of cure quantitatively.....	42
Figure 8: Cure temperature profile for all panels.....	43
Figure 9: Vinyl ester and styrene conversion with time	44
Figure 10: DMA storage modulus curves for all panels on day 1	45
Figure 11: Normalized DMA storage modulus for panel 4501-NPC on all days.....	45
Figure 12: DMA storage modulus and tan delta curves for two replicates from panel 4504-93 on day 300.....	46
Figure 13: Creep compliance curves for panel 4501-NPC on all days.....	47
Figure 14: Mean initial modulus values of pseudo-quasi-isotropic specimens as a function of time and post-cure. Note that the error bars indicate the range of the data.	48
Figure 15: Mean ultimate tensile strength of pseudo-quasi-isotropic specimens as a function of time and post-cure. Note that the error bars indicate the range of the data.	48
Figure 16: Stress-strain diagrams of panel PQ04-93 during quasi-static tension tests on all days.	49
Figure 17: Mean initial shear modulus of $[\pm 45]_{2s}$ samples as a function of post-cure and time. Note that the error bars indicate the range of the data.	50
Figure 18: Shear strength for $[\pm 45]_{2s}$ panels as a function of post-cure and time. Note that the error bars indicate the range of the data.....	51
Figure 19: Typical stiffness reduction and temperature data for all panels on fatigue testing day 1.....	52
Figure 20: Cycles to failure data for all panels on all testing days. Note that the error bars indicate the range of the data.	53
Figure 21: Calculation of predicated residual strength Weibull CDF values.	77
Figure 22: Weibull analysis of residual strength data for E-glass/8084 composite.....	78
Figure 23: Normalized constant amplitude stress-life (SN) plots for R=0.1, R=-1, and R=10 (E-glass/510-A).....	79
Figure 24: Residual strength data for R=0.1 and loading of 44% UTS for E-glass/510-A composite.	80
Figure 25: Residual strength fit plots for E-glass/510-A material, at R=0.1 constant-amplitude loading.....	81
Figure 26: Residual strength data and predicted CDFs for R=0.1 and loading of a) 52% UCS and b) 44% UTS for E-glass/510-A composite.	82
Figure 27: Residual strength data for a) R=-1, and b) R=10 for E-glass/510-A composite showing sudden-death behavior, especially for R=10.....	83

Figure 28: Residual strength fit plots for E-glass/510-A material, at R=-1 constant-amplitude loading.....	84
Figure 29: Unacceptable cumulative distribution function for the residual strength of E-glass/510-A material at loading ratio of R=-1 resulting from numerical difficulties.	85
Figure 30: An acceptable cumulative distribution function for the residual strength of E-glass/510-A material at loading ratio of R=-1 at a loading of 29.9% UCS.	86
Figure 31: Residual strength data and model fit for R=10 for E-glass/510-A material under constant-amplitude load.	87
Figure 32: Cumulative distribution function for the residual strength of E-glass/510-A material at loading ratio of R=10.	88
Figure 33: Constant amplitude stress-life (SN) plots for R=0.1, R=-1, and R=10 (E-glass/8084).	89
Figure 34: Residual strength data and model fit for R=0.1 for E-glass/8084 material under constant-amplitude loading.	90
Figure 35: Residual strength and model fit for E-glass/8084 material at a constant-amplitude loading ratio of R=-1.	91
Figure 36: Residual strength data and model fit for E-glass/8084 for a constant-amplitude loading ratio of R=10.	92
Figure 37: The first few seconds of the time history of the Rayleigh-distributed spectrum with autocorrelation of 0.95.	93
Figure 38: SN plot for variable-amplitude spectrum loading of E-glass/8084 material at R=10.	94
Figure 39: End-loaded side-supported fixture for axial compression testing.	99
Figure 40: Fixture and PTFE seal used for hoop burst testing.	101
Figure 41: Moisture absorption of E-glass/Epoxy helically-wound tubes.....	105
Figure 42: Axial compressive and tensile strength of aged FRP cylinders.	106
Figure 43: Shifted axial compression strength plot with fit line.....	107
Figure 44: Hoop strength of aged FRP cylinders.....	108
Figure 45: Time-shifted hoop strength with Arrhenius fit line.....	109
Figure 46: Reaction steps in environmentally enhanced fracture of vitreous silica in (a) the Michalske-Freiman model and (b) the Michalske-Bunker model. (Excerpted from West and Hench [109]).	124
Figure 47: The reaction path for the Si-O bond fracture with the interaction of water with the five-fold ring-chain structure. (Excerpted from West and Hench [109]).	125
Figure 48: Arrhenius plot for PP_comp_OPCI data set showing the fits for the linear and nonlinear models. The slopes of the lines represent the activation energy divided by the gas constant, R.....	126
Figure 49: The Purnell model [101] fit to strength data, taken from HK-0 data set.....	127

List of Tables

Table 1: Post-cure Conditions and Panel Designations	41
Table 2: Constant-amplitude fatigue to failure testing for E-glass/510A and E-glass/8084	70
Table 3: Test plan for constant-amplitude residual strength testing	71
Table 4: Test plan for variable-amplitude fatigue to failure testing with Rayleigh-distributed spectrum.....	72
Table 5: Curve fit parameters for normalized E-glass/510-A S-N curves for three R-ratios.	73
Table 6: Results of Weibull analysis of E-glass/510-A constant amplitude residual strength tests at R=0.1.....	73
Table 7: Results of Weibull analysis of E-glass/510-A constant amplitude residual strength tests at R=-1.	74
Table 8: Results of Weibull analysis of E-glass/510-A constant amplitude residual strength tests at R=10.....	74
Table 9: SN curve fitting parameters for constant-amplitude fatigue testing of E-glass/8084 material.	75
Table 10: Weibull analysis for the residual strength of E-glass/8084 at constant-amplitude R=0.1 loading.....	75
Table 11: Weibull analysis for the residual strength of E-glass/8084 at constant-amplitude R=-1 loading.....	76
Table 12: Weibull analysis for the residual strength of E-glass/8084 at constant-amplitude R=10 loading.....	76
Table 13: Test plan for composite testing (number of replicates).	98
Table 14: Time-based shift factors for axial compression strength.....	107
Table 15: Time-based shift factors for hoop tensile strength.	109
Table 16: Data set designations for GRC and GRP data sets.	122
Table 17: Model fit results for all data sets.....	123

1. Introduction

E-glass/vinyl-ester composites are increasingly being used in naval and civil applications, such as ship deck structures and wind turbine blades. In these applications the material may be subjected to cyclic stresses of randomly varying magnitude and sign, and will usually also be exposed to moisture, both of which reduce the material strength. Therefore, in order to design with these materials efficiently, it must be understood, in a quantitative way, how these conditions (mechanical loading and moisture exposure) affect the performance of the composite. In addition to these service conditions, the manufacturing method and initial post-cure of the material also determine the subsequent material performance in as much as it determines the initial value from which the strength degrades when exposed to its service environment. This dissertation will, therefore, begin by describing work that has been completed in the area of characterizing E-glass/vinyl ester composites in terms of their degree of initial post-cure. These results will lay the ground work for the understanding of the remaining portion of the work.

Once this foundation has been laid, this dissertation will focus on two areas of current composite durability and life prediction research that are important for the efficient use of these materials in various civil, naval, and aerospace applications. The first area to be discussed concerns the effect of the loading parameters, such as R-ratio (defined as the ratio of the minimum applied load to the maximum applied load, and discussed in detail in a later section), mean stress, etc. on the remaining strength and fatigue life of composite materials. It is well documented that the fatigue behavior of glass-reinforced composite materials (and carbon-reinforced materials, as well) is largely a function of the R-ratio, as well as other factors such as load amplitude and mean stress, cycle order, etc. However, there are currently no satisfactory models to describe/predict the strength loss and ultimate fatigue life of these materials under any arbitrary loading condition, nor even under constant amplitude loading at an arbitrary R-ratio. Typically, the Palmgren-Miner damage accumulation rule is used, along with a large amount of experimental data used for fitting the model. However, this linear model has been shown to be unsatisfactory when used for most composite materials. Therefore, this dissertation will discuss a portion of on-going efforts in the Materials Response Group at Virginia Tech to develop a more accurate and general composite strength and life prediction model. The work described will concentrate on the R-ratio and mean stress effects of constant-amplitude and variable-

amplitude fatigue loading, and will complement other current work that is looking at other aspects of variable amplitude fatigue loading (i.e., RMS level). Experimental results from fatigue-to-failure and remaining strength tests will be presented and discussed, and a portion of the proposed future work will use microscopy techniques to develop a better understanding of the mechanics of damage accumulation as a function of R-ratio in the hopes that this understanding will lead to more effective, better informed life prediction models.

The second portion of the work will investigate how moisture affects the strength of glass fiber reinforced composites. This is largely focused on the interaction of water with the glass fibers themselves. Much work has been done on the investigation of the hydrolysis of glass and how this process leads to the gradual degradation of strength, also known as “static fatigue”. Many methods have been used to predict this process, from traditional fracture-mechanics-based approaches to *ab initio* molecular dynamics methods; the latter are becoming more effective as available computing power increases. Some models of glass degradation have been adapted and fit to experimental data from glass-reinforced composites. These models are of various degrees of applicability. The discussion will describe a new model that has been used to model the strength degradation of glass-reinforced concrete, but which has recently been preliminarily extended to glass-reinforced polymer composites (GRP). The work in this area will entail a meta-study utilizing various GRP and GRC moisture studies and applying the model to the data in order to assess its general applicability.

2. Literature Review

2.1. The effect of post-cure on the short- and long-term material properties of GRP

Designers of composite structures, whether they design for civil, naval, or aerospace applications, need to be able to understand the way the materials they choose to use will change with time. In addition to the material changes brought about by environmental and mechanical loads (discussed in the following sections), often the materials will change due to changes in the degree of cure of the matrix material.

As polymers originally cure during the manufacturing process, they often are left in a state of incomplete cure. In such cases, often the degree of cure will gradually increase over time, usually at a rate that is significantly slower than the original cure. As the cure advances, material properties such as modulus, ultimate strengths, strain to failure, and resistance to moisture or fatigue change. Often these changes are for the better; sometimes they are not. However, for efficient use of the material, the changes must be accounted for in the original design.

It is usually possible to bring the matrix to a more-complete degree of cure than is accomplished during manufacturing through the use of a post-cure, in which additional energy (in the form of heat or ultraviolet light, for example) is added for a time after initial cure. The degree of this post-cure is critical, though, as it often will bring about both wanted and unwanted effects. In addition, for large structures such as bridges and especially naval craft, the energy required may be excessive or impractical to apply, limiting the amount of post-cure that can be carried out. Therefore, compromises often have to be made, and so an understanding of the trade-offs involved is needed.

There are many ways in which to assess the degree of cure of a matrix material. There is extensive work [1-3] that has been done looking at the step growth polymerization of epoxies, which are widely used in the composites industry. These researchers have shown that the glass transition temperature, T_g , is closely linked with the degree of cure. Wissanrakkit and Venditti [2, 3] showed that for some epoxy systems undergoing isothermal cure, there is, in fact, a one-to-one correspondence between the T_g and degree of cure. One must be careful, though, in

asserting a given T_g based on a given degree of post-cure. As Chang [4] points out, the full history of cure affects the final network structure.

Venditti [2] developed a simplified equation, based on Couchman's [5] equation, to relate the T_g to degree of cure for certain epoxies. Venditti also [1] investigated the relationship between material properties and conversion. Specifically, he looked at modulus, density, and T_g and used differential scanning calorimetry (DSC) to assess degree of cure. Then converting T_g into the measure of conversion, he created property-conversion-temperature diagrams for the materials in question. However, while the correlation between degree of cure and T_g has been shown to be good for epoxies, the relationship between T_g and the microstructure has not been as clearly shown.

On the other hand, much effort has gone into studying the cure kinetics of free radically cured systems, such as vinyl-esters, which recently have been the primary matrix of concern for those working in the Materials Response Group at Virginia Tech. These matrices are formed by copolymerization reactions between ethers of Bis-A and styrene monomer, and involve a more complicated cure process than that of step-growth polymerization reactions.

While several studies have defined the degree of cure for step-growth polymers in terms of endothermic arguments [1-3, 6, 7], Verghese [8] has extended those ideas to free-radically cured resins and treated the resin as a blend of crosslinked polymer and monomer. This approach is less complicated than the method proposed by Hale et al. [9], who developed a model for the relation between T_g and the extent of cure. This model was based on the assumption that the T_g is increased by three factors: the decrease in the number of free chain ends, the formation of crosslinks, and the decrease in entropy associated with the molecular configuration.

Similarly to the work of Venditti in epoxies, Li [10] has investigated the relationship between the network structure of vinyl-esters and some material properties (specifically T_g and fracture toughness). This was accomplished by varying the molecular weight of the oligomer, as well as the concentration of styrene monomer. With decreasing styrene concentrations, both T_g and fracture toughness were seen to increase. It was also found that larger molecular weight oligomers led to improved fracture toughness. Ziaee [11] performed similar tests, but looked at more mechanical properties, and used Fourier Transform Infrared Microscopy (FTIR) measurements to assess the degree of cure. FTIR has the advantage over T_g measurements

because the latter involve heating the material past its T_g (as part of a DSC or DMA test), and thus, additionally curing the resin and changing the T_g itself.

Aside from purely chemical studies, there have been a number of studies that look at the effect of matrix degree of cure on the overall material properties of composites. Bradley [12] looked at the effect of degree of cure on viscoelastic properties of E-glass/vinyl-ester laminates. He found that vinyl-ester composites that were room-temperature cured showed more viscoelastic (creep) behavior than those that reached “complete” cure after being post-cured at 93°C. (As a side note, Cain et al. [13] found for similar materials that they did not quite see “complete” conversion even at 93°C, though the conversion did seem to be stable at that point and did not increase with time afterwards.)

Cvetanovska [14] investigated the effect of post-cure on mechanical properties for UV-cured composites, but also compared those results to some that were thermally post-cured. Not surprisingly, it was found that a higher degree of cure (which, for the thermally cured resins meant a higher temperature post-cure) resulted in harder and stronger (in tension) composites.

He [15] performed similar tests on a high-temperature carbon/BMI system to which he applied high post-cure temperatures (up to 246°C). He found that flexure properties (modulus) and Mode II fracture toughness were increased with post-cure temperatures up to 216°C, but decreased at higher temperatures, perhaps as a result of matrix embrittlement. In addition, the in-plane shear properties were adversely affected by increasing post-cure, probably for the same reason.

Instead of varying the temperature of post-cure, Ota [16] applied a consistent post-cure temperature to woven glass/vinyl-ester composites but varied the time over which it was applied. The post-cure times ranged from 0 to 24 hours. A variety of mechanical properties were measured, including moduli, hardness, T_g , and flexural strength. Microscopy was also carried out on post-mortem samples to investigate the damage that may have been caused by excessive post-cure times. Ota found that except for the 24-hour post-cure, all post-cure regimes resulted in decreased viscoelastic behavior and increased mechanical properties. The 24 hour cure resulted in reduced mechanical properties, which Ota attributed to degradation of the fiber/matrix interface. For the microscopy samples, delamination was more likely to occur for low post-cure times, such as 0 or 4 hours, but also for the 24 hour post-cure.

Tucker [17] varied both the post-cure temperature and duration to investigate the effect these parameters had on the mechanical properties of both neat vinylester resin and a unidirectional glass/vinylester composite. For the composite samples the temperature was consistent at 90°C, while the durations were 1, 4, and 24 hours. These samples were tested for Mode I fracture toughness using a DCB specimen geometry. At these conditions, it was found that the 1- and 4-hour post-cures tested resulted in increased toughness of the composite. However, the 24-hour post-cure resulted in a lowering of the toughness. Tucker attributes this effect to the weakening of the fiber/matrix interface.

Despite the usefulness of all of the above studies, none of them address one important question: are all of these measured material properties that are functions of degree of cure and post-cure also functions of time? That is to say, are the material properties measured temporally stable, or will they evolve with time for given degrees of cure? As mentioned at the beginning of this section, this is a very important question for someone attempting to use these materials in the design of a structure that is expected to see long service lifetimes, especially if overdesign is to be avoided. This is one of the primary questions investigated in the following chapter.

2.2. The effect of the R-ratio on the fatigue behavior of polymer-matrix composites

2.2.1. Introduction to composite fatigue

Fatigue is simply the application of cyclic mechanical loads on a material, which causes a progressive loss of materials properties such as strength and stiffness, accompanying a progressive increase in internal damage. For metallic materials, the damage may be in the form of plastic yielding or particularly crack initiation and propagation. This phenomenon has been studied exhaustively over many decades and is fairly well understood and characterized for most metallic (i.e., homogenous, isotropic) materials.

For composite materials, however, fatigue is much more complicated due to the nonhomogenous, anisotropic nature of composites. The accumulated damage in a composite can

take many forms. Under tensile loads, most composites will first exhibit damage in the form of transverse and shearing matrix cracks. The reinforcing fibers, too, can break, leading to significant losses in the material modulus. The fibers may become debonded from the matrix, leading to a loss in the ability of the matrix and fibers to share distributed loads. For compressive loading, matrix crushing and local (or global) buckling may occur. Some or all of these damage modes can lead, eventually, to debonding between lamina within the laminate, and eventually, failure of the material. Due to the complicated micromechanics involved, however, it is very difficult to predict with certainty how damage will progress through a laminate for any given loading condition, and, therefore, it is very difficult to predict lifetimes of composite structures that will experience fatigue loading.

Since composites are often subjected to fatigue while in service as structural members of civil, naval, or aerospace applications, much effort has gone into better understanding how these materials behave under such loading. Many models, some of which will be discussed in the following sections, have been developed, which attempt to explain why and how fatigued composites lose stiffness and strength. And of course, extensive experimental work has been performed, both to validate particular models and also simply to characterize various materials under equally various conditions.

Usually during experimental material characterization, either a small coupon or a larger structure or substructure is subjected to a cyclic load, generally of a sinusoidal nature, as in Figure 1. The loading may be either stroke-controlled or load-controlled.

One parameter associated with the loading which has bearing on this portion of the proposed dissertation is the R-ratio, which is defined as the ratio of the minimum applied stress to the maximum applied stress during a given fatigue cycle. For instance, in Figure 2 are shown examples of load curves for $R=0.1$ (tension-tension), $R=-1$ (so-called “fully reversed”), and $R=10$ (compression-compression).

While most composites will see loading whose amplitude is variable, for simplicity, and as a measure of basic material properties, much experimental work has been performed using constant-amplitude loading. For such loading, if the samples are run to failure, then the data can be plotted on an S-N curve, where the applied stress is plotted on the ordinate and the number of fatigue cycles to failure is plotted on the abscissa. Such plots are designed to allow designers to

estimate mean lifetimes of a material at a given loading level. The data may also be used to estimate the amount of damage that a composite suffers during any given cycle of a variable amplitude loading. This is not a straightforward problem, however, and the difficulties and attempted solutions will be discussed in later sections.

Generally, a curve is fit through the data so that a closed-form equation relating load to lifetime can be achieved. These curves are often expressed in terms of a power-law relation, such as Equation 1:

$$N = B\sigma^A \quad (1)$$

which, by taking the logarithm and rearranging can alternatively be written as Equation 2:

$$\log(\sigma) = a \log(N) + b \quad (2)$$

The latter form is useful as it plots as a straight line on a log-log graph, though the data is sometimes plotted on a semi-log graph. Figure 3 shows typical fatigue-to-failure data plotted on a semi-log S-N curve.

When S-N data has been generated for multiple R-ratios for a given material, the fatigue data are often plotted on a Goodman diagram, like Figure 4. In this representation, the stress amplitude is plotted on the ordinate and the mean stress is plotted on the abscissa for a given lifetime. Then “iso-life” lines can be drawn between points of equal life. This format allows for qualitative differences in the fatigue behavior of a material at different R-ratios and different lifetimes to be visualized readily.

2.2.2. Fatigue life predictions based on micromechanical considerations and damage accumulation laws

In an attempt to predict lifetimes of composites subjected to fatigue (particularly multi-stress-level or variable-amplitude fatigue), many models have been developed and refined over the years. Some of these are primarily data curve fits, while others are sometimes based on elaborate micromechanical descriptions of hypothetical damage. But arguably the most popular methods

of life prediction is the Palmgren-Miner [18, 19] method, or Miner's Rule. This method defines the state of damage, D , within the material on a scale of 0 to 1. At $D=0$, the material is undamaged; at $D=1$, the material fails. The cumulative damage, D , is defined as

$$D = \sum d_i \quad (3)$$

where the d_i represent the damage accumulated in a given block of loading of a certain stress level, i . They are mathematically defined as

$$d_i = \frac{n_i}{N_i} \quad (4)$$

where n_i is the number of cycles at the stress level i , and N_i is the number of cycles to failure expected at that stress level.

Miner's rule experiences such great popularity largely due to its ease of use, as well as familiarity to generations of designers in various fields. However, while it may be arguably useful in the design of some metallic structures, it has been shown (e.g., [20]) repeatedly to be unsuitable for the design of composite structures. Not only is the method not consistently accurate in these cases, but it cannot be said to be conservative, as it often may return very non-conservative results.

One large drawback and limiting aspect of Miner's rule is its inability to take into account cycle order for variable-amplitude loading. It has been shown repeatedly [20-22] that the damage accumulation for composites is a function of the order of the loads applied. However, Miner's rule has no mechanism for 'remembering' past cycles, and so no ability to take into account cycle order.

Variations to Miner's rule have been developed. One alternative was developed by Adam et al. [21]. The model looks very similar to Miner's rule with the exception of a non-linear exponent on the right-hand side:

$$d_i = \left(\frac{n_i}{N_i} \right)^\alpha \quad (5)$$

where α is a parameter that causes the relationship between fractional damage and fractional life to be nonlinear, as opposed to the linear relationship seen in Miner's rule. This can be seen in Figure 5, below. The nonlinear aspect of Figure 5 implies that this method does take into account cycle order, unlike many similar models.

Adam et al. applied this model to a variety of loading situations for T800/5245 carbon fiber composites. Two- and four-unit block loadings were applied for tension, compression, and mixed loadings. It was seen that while Miner's rule was reasonably successful at predicting life for tension-tension fatigue, it grossly overestimated life for compression-compression and mixed loadings. The updated model was successful at modeling the various loadings, and the parameter α was found to be proportional to the applied stress.

Some researchers have attempted to use the material stiffness as an indicator of accumulated damage. Poursartip et al. [23] used the tensile stiffness in quasi-isotropic carbon fiber specimens as a measure of damage. The damage was considered to be of the form of a crack front progressing inward from the edges of the sample, and was mathematically defined at any given point in time in terms of a crack growth rate that was a function of the applied stress level, the R-ratio, and the present value of damage.

In a follow-up paper Poursartip et al. [24] used the damage formulation from the first paper to make predictions for constant amplitude fatigue at other R-ratios and for variable amplitude (block and random) loading. The agreement for constant-amplitude tests is good, but less so for variable amplitude loading. The authors recognize an 'acceleration' of the damage that occurs when the loading amplitude changes during the test. This is effectively the cycle-mix factor described by Schaff and Davidson [25, 26], discussed in a later section. Interestingly, as Kedward [27] points out, Poursartip has recognized the edge effects seen when testing small coupons by pointing out that the damage fronts always progress inward from the edges. This effect is often not accounted for when taking coupon data and using it to design larger structures.

Van Paepegem et al. [28, 29] developed a complex-seeming model for damage in which six damage parameters were used to estimate the total damage. The authors used a model of their devising to perform finite element calculations simulating the fatigue damage of glass/epoxy laminates with a [45]₈ schedule. For this simple and specific lay-up the authors claimed

reasonably good comparison between experiment and simulation for the bending stiffness in fully-reversed loading.

Yang et al. [30] developed a two-parameter stiffness-based statistical fatigue life prediction model for graphite/epoxy laminates, as well as a model [31] for predicting residual stiffness of graphite/epoxy composites.

The advantage of the stiffness reduction method is that the stiffness is usually something that is fairly easy to measure during a test. However, Post [32] has shown that for quasi-isotropic E-glass/vinyl-ester laminates with significant fiber reinforcement in the loading direction there is no significant correlation between stiffness and residual strength (or conversely, damage). So stiffness cannot be said to be a universal indicator of damage for some common types of laminates.

Diao and Xing [33] developed a model in which fatigue damage is modeled using a stochastic approach for the evolution of matrix cracks. This was an attempt to introduce spatial inhomogeneity into the material failure.

Interestingly, Osiroff and Stinchcomb [34] used dynamic mechanical analysis (DMA) to assess the state of damage within composites. They used traditional means of damage evaluation, such as remaining strength, remaining stiffness, and nondestructive evaluation techniques to characterize the damage states of the laminates. Then they used DMA approaches to establish the material's time-dependent properties, such as its creep response at various temperatures, and the glass transition temperature at various frequencies. The authors were able to successfully draw conclusions as to the relationship of the viscoelastic nature of the material and the damage state it was in; however, they did not attempt to explain the correlation in such a way as to make this a viable way of predicting the damage state of a material that has not first been exhaustively characterized in this way. That is to say that the authors presented an alternative method of damage assessment, but did not provide a tool for prediction. The method, however, is useful for helping to understand the effects that various damage states have on the viscoelastic properties of a given composite.

There has been a significant amount of work done in the area of using microscopy to evaluate the damage state of composites. Both optical and electron microscopy have been used, although the latter is more often useful for researchers trying to understand the damage modes at the scale of

the fiber reinforcement. In at least one case [35], scanning electron microscopy has been performed on the sample during the testing phase; that is, the mechanical testing has been performed in-situ within the SEM. In this test, the sample was subjected to static loading only, not fatigue, but the damage state was correlated to the material stiffness. Doucet and Qin [36] used SEM to investigate the damage state of glass/epoxy composites subjected to impact loading.

In other cases, SEM was used as a destructive evaluation tool on post-mortem samples taken from samples with varying degrees of damage. Scida et al. [37] did not investigate fatigue. However, they did look at the effect of moisture-conditioning on the initial quasi-static material properties (tensile and shear modulus and strength) of woven glass/epoxy laminates.

Barchan [38] subjected glass/epoxy composites to bending fatigue loads until the bending stiffness dropped by 40%, at which time he used SEM to investigate the character of the fatigue damage state, while using acoustic emission taken at various points as a quantitative measure of the damage state. Barchan concludes that for low cycle fatigue, the sample experiences significant delaminations (or meta-delaminations), which are largely clustered near the sample edges. Towards the center of the sample the damage is reduced. (This is similar to results that we have seen in axial compression tests, where delamination and local buckling are the primary forms of damage and failure and these most often start near the edges.) At low loading levels, along with the expected matrix cracking, Barchan describes fibers that are broken in multiple places along their length, and attributes this as the major cause of the composite modulus reduction.

2.2.3. Residual strength approaches

Many approaches have been developed to model and predict fatigue life and remaining strength. Some of the more important of these models are described in [39]. One of the first remaining strength models was by Broutman and Sahu [20]. In the paper, the authors applied Miner's rule to a series of two-block loading cases on glass/epoxy composites and found that the agreement between theory and experiment was considerably poor. So they proposed a model of the form of Equation 6:

$$S_{r,i} = S_{r,i-1} - (S_u - \sigma_i) \frac{n_i}{N_i} \quad (6)$$

where $S_{r,i}$ is the remaining strength at a given loading level, i , $S_{r,i-1}$ is the remaining strength at the end of the previous block of loads, S_u is the initial strength of the material, σ_i is the applied load of the i th loading block, n_i is the number of cycles applied in the i th loading block, and N_i is the expected lifetime of the material at the load σ_i .

For multiple block loadings, the damage of the various blocks can be summed and failure can be said to occur according to Equation 7:

$$S_r - S_u - \sum_{i=1}^{Failure} (S_u - \sigma_i) \frac{n_i}{N_i} = \sigma_i^{Failure} \quad (7)$$

Broutman and Sahu found that their model gave significantly better results of residual strength prediction than Miner's rule for the two-block loading case.

Soon after Broutman and Sahu, Chou and Croman [40] developed a new remaining strength model. This model was a nonlinear and stochastic model, and utilized the strength-life equal-rank assumption. This assumption states that a sample that lies in the X th percentile in initial strength also lies with the X th percentile in fatigue life. This assumption is often made, though it is difficult or impossible to prove experimentally, because to measure the remaining strength in a sample requires its testing to destruction, and therefore it is impossible to measure what its fatigue life would have been. Using this assumption, however, Chou and Croman arrived at Equation 8 for remaining strength:

$$S_r^\alpha = S_{u,k}^{\alpha_1} - \eta_k^{\alpha_1} \left(\frac{\eta_k}{\beta_1} \right)^{j\alpha_1} \quad (8)$$

where S_r is the remaining strength, S_u is the initial strength, $S_{u,k}$ is the initial strength value that will give a cumulative distribution function value of k , η is the value of life with a cumulative distribution value of k , α and β are the Weibull distribution parameters for a two-parameter Weibull distribution, and j is a curve-fitting parameter.

To validate their model, Chou and Croman applied it to several data sets from the literature. The model was able to fit reasonably the data that they had, although the limited nature of the residual strength data meant that the detail in the curves was limited. That is to say, the remaining strength curves were not able to capture details of the behavior but only gross trends. This model in the form presented here is only suitable for predicting remaining strength for constant amplitude loading, which is a great limitation for many designers who need to anticipate variable amplitude loading.

Building on the Broutman and Sahu approach, Yang and Liu [41] developed a new residual strength model based on the assumption that the residual strength degrades monotonically. The model was verified using unnotched carbon/epoxy laminates and used constant amplitude loading in tension. The model was stochastic in that it started out with a statistical initial strength distribution as an input. Specifically, the initial ultimate strength of the material was described by a two-parameter Weibull distribution. The model of residual strength loss was similar in form to the Broutman and Sahu model. Since the inputs were stochastic in nature, the model returned a statistical description of fatigue life, as well.

Schaff and Davidson [25, 26] developed a remaining strength model. The model took the form of Equation 9:

$$S_r(n) = S_u - (S_u - \sigma_{applied}) \left(\frac{n}{N} \right)^v \quad (9)$$

where Schaff and Davidson considered v to be a function of the applied stress level.

Parenthetically, Schaff and Davidson also introduced a “cycle-mix” factor into their model. This cycle mix factor attempted to account for the fact that when the applied stress is variable, the order in which the various stress levels are applied can have a significant effect on the fatigue life of the material. This factor was only applied at certain points in the fatigue spectrum when the stress amplitude changed sufficiently, and was given by Equation 10:

$$CM = C_m R_0 \left(\frac{\Delta S_{mn}}{R(n)} \right) \left(\frac{\Delta S_p}{\Delta S_{mn}} \right)^2 \quad (10)$$

where ΔS_{mn} and ΔS_p are the changes in mean and peak applied stresses, R is the remaining strength, and C_m is effectively a curve fitting parameter that must be determined empirically for a given material. This factor is used to reduce the remaining strength at a given cycle over what would normally be the case without the cycle mix factor in the original model. Schaff and Davidson validated their model with data from Schultz [42].

This cycle mix effect was demonstrated clearly when Post et al. [22] conducted random spectrum loading on E-glass/vinyl-ester composites. This ‘random’ spectrum was comprised of approximately 732,000 cycles. First, a set of samples were tested using ascending block loading, in which the random spectrum was sorted such that the lowest amplitude cycles were first, then the next largest, and so on to the highest amplitude cycles. A second set was tested in descending order. And a third set was run using the completely randomized spectrum. Post found that the randomly ordered spectrum samples failed very prematurely compared to what was predicted, while the block loading cases did not.

Recent efforts at Virginia Tech have used the remaining strength model first proposed by Case and Reifsnider [43]. This model is a nonlinear damage accumulation model that employs one curve-fitting parameter (plus the fitting parameters from the SN curve) to fit empirical residual strength data.

This model has been successfully used in the past to model constant-amplitude fatigue life at $R=0.1$ (tension-tension loading.) However, current research efforts by the author and his colleagues have begun looking at developing a predictive, reliability-based model of GFRP (glass fiber reinforced polymer) composite remaining strength for spectrum (i.e., variable amplitude) loading.

The model assumes a two-parameter Weibull [44] distribution for material properties, such as the initial strength of the material, given by Equation 11, below:

$$P_f = 1 - e^{\left(-\frac{\sigma_{init}}{\beta}\right)^\alpha} \quad (11)$$

where α and β are the Weibull shape and location parameters, respectively.

The Case and Reifsnider remaining strength prediction model [43] is shown in Equation 12:

$$Fr(n) = 1 - \left[\int \left\{ \frac{(1 - Fa(n))^{\frac{1}{j}}}{N(Fa)} \right\} dn \right]^j \quad (12)$$

where n is the number of cycles, Fr is the normalized remaining strength (normalized by the median initial strength), Fa is the normalized applied stress, N is the number of cycles to failure at a given load Fa , and j is a curve fitting parameter. For constant amplitude loading, Equation 12 reduces to Equation 13:

$$Fr(n) = 1 - (1 - Fa(n)) \left(\frac{n}{N(Fa)} \right)^j \quad (13)$$

Failure is considered to occur when the applied stress is equal to or greater than the residual strength. That is, the material fails when $Fr(n) \leq Fa(n)$.

2.2.4. The effect of R-ratio and mean stress on fatigue life: data and models

Much characterization work has been done to describe the effect of the mean stress, and the related parameter of the R-ratio, on the fatigue lives and remaining strength of GRPs. This data is often taken from constant-amplitude fatigue tests, though it has been used by many to make predictions of variable-amplitude fatigue life and remaining strength. This section will document some of the more prominent material characterizations in this vein.

El Kadi and Ellyin [45] characterized the effect of R-ratio on unidirectional glass/epoxy laminates. They looked at various fiber orientations: 0, 19, 45, 71, and 90° from the load axis. As expected, the SN curves generated for each orientation and for each R-ratio were different. They defined a fatigue failure criterion in terms of the input strain energy, claiming that since this parameter does not rely on the different failure modes obtained in composites, it gives equally good results independent of the failure mechanism. They developed a normalized form of this strain energy criterion and showed that it can be used to collapse all of the data from the different R-ratios and fiber orientation angles.

Later El Kadi and Al-Assaf [46] trained a neural network to predict the fatigue lifetimes of unidirectional composites using the data from above. Vassilopoulos et al. [47] also used a neural network, but used data from multidirectional composites to train it.

Epaarachchi and Clausen [48] developed an empirical model to account for the effect of R-ratio (as well as testing frequency) on the fatigue behavior of GRPs. The goal was to create a model that could be used for fatigue life predictions with a well-defined minimum of tests. Beginning with an equation for constant amplitude fatigue life derived by Sendekyj [49], Epaarachchi and Clausen arrive at a complicated equation with two fitting parameters. With this method, the two parameters can be found by a small number of tests at only one R-ratio and a few stress levels, and make predictions for various R-ratios. The authors fit their model to a fairly large data set from the literature and showed reasonably good results. They presented a table that catalogued the curve fitting parameters for various materials.

Conle [50] conducted fatigue tests on pultruded glass/polyester composites and found that the mean stress has a small impact on the slopes of the SN curves for various levels of mean stress. They also found that the relationship between the ratio of the bending stress over the initial bending stress and the ratio of fatigue cycles to the total number of cycles at failure was independent of both the stress amplitude and mean stress.

Rotem [51] developed a method for predicting SN curves for composite laminates that are tested under any given R-ratio. Essentially, the method relies on the researcher characterizing the behavior of the material under tension-tension and compression-compression loadings.

Rotem presents a form of data representation that he calls a failure envelope, somewhat similar to a failure envelope for various static stress criteria (maximum stress, maximum strain, etc.) In this method, a plot is created where the mean stress is plotted on the abscissa and the load amplitude is plotted on the ordinate. Lines of constant lifetimes, in cycles, are created and a failure envelope emerges. When the SN data from tension-tension and compression-compression tests are plotted on the failure envelope plot, essentially the ends of the resulting curves are connected with straight lines forming a quadrilateral that is considered to be the fatigue envelope for that material, as in Figure 6.

Using the analysis behind this method, one can predict SN data for any R-ratio based on the failure envelope generated from just two SN curves (and static strength data). Rotem performed

“extensive” testing to verify the predictions and found reasonable agreement, though generally the number of samples for some R-ratios was too small to draw firm conclusions. Some shortcomings of the model included not predicting “unexpected” behaviors, such as changes in the failure mode during tests (i.e., at a certain number of cycles), and failure modes that were contrary to the applied mean stress.

In the area of empirical fatigue of composites at various R-ratios, perhaps no one is as prolific as Sutherland and Mandell [52, 53]. They have done much work on the extensive MSU/DOE (Montana State University/Department of Energy) database [54] that is a large compilation of fatigue data relating to composite materials for wind turbine applications. Because of the nature of the wind turbine environment, much of their work is focused on spectrum loading lifetime prediction. However, they have generated many Goodman diagrams based on constant amplitude loading. These tests cover a wide range of R-ratios, and are often run out to very long lifetimes, something that is very useful for many designers in the civil and naval fields.

Cain et al. [55] have produced similar diagrams, though with many fewer R-ratios, for E-glass/vinyl-ester composites manufactured at Virginia Tech. These data have highlighted weaknesses in the model that has been used in the Materials Response Group at Virginia Tech in the past. It is hoped that the completed characterization of this material will lead to a more effective model in the near future.

2.2.5. Figures and Tables

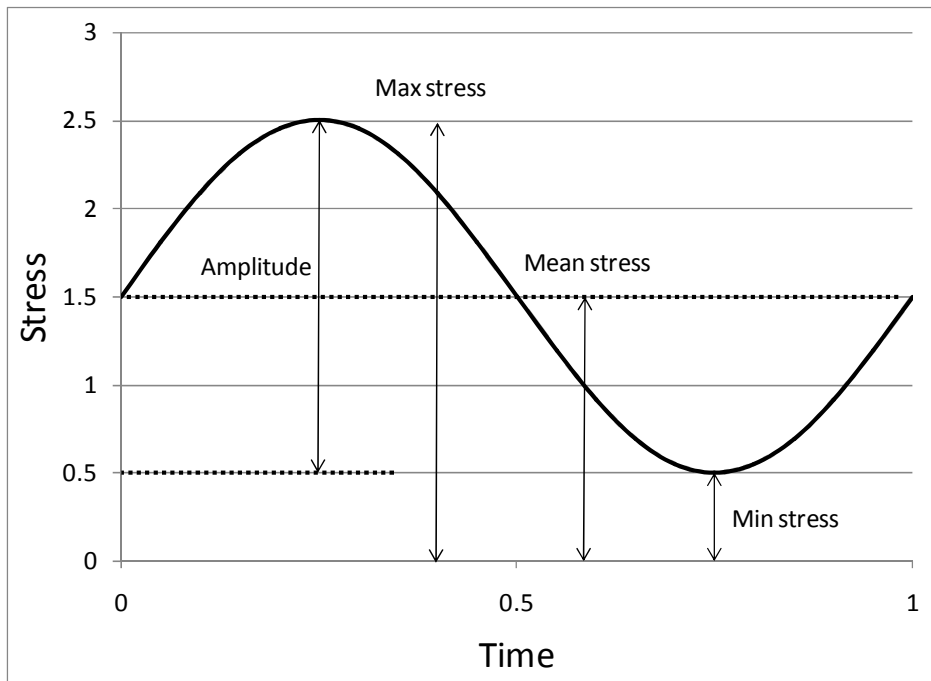


Figure 1: A typical sinusoidal loading curve

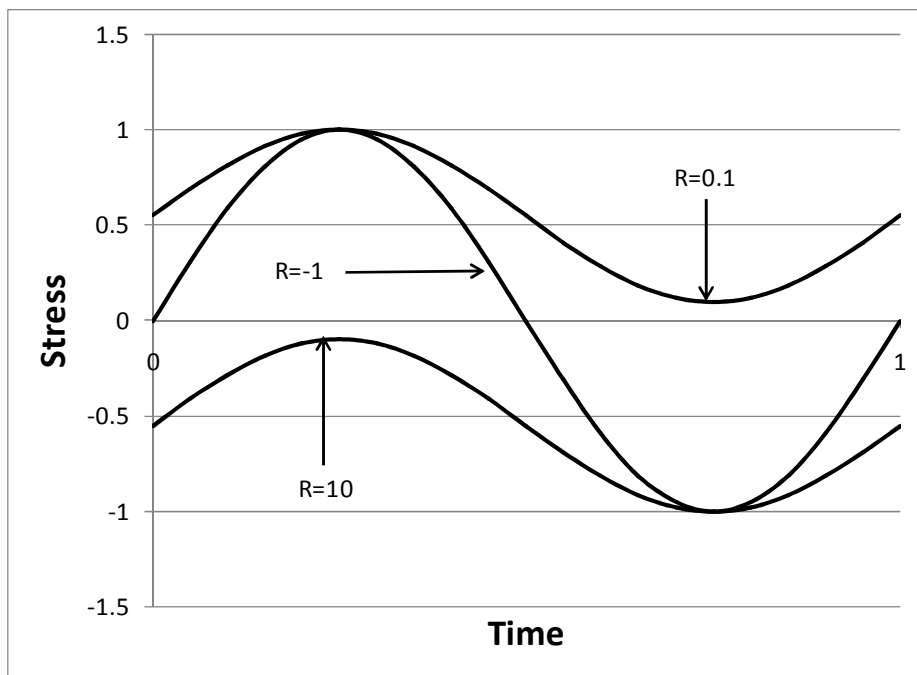


Figure 2: Example of loading curves for three common R-ratios.

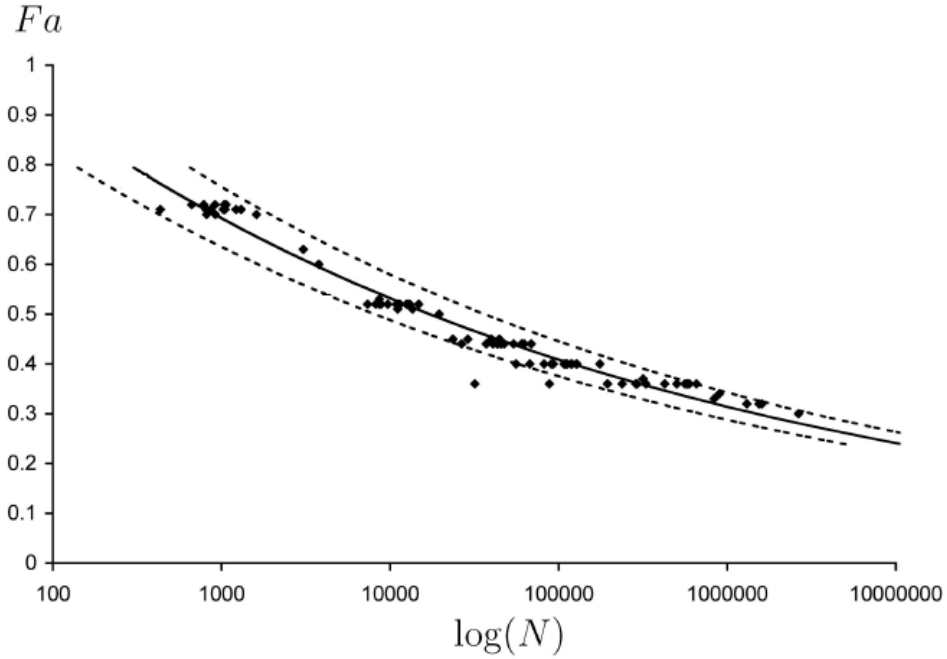


Figure 3: An example of fatigue-to-failure data plotted on an S-N curve, in terms of normalized applied stress, Fa .

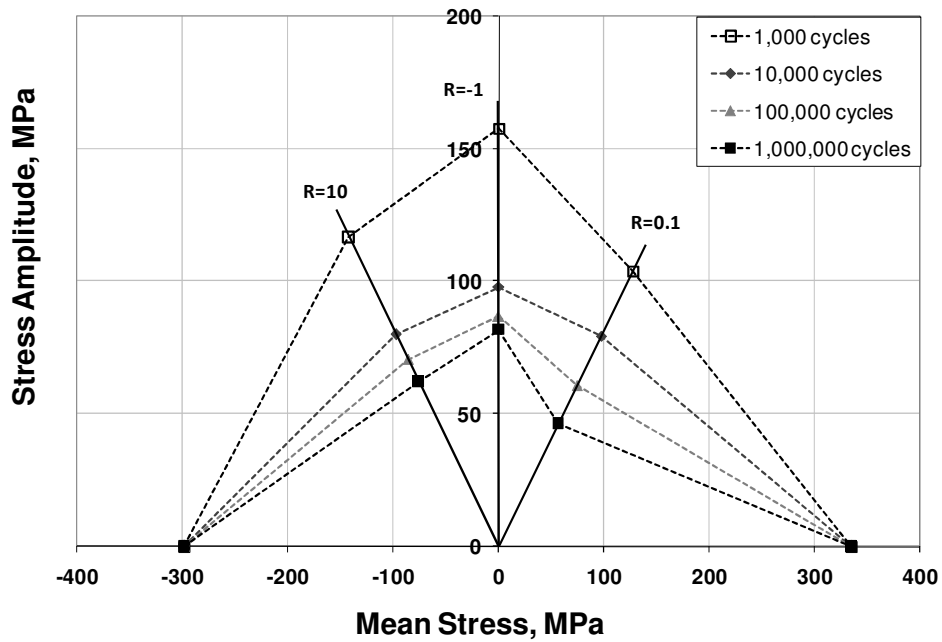


Figure 4: An example of a Goodman diagram.

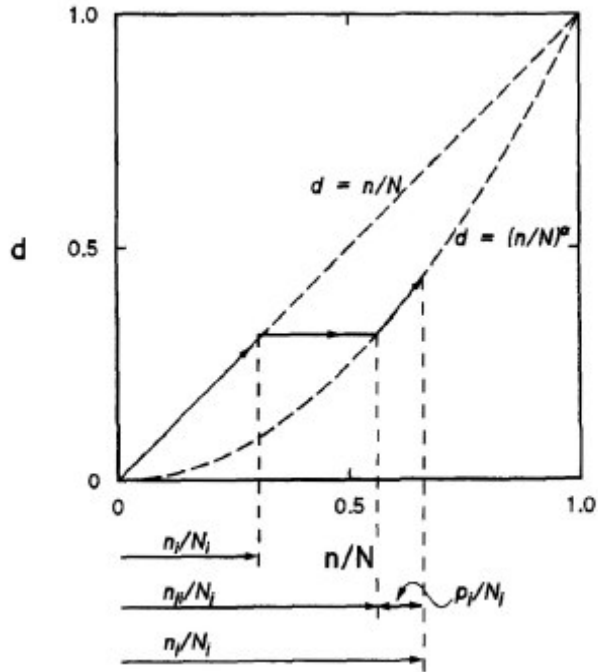


Figure 5: Illustration of linear (Miner's rule) and nonlinear damage laws. (Excerpted from [21]).

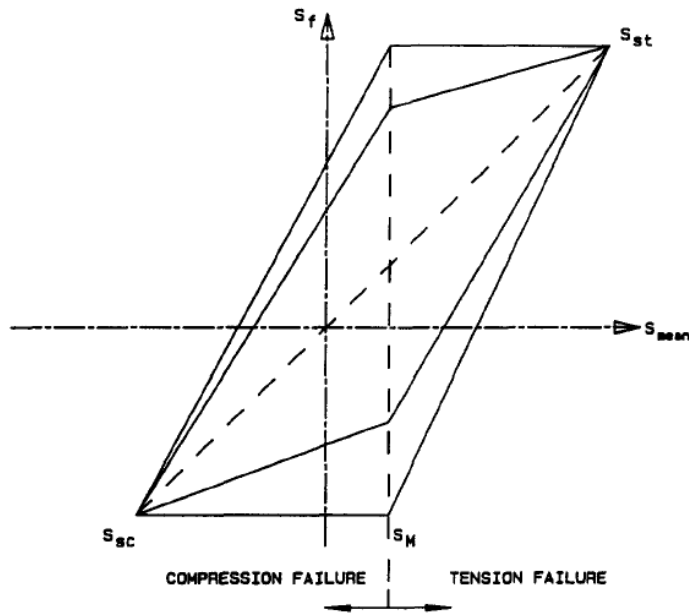


Figure 6: An example of a fatigue failure envelope for a hypothetical material expressed in terms of mean stress and stress amplitude. (Excerpted from [51]).

2.3. Long-term moisture damage in glass-reinforced composites

For engineers that are designing composite structures that will see service in wet conditions, the absorption of water by the composite is of great concern since the presence of moisture causes many deleterious effects on the composite. The problem of moisture ingress has been studied extensively; researchers have investigated the rates and degrees of moisture absorption for a multitude of fiber and matrix materials, ply orientations, stress states, and aqueous (as well as non-aqueous) environments [56-61], and have developed various models to predict these moisture profiles [62-64]. Swelling and cracking of the matrix are common problems, especially at elevated temperatures, as is the chemical degradation of the matrix. Schutte [65] showed that hydrolysis of a bisphenol-A epoxy matrix in warm water results in the breaking of the ester bonds, reducing the strength of the inter-chain bonds. The interface between the fibers and matrix also can be mechanically and chemically stressed and compromised. The glass fibers themselves, too, are degraded by the presence of moisture. (Note, it is this type of damage that will primarily be focused on in the later sections of this chapter and in a portion of the proposed work).

Much research has gone into characterizing the loss of various material properties as functions of the degree of moisture absorption, the time of exposure to the moisture, and the ambient temperature conditions to which the material is exposed during saturation and during testing. Often, this characterization is such that the contributions of the various damage modes (matrix, interface/interphase, glass fiber) are lumped together, and the combined effects (loss of strength, stiffness, etc.) are measured simply as a loss in initial material properties.

Often, glass reinforced polymer composites are used in civil structural applications, either as primary structural material, or as external stiffening or repair elements for steel or concrete structures. Helbling et al. [66] have investigated the synergistic effects of moisture and load on E-glass GRPCs used in the latter function, specifically as externally applied rehabilitation elements for concrete bridge slabs. These materials were immersed in deionized water for 100 weeks and their strength degradation was recorded at regular intervals. During the immersion, the samples were subjected to uniform bending strains at various degrees of the initial failure strain. It was seen that for moderate strain rates, the moisture uptake was not affected by the strain. However, at approximately 45% of the ultimate strain, the samples showed an increase in

both the rate and final level of water uptake, and a drastic decrease in strength compared to samples conditioned at lower strain levels. Based on the results, the authors conclude that this is a result of gross material degradation, especially at the interface regions.

(It should be noted that Helbling et al. made informal predictions on the material strength far into the future using an Arrhenius-type relation at a given temperature. As will be noted below, this may not be an accurate prediction method given the uncertainty in the temperature value.)

Ellyin and Maser [67, 68] have characterized the hygrothermal damage induced in filament-wound E-glass/epoxy composites (similar to those used by the author of this proposal and described below) conditioned in distilled water at two temperatures, namely room temperature (approximately 20°C) and an elevated 50°C condition. The samples were tested under various bi-axial load ratios, as well as pure hoop loading. In this study, Ellyin and Maser considered sample failure not to be the complete mechanical failure of the specimen, but instead at a “functional failure” level where the specimen leaked. They concluded that plasticization and hydrolysis of the matrix resulted in a reduced composite stiffness; however, the swelling of the matrix after moisture saturation induced compressive stresses in the material, leading to matrix crack closure, and thus an increase in the functional failure load for certain bi-axial loading conditions, specifically those in which the hoop stress was greater than the axial stress.

Ellyin and Maser also performed post-mortem microscopy on the failed samples in order to gain insight into the damage and failure modes and their relation to the moisture conditioning. They found that the fibers in the vicinity of the failure showed more residual resin attached to dry samples than to wet ones, and greater resin attachment for the 20°C case than the 50°C case, suggesting that both moisture and elevated temperature (in the presence of moisture) drive the degradation of the matrix/fiber interface.

Chiou and Bradley [69, 70] have also studied moisture-induced damage in helically wound e-glass/epoxy laminates, though they used a seawater bath instead of distilled water. They tested some samples under a monotonically increasing hydrostatic load until failure, and others using a 14-cycle load/unload program before conducting creep rupture tests. In the burst tests, a significant decrease (~20%) in burst strength was seen for the moisture conditioned samples. Surprisingly, however, there was no significant difference seen between dry samples and wet

samples during the stress rupture tests, though the authors attribute this to the presence of manufacturing-induced voids.

Post et al. [71] attempted to develop static strength knockdown factors that could be applied to predict fatigue life of E-glass/vinyl-ester composites that were hygrothermally aged to saturation and then tested at an R-ratio of 0.1 (tension-tension). Half of the moisture-aged samples were tested under ambient (dry) conditions, while the others were tested in a fluid cell that kept the sample gage length submerged during the testing. They found that while hygrothermal aging did reduce the initial strength of the material, they achieved longer fatigue lifetimes for these samples than for samples stored under dry conditions. This is most likely due to the cooling effect of the fluid cell, which was maintained at 80°F during the testing. The samples fatigued under dry conditions experienced greater viscoelastic heating during the tests, which were performed at a frequency of 10Hz. Past experience with fatigue testing at this frequency has shown that the samples can reach significantly higher temperatures during the test. It is unknown to what extent this may reduce the fatigue lives of the samples.

Often when characterizing strength loss of composites due to hygrothermal aging, researchers will fit their data to an Arrhenius equation, of the form of equation 14:

$$a = Ae^{-\frac{E}{RT}t} + a_0 \quad (14)$$

where a is a material property such as ultimate strength, A is a constant, E is the Arrhenius activation energy, R is the universal gas constant, T is the temperature, t is time, and a_0 is the initial material property before aging. These models presuppose that the mechanism of glass degradation is a chemical process with an associated, measurable activation energy.

Liao et al. [72] suggested that for pultruded vinyl-ester GRPs, 2,400 hours soaking in water at 75°C is equivalent to 3,900 hours at room temperature; this corresponds to an acceleration factor of 1.6 corresponding to $E \sim 7 \text{ kJ mol}^{-1}$ if 20°C is assumed for room temperature. These samples were conditioned at zero stress for given amounts of time and then cyclically loaded in four-point bending tests at various stress levels.

Bank et al. [73] suggested that Arrhenius type relationships should be used to predict service lifetimes, although since he proposed using plots of time and/or property retention vs. reciprocal

temperature, technically such plots are not Arrhenius plots as the y-axis is not the natural log of a rate constant and thus activation energy cannot properly be derived from them.

Khennane [74] invoked surface flaw growth as a cause of stress corrosion (similar to the approaches outlined in later portions of this chapter) but did not model residual strength vs. time. The model required 10 input parameters and predicted time to rupture, instead.

Chin et al. [75] used Litherland's and Proctor's [76] procedure to study ageing of pultruded vinyl ester and isopolyester at room temperature to 80°C in water, salt water and alkaline pore solution (they were studying glass reinforced concrete). No activation energies were derived, although they did note that the slopes of their Arrhenius-like plots were different, implying that different mechanisms applied in each ageing medium.

Iskander et al. [77] studied degradation of glass-reinforced HDPE at three temperatures and various strain levels and attempted to apply Arrhenius analysis to the results. They did not see sufficient strength loss over the timescales of their experiment (5000h) to get reliable results. No activation energy was derived, however, as the plots presented were not truly Arrhenius plots.

In their review, Nkurunziza et al. [78] reviewed studies that use Arrhenius or pseudo-Arrhenius relationships to model strength loss in GRP. They quoted phenomenological exponential relationships derived by Vijay and Gangarao [79], i.e. equation 15

$$\frac{N}{C} = 0.098e^{0.0558T} \quad (15)$$

where N is the age in days, T is the aging temperature in Fahrenheit and C is the number of days of aging at temperature T . This was developed with respect to conditions in West Virginia, USA, where the average annual temperature 11.7°C, thermodynamic average temperature ~17°C. However, as Purnell has pointed out, these approximations concerning weather temperatures can lead to significant errors [80].

Equation 15 is not a true Arrhenius relationship but it approximates to an activation energy of around 100-110 kJ mol⁻¹ over the accelerating temperature ranges of interest (35-80°C).

Other researchers have used fracture mechanics ideas to develop models for the prediction of fiber damage. In investigating the moisture-induced degradation of silica optical fibers, Muraoka

et al. [81] developed a lifetime prediction model for these fibers based on sub-critical crack growth ideas expressed by Ritter et al. [82]. They assumed that the flaws grow according to the following power-law relation for crack velocity, equation 16:

$$\frac{da}{dt} = AK^n \quad (16)$$

where K is the stress intensity factor and A is a constant dependent on the environment, N is the stress corrosion susceptibility constant or the fatigue constant and is dependent on the environment. If the fiber is subjected to a constant stress σ_s , then the time to failure t_f is given by equation 17:

$$t_f = BS_i^{n-2} \sigma_s^{-n} \quad (17)$$

where S_i is the fracture strength in an inert environment, and B is given by equation 18:

$$B = \frac{2}{AY^2(n-2)K_{IC}^{n-2}} \quad (18)$$

where Y is a constant dependent on the flaw shape and K_{IC} is the fracture toughness in an inert environment.

In order to apply this model, the parameters n , B , t_f and S_i need to be measured or determined from curve fitting. N is determined by fitting equation 17 to the empirical static fatigue data.

The above are examples of empirical data that documents the overall strength loss of composites subjected to an aqueous environment. The remainder of this chapter will focus on the moisture-induced degradation of the glass fibers themselves, and the strength loss of glass-reinforced composites as a function of this glass fiber degradation process, as opposed to matrix and interface damage.

2.3.1. Moisture-induced degradation of glass fibers and the static fatigue model

The static fatigue model and other considerations of the degradation of glass fibers from the literature will be addressed in the literature review section of Chapter 6.

2.3.2. A method of GRP life prediction adapted from a GRC model

A description of this model is given in the literature review section of Chapter 6.

3. Paper: Post-curing Effects on Marine VARTM FRP Composite Material Properties for Test and Implementation

The following paper was submitted to and published in a special issue of the Journal of Engineering Materials and Technology - Transactions of the ASME [83] in 2006. Formatting and typesetting have been changed for consistency with the rest of this document.

Post-curing Effects on Marine VARTM FRP Composite Material Properties for Test and Implementation

*Jason J. Cain, Nathan L. Post, John J. Lesko, Scott W. Case
Materials Response Group
Department of Engineering Science Mechanics*

*Yin-Nian Lin and Judy S. Riffle
Department of Chemistry*

Virginia Polytechnic Institute and State University

*Paul E. Hess**
Naval Surface Warfare Center, Carderock Division

**Note: The opinions expressed herein are the views of the authors and should not be interpreted as the views of the Naval Surface Warfare Center or the Department of the Navy.*

3.1. Abstract

Structural composites are increasingly being utilized in many large naval and civil structures where it is vital that their long term performance be predictable and their variability definable over the life of the structure. However, these properties may be influenced by the degree of cure of the resin, particularly for room temperature cured systems. Thus, this investigation defines the post-cure effects on E-glass/vinyl ester fiber-reinforced polymer (FRP) composites manufactured using the Vacuum-Assisted Resin Transfer Molding (VARTM) method, which are typical of those used by the US Navy for ship structures. The composites are differentiated by varying levels of post-cure temperature and duration, and examined for the effects of advancing cure at various points in the time after post-cure. Pseudo-quasi-isotropic $[0/+45/90/-45/0]_S$ and angle ply laminate $[\pm 45]_{2s}$ samples from each level of post-cure are examined at 1, 10, 30, 100, and 300 days after post-cure in order to track strength, stiffness, failure strain, creep, and fatigue performance as functions of time.

In parallel, the matrix polymer is inspected using FTIR (Fourier Transform Infrared Spectroscopy) to directly assess the degree of conversion. Dynamic mechanical analysis and shrinkage measurements are also undertaken to assess the T_g and the amount of shrinkage

undergone during post-curing, as well as the advancing of the level of cure during the prescribed aging time.

Results suggest that the degree of conversion is limited to 80% for the vinyl ester oligomer and 90-95% for styrene following a post-cure of 93°C. It is observed that after 300 days of ambient storage the non-post-cured samples approach the degree of conversion exhibited by those post-cured at 93°C, as measured by FTIR. Resin dominated quasi-static properties are greatly affected by the degree of cure whereas fiber dominated properties are not. Where the degree of cure is comparatively low, viscoelastic properties cause greater changes in creep response as well as influencing fatigue performance.

Keywords: Post-cure, vinyl-ester, VARTM, composite, FTIR, conversion

3.2. Introduction

The degree of cure of vinyl ester resin composites produced by the VARTM process has recently received a great deal of attention as it relates to mechanical properties and reliability of marine composite structures. Understanding the degree of cure and effect of vitrification on ambient temperature cured E-glass/vinyl ester resin composites and the resulting thermal-mechanical properties are of critical importance to the design and reliability of structures formed from these materials. In particular, we seek to understand how the degree of cure influences the evolution of properties over time and how to develop test protocols for characterizing basic material properties, durability, and variability for the purposes of design. Secondly, we are also concerned to define what degree of cure is acceptable for the purposes of material stability and durability relative to the available vinyl ester polymers and practical curing conditions for large structures.

3.3. Literature Review

When examining the literature regarding degree of cure in thermosetting materials, two distinct classes of review have been addressed; epoxy resins systems and styrenated resin systems. There

exists a large body of work which examines the step growth polymerization aspects of degree of cure for epoxy/amine thermosetting polymers [1,2,3]. Within this work, T_g has been shown to correlate closely with the degree of cure; however, the relationship to microstructure of the network is not clearly known. The other area which has received recent attention deals with the cure kinetics of free radically cured systems like those formed by the copolymerization of styrene monomer and a dimethacrylate monomer based on the diglycidyl ether of bisphenol-A (e.g. vinyl ester resins). In this case the formation of these networks is complicated by presence of additional mechanisms uncharacteristic of networks formed through step growth polymerization. Verghese et al. [4] have been successful in expanding the work of Gillham [1,2,3], Pascault [5], and Dibenedetto [6] to define the degree of cure based on endothermic arguments which attempt to predict the T_g for compatible blends. In this case the thermoset is treated as a blend of completely crosslinked polymer and monomer. The noted approaches all result from the philosophy proposed by Couchman [7]. More complicated approaches have been proposed and compared in an effort to model T_g as a function of conversion [8].

While these approaches describe completion of cure through the averaged effect of glass transition temperature evolution, they are an indirect measure of the network structure formed. Moreover, the use of T_g as a metric has its detractions given that DSC (differential scanning calorimetry) and DMA (dynamic mechanical analysis) advance the evolution of cure during the process of measurement [4]. Thus, more direct measurements have been made through FTIR (Fourier Transform InfraRed spectroscopy) where the disappearance of styrene and methacrylate C=C are monitored [9,10]. Yet studies relating these to the network structure and the resulting mechanical properties are rare. Li et al. [11,12] and Ziaee et al. [13] have made attempts to connect structure with property as it relates to the degree of cure. Efforts to examine mechanical properties of vinyl ester glass composites laminates by Puckett et al. [14] showed that viscoelastic phenomena are enhanced at reduced degrees of cure.

Yet none of these studies have fully examined the spectrum of properties affected by the state of cure in these systems, nor studied if, and how, long-term properties are changed. Thus, this interdisciplinary study collectively examines and connects the state of cure and the mechanical performance of VARTM E-glass/vinyl ester laminates with and without various levels of post-cure.

3.4. Materials, Fabrication and Post-curing

A total of eight panels were fabricated using the VARTM process. Of these, four were 35”x35” (0.89m x 0.89m) pseudo-quasi-isotropic panels, fabricated with a 10-layer [0/+45/90/-45/0]_s lay-up. These panels were used in both ultimate tensile strength tests and tensile fatigue tests. The four remaining panels measured 22”x22” (0.56m x 0.56m), and were fabricated with an 8-layer [\pm 45]_{2s} lay-up. These panels were used to investigate shear properties of the material under quasi-static tension to characterize shear (resin dominated) properties. The DMA temperature sweeps and DMA creep tests were performed on small samples taken from these panels. A list of panel designations is given in Table 1.

All panels were fabricated using a 24-oz. plane weave E-glass (55% warp, 45% weft) and a brominated vinyl-ester resin (38% styrene). In preparing the resin for VARTM, the following procedure was followed. First, the resin was divided into two roughly equal volumes in separate containers. To one of these portions 0.2% Cobalt Napthenate catalyst (weight percent of total resin volume used) was added. To the other portion 0.05% 2,4-Pentanedione 99% (retarder) and 1.25% Norox MEKP-925H Peroxide (peroxide initiator) was added. Each portion was mixed thoroughly and independently, before the portion containing the catalyst was poured and mixed with the portion containing peroxide and retarder. The entire batch of resin, with additives, was mixed thoroughly for four minutes using a propeller-type paint mixer attached to a Master Mechanic 1/3 hp variable-speed hand drill. It is from the beginning of this final mixing that all subsequent time measurements reported in this paper are made. After final mixing, the resin was degassed with vacuum using a Welch Model 1400 vacuum pump; the degassing process took approximately five minutes and infusion began immediately thereafter. Thermocouples were used to record temperature histories of each panel during the VARTM process. The thermocouples were located several inches from the center of one edge, and were centered through the thickness of the panel.

Each panel was allowed to sit overnight after fabrication and prior to demolding. The following morning, panels were cut into several smaller sections to allow for post-curing at the prescribed temperature and time as described in Table 1. Following the post-cure, specimens were

machined and stored overnight at room temperature, and on the following day, testing began (designated as Day 1 testing). Testing was repeated on Days 10, 30, 100, and 300.

3.5. Experiments

3.5.1. Degree of Cure Characterization

The FTIR technique was used to track the C=C styrene and methacrylate double bond conversion during the process of vinyl ester network formation from the free radical curing process, as illustrated in Figure 7. This method serves as a direct and quantitative means of assessing the degree of cure and is valuable in characterizing the network structure as it evolves due to time and thermal history. This is in contrast to thermal-mechanical analysis such as DMA, where a relative and non-quantitative measure of degree of cure is inferred by the movement of T_g . The FTIR studies were performed on small gram scale quantities of the matrix resin alone and scanned at selected intervals during the first several hours after initiator was mixed into the resin. FTIR spectra were collected using a Nicolet Impact Model 400 instrument equipped with a controlled temperature cell (Model HT-32 heated demountable cell used with an Omega 9000-A temperature controller). One drop of the reaction mixture was placed between two NaCl plates, which were then placed in a preheated controlled temperature cell in the FTIR. The heights of the infrared absorbencies at 943 and 910 cm^{-1} , corresponding to the methacrylate and styrene double bonds respectively, were monitored quantitatively and used to calculate reaction conversion. A small background absorbance assigned to the vinyl ester backbone overlapped the absorbance at 943 cm^{-1} (about 25 percent of the initial absorbance at 943 cm^{-1}). Therefore, all spectra were subtracted by a spectrum where the conversions of methacrylate and styrene double bonds were complete. Due to the limited thermal control in FTIR, scans were conducted at 22°C and did not include the effects of exotherm seen during cure. An additional study at 35°C (also conducted isothermally) showed no significant difference in the degree of conversion and is not presented here.

3.5.2. Viscoelastic Characterization

Dual-cantilever DMA tests [15] were performed on samples taken from each $[\pm 45]_{2s}$ panel, using a TA Instruments Model 2980 DMA instrument. The samples were cut using a diamond saw to approximately 1.4" x 0.18" x 0.10" (35mm x 4.5mm x 2.5mm) with the thickness of the panel in the 0.18" direction. Two types of viscoelastic characterizations were conducted. First, to characterize viscoelastic transition, temperature sweeps from 30°C to 200°C were undertaken. The samples were heated at a rate of 5°C per minute (designated First Heat), allowed to air-cool to 35°C, and heated again at 5°C/min. to 200°C (designated Second Heat). A displacement amplitude of 15 μ m and frequency of 1Hz were used for all runs. (It should be noted here that for situations where the T_g is below the testing temperature, the possibility that the cure will advance during the course of the test is likely, thus making the T_g determined by this method for under cured samples suspect.) Secondly, in an effort to examine long term dimensional stability under sustained load, isothermal creep characterization at 30°C for 2 hours with an applied stress (in bending) of approximately 1740 psi (12 MPa) was examined.

3.5.3. Quasi-Static Mechanical Characterization

Ultimate tensile strength (UTS) tests [16] were performed on specimens taken from the four pseudo-quasi-isotropic panels. The specimens were 6" (0.152m) long and 1" (0.254m) wide, and were cut slightly oversized from the panel using a water-cooled diamond saw. In order to provide accurate and consistent specimens, the long edges of the samples were ground to within 0.001" of the nominal 1" width, with edges parallel to within 0.003" over the 6" length. In addition, the grinding provided a very smooth surface along the edges, free from defects arising from cutting. On each testing day, the UTS testing consisted of destructive quasi-static tension tests performed on 5 replicates using an MTS Model 810 20-kip servo-hydraulic load frame and an MTS 407 Controller. Load ramp rates were set at 150 lbf/sec (667 N/sec), and strain data were collected with an extensometer with a 1-inch gauge length. In this way, load-strain data were collected for each sample. Prior to testing each sample, the width and thickness were

measured in several locations using hand held calipers and an average value was recorded to determine the bulk cross-sectional area. This area was then used in combination with the load and strain data to calculate the stress and elastic modulus of each specimen.

The shear tests [17] were performed on specimens taken from the four $[\pm 45]_{2s}$ panels. The samples were 9" (0.229m) long and 1" wide. As with the UTS samples, the samples were ground to 1.000" width for consistency and accuracy. On each day of testing, five replicates from the $[\pm 45]_{2s}$ panel were subjected to quasi-static tension loads to failure, at a load rate of 100 lbf/sec (445 N/sec). Shear strain data were collected for each sample using two 120Ω , $\frac{1}{2}$ " gage length strain gages mounted perpendicularly on the specimen in the transverse and longitudinal directions and connected to a Wheatstone bridge. Together with the load data taken from the MTS controller, the strain data allowed the determination of the initial shear stiffness. The engineering shear modulus was computed based on the initial cross-sectional area and the tensorial strains measured. Since these data were taken from panels at each post-cure condition and time, it was possible to investigate the effect of these variables on the matrix shear modulus, as well as its effect on the shear breaking strength of the samples.

3.5.4. Laminate Fatigue Characterization

Tension-tension $R=0.1$ sinusoidal fatigue tests [18] were performed at a maximum stress level of 21.6 ksi (149 MPa) (approximately 45% of the ultimate tensile strength) and at 10 Hz using the same load frame used for the quasi-static tests. Straight sided 6"x1" specimens were used without end-tabbing. Strain was measured with a surface-mounted 1" gage length extensometer, and surface temperature was measured using a non-contact infrared temperature sensor near the center of the specimen. The dynamic stiffness of each specimen during fatigue was calculated using the load and strain data at the maximum and minimum of each loading cycle.

3.6. Results and Discussion

3.6.1. Panel Temperature Histories

The panel temperature histories recorded by the thermocouples clearly demonstrate the exotherm associated with cure, as seen in Figure 8. (Note that the temperature history for panel 4501-NPC was not successfully recorded due to data acquisition problems.) It is not understood why panel PQ01-NPC experienced such an increased exotherm compared to other panels. The difference may be the result of slightly higher resin temperature for panel PQ01-NPC on that particular day leading to an increase in the reaction rate early in the infusion process. Such an increase in reaction rate may have led to an increased exotherm, which in turn speeded the reaction rate. However, it appears that panel 4503-82 had a similar resin temperature early in its history, and did not experience this large and early peak in exotherm.

3.6.2. FTIR Matrix Cure Measurements

FTIR results reveal the degree of double bond conversion for vinyl ester and for styrene, and are shown in Figure 9. The post-curing process begins at 20 hours and concludes at 24 hours, resulting in the rapid increase in the degree of conversion seen for the three post-cured samples. The rate of increase of double bond conversion for the post-cured samples levels off again after post-curing. The degree of conversion at this time is nearly complete for the styrene, at about 90-95%, and approximately 80% for the dimethacrylate. The non-post-cured sample, which has undergone less conversion after 24 hours than the other samples, steadily increases in conversion and begins to approach the post-cured samples near day 300.

3.6.3. Viscoelastic Characterization

Storage modulus results (first heat) from one DMA test from each post-cure condition at Day 1 are presented in Figure 10, clearly showing that post-curing has advanced the T_g significantly. (The storage modulus, E' , is defined as the real portion of the complex modulus that is in phase with the stress.) Also, there is an additional plateau in the storage modulus curves from panels 4501-NPC and 4502-71, which is absent from those of the more highly post-cured panels, indicating the presence of a phase of uncured material. The presence of these two transitions is indicative of that described by Verghese et al.[4], where the first transition indicates the T_g of the uncured oligomer phase within the vitrified resin and the second is more nearly characteristic of the fully cured system.

The normalized storage modulus curves for the non-post-cured panel at all testing days are shown in Figure 11. Over the span of 300 days, the first transition has shifted more than 20°C as a result of advancing cure. This agrees well with the FTIR results which showed a slow room-temperature increase in conversion in the resin with time. Storage modulus curves taken from other panels, however, show a lessening of this effect with increasing post-cure. Panels 4503-82 and 4504-93 (82°C and 93°C) show no detectable change in T_g over 300 days. These results confirm that post-curing has advanced the degree of cure sufficiently to induce stability in the degree of cure of the resin when these composites are stored for extended periods at room temperature.

Second heat data from panel 4504-93, however, suggest that even that panel, post-cured at 93°C, is not entirely stable at elevated temperatures as shown in Figure 12. Comparing the first and second heat data for 2 replicates from panel 4504-93 on day 300, it is clear from the tan delta data that the T_g advances approximately 10°C between first and second heats, demonstrating that the panel experiences additional curing as a result of the testing ($\tan \delta = E'/E''$, where E' is the storage modulus, and E'' is the loss modulus.)

Isothermal creep tests confirm the observations from above that non-post-cured samples will advance in cure over 300 days as shown in Figure 13, in which panel 4501-NPC undergoes a decrease in creep response as cure evolves over time. More highly post-cured specimens, however, do not appear to advance in cure significantly with time at room temperature.

3.6.4. Tensile Characterization of Pseudo-Quasi-Isotropic Laminates

In the quasi-static tension tests on pseudo-quasi-isotropic samples strain, modulus, and breaking strength were measured. These parameters are primarily fiber-dominated, and so were not significantly affected by the degree of cure of the matrix. Mean initial modulus and breaking strength values are given in Figure 14 and Figure 15, respectively. Figs. 8 and 9 clearly show that neither the initial post-cure nor the time since post-cure have an effect on the results. A representative stress-strain plot is given in Figure 16, which plots the results for one sample from panel PQ04-93 on each day of testing through three hundred days.

3.6.5. Characterization of Angle Ply Laminates

In contrast to the pseudo-quasi-isotropic samples, the tensile properties of the angle ply samples are markedly affected by degree of cure since these properties are matrix-dominated. Initial modulus values of the samples are shown in Figure 17. A clear trend is evident of increasing stiffness with increasing degree of initial post-cure up to a post-cure temperature of 82°C. The 93°C post-cure, however, does not show significantly different initial modulus compared to the 82°C post-cure. Values of breaking strength show a stronger dependence on post-cure, as seen in Figure 18. Up to 82°C, the breaking strength values increase significantly with increasing post-cure. There is, however, a substantial reduction in shear breaking strength when the post-cure temperature is raised to 93°C, potentially indicative of a more complete degree of cure and a subsequently more brittle network.

3.6.6. Tensile Fatigue Characterization

The dynamic stiffness (stiffness reduction) and temperature history data are shown in Figure 19 for representative samples from testing day 1. Samples from panel PQ01-NPC (no post-cure) showed markedly lower fatigue life than samples from panels PQ02-71, PQ03-82, and PQ04-93, suggesting that some degree of post-cure (at least 71°C for 2 hours) has a large positive effect on

cycles to failure. The non-post-cured samples from PQ01-NPC experience greater fatigue lives after 300 days of storage, again suggesting slow room temperature curing. This effect can be seen in Figure 20, which shows cycles-to-failure data for each panel on each day of testing. It is also worth noting that samples from PQ01-NPC experienced more significant viscoelastic heating and a greater rate of increase of temperature with cycles during fatigue than did the post-cured samples.

3.7. Summary and Conclusions

Examination of ambient cured VARTM E-glass/fire retardant bisphenol-A epoxy vinyl ester resin composites show that their mechanical properties are significantly affected by the degree of cure and conversion of resin constituents. Given low degrees of cure (e.g. no post-cure) following fabrication, the laminates change significantly over 300 days in terms of degree of conversion as well as viscoelastic properties, static resin dominated mechanical properties and fatigue performance of fiber dominated laminates. FTIR testing has shown that the degree of conversion in the non-post-cured resin approaches that of post-cured resin after storage at room temperature for 300 days.

DMA tests indicate that non-post-cured samples and those post-cured at 71°C both contain a phase of uncured material, as evidenced by an additional plateau in the storage modulus curves. Samples from the 82°C and 93°C post-cure do not exhibit this additional plateau. However, tan delta data show that even the samples post-cured at 93°C are still not fully cured, since second heating to 200°C shifts the T_g by 10°C. Creep results show that post-curing greatly reduces the creep behavior of the matrix, and the non-post-cured samples show decreasing creep response with time at room temperature. Both of these results suggest an increase in crosslink density with either time or post-cure, but little or no change in the material after post-curing, reinforcing the FTIR results. Among the three non-ambient post-cure conditions, successively higher post-cure temperatures result in moderate decreases in creep response.

Ultimate tensile strength tests performed on pseudo-quasi-isotropic samples show no significant difference between non-post-cured and post-cured samples with respect to ultimate tensile

strength, initial modulus, or strain at failure. Shear tests on $[\pm 45]_2$ s samples indicate that both initial shear modulus and ultimate strength of these samples is affected by the degree of post-cure. There is a moderate increase in initial shear modulus with successively higher post-curing, up to 82°C. Values for 93°C samples were not significantly different from those at 82°C post-cure. Shear strength values show a more pronounced trend towards greater values with increasing post-cure temperatures, again up to 82°C, before dropping off at a post-cure temperature of 93°C. Shear strength values for panel 4504-93 are significantly lower than those for panel 4503-82 and are approximately equivalent to those found for panel 4502-71.

Fatigue testing has shown that post-curing dramatically increases the cycles to failure of samples tested at 10 Hz, $R=0.1$. Non-post-cured samples experienced much more viscoelastic heating during testing, and failed after approximately half the cycles compared to post-cured samples. The fatigue lifetimes for these samples increased with time through 300 days but still did not reach the lifetime of post-cured samples after 300 days. It is not known what effect the increased heating of the non-post-cured specimens has on the fatigue life. The post-cured samples did not show significant differences in fatigue life, either as a function of the degree of post-curing, or with time.

As a result of room temperature curing, resin-dominated properties in the composites with low or no initial post-cure begin to approach the properties of more highly post-cured composites, though the former still fall well short of the latter over the span of three hundred days. In many practical applications, the need for structural composites to have stable and predictable mechanical properties necessitates the use of a post-cure regime. For the E-glass/Vinyl-ester resin composites examined in this study it has been found that a post-cure of at least 82°C for 2 hours is sufficient to bring about stability in the state of cure and the resulting mechanical properties.

3.8. Acknowledgements

The authors would like to gratefully acknowledge the support of the Office of Naval Research (technical point of contact Mr. Patrick Potter) through grant number N00014-03-1-0151.

3.9. Figures and Tables

Table 1: Post-cure Conditions and Panel Designations

Panel designations	Lay-up	Post-cure conditions
PQ01-NPC	[0/+45/90/-45/0]s	No post-cure
PQ02-71	[0/+45/90/-45/0]s	71°C (160°F) for 4 hours
PQ03-82	[0/+45/90/-45/0]s	82°C (180°F) for 4 hours
PQ04-93	[0/+45/90/-45/0]s	93°C (200°F) for 4 hours
4501-NPC	[±45]2s	No post-cure
4502-71	[±45]2s	71°C (160°F) for 4 hours
4503-82	[±45]2s	82°C (180°F) for 4 hours
4504-93	[±45]2s	93°C (200°F) for 4 hours

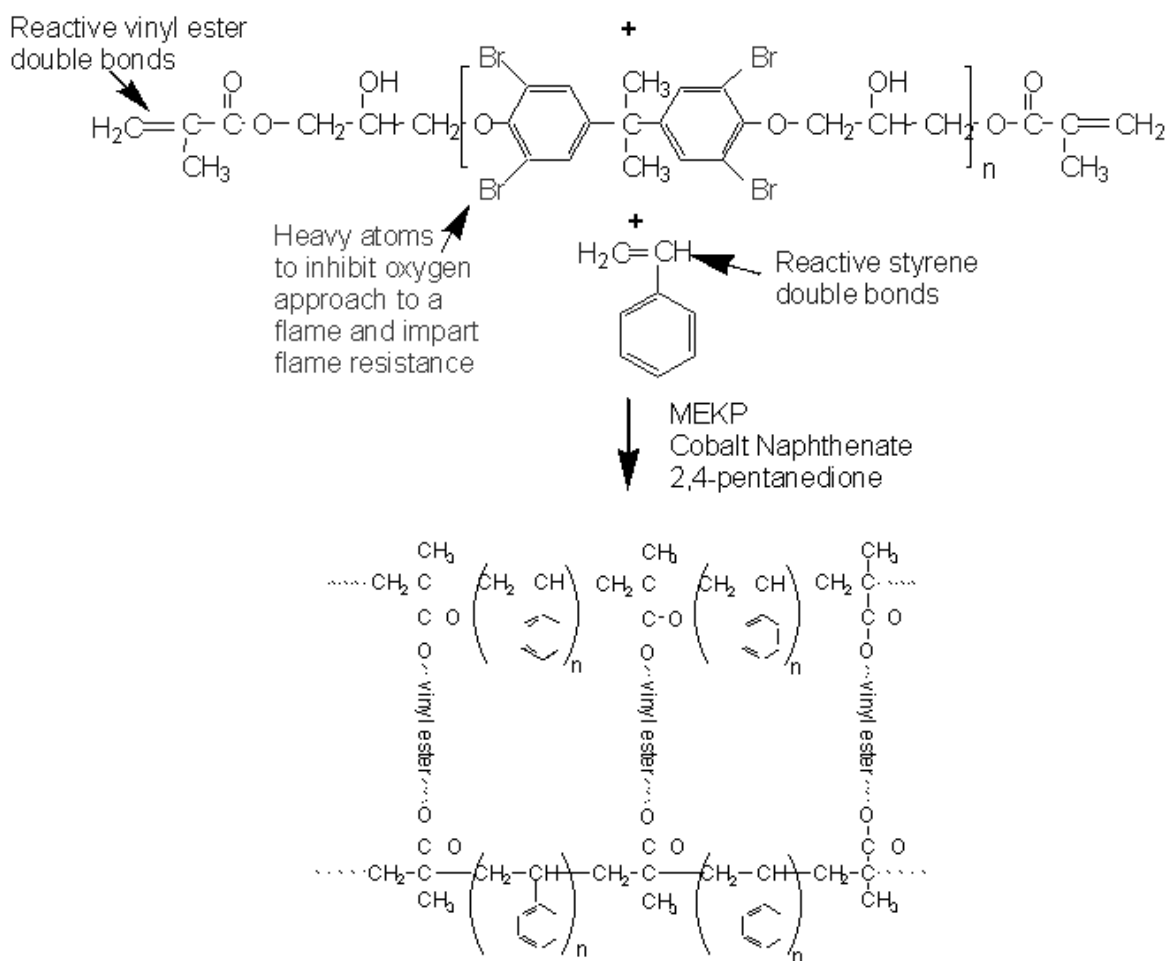


Figure 7: Resin oligomer and styrene monomer reaction to the vinyl ester network. The disappearance of styrene and methacrylate C=C are tracked by FTIR to assess the degree of cure quantitatively.

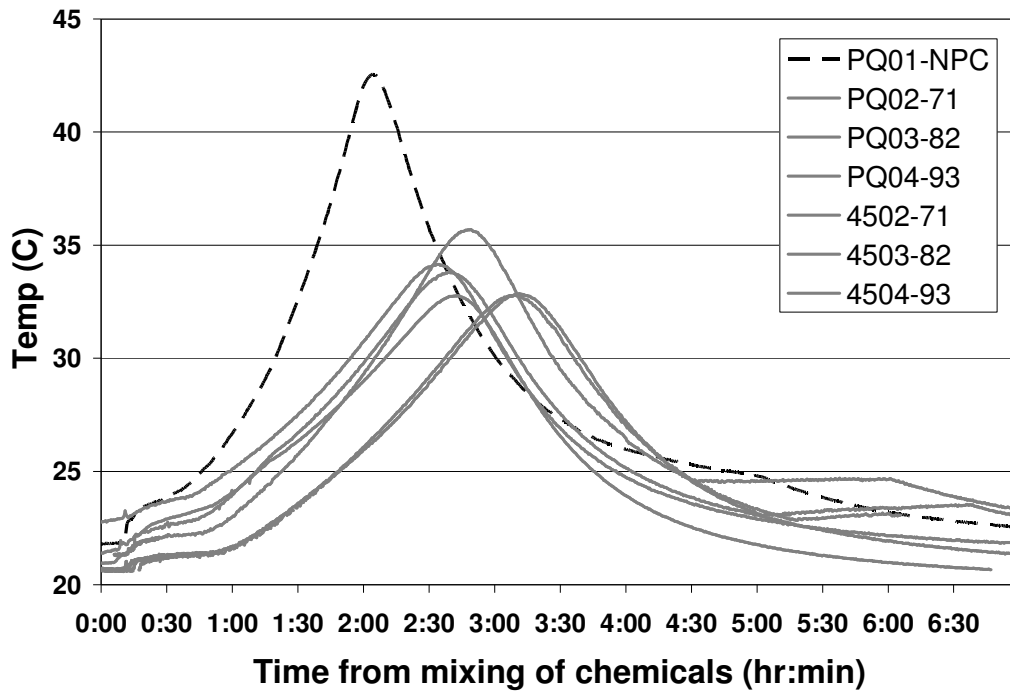


Figure 8: Cure temperature profile for all panels

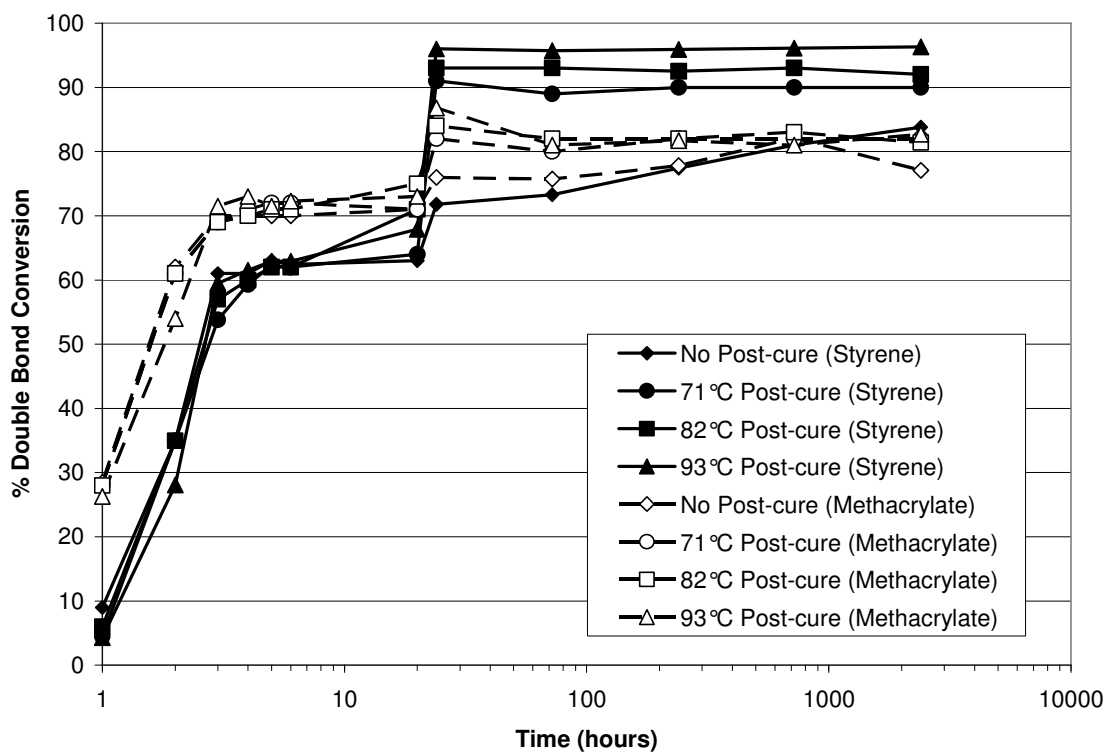


Figure 9: Vinyl ester and styrene conversion with time

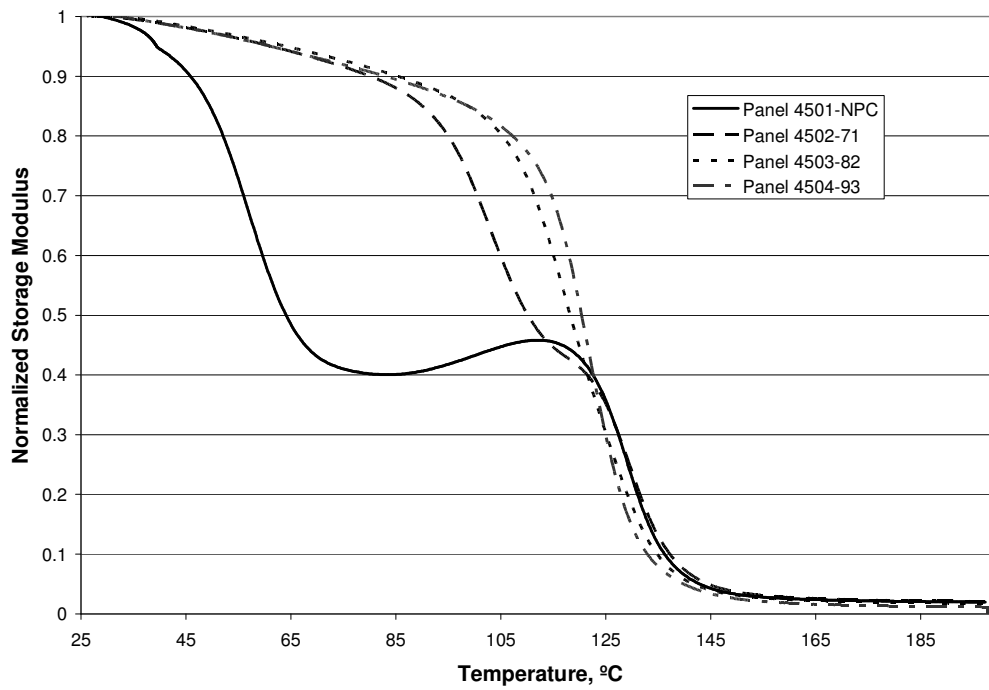


Figure 10: DMA storage modulus curves for all panels on day 1

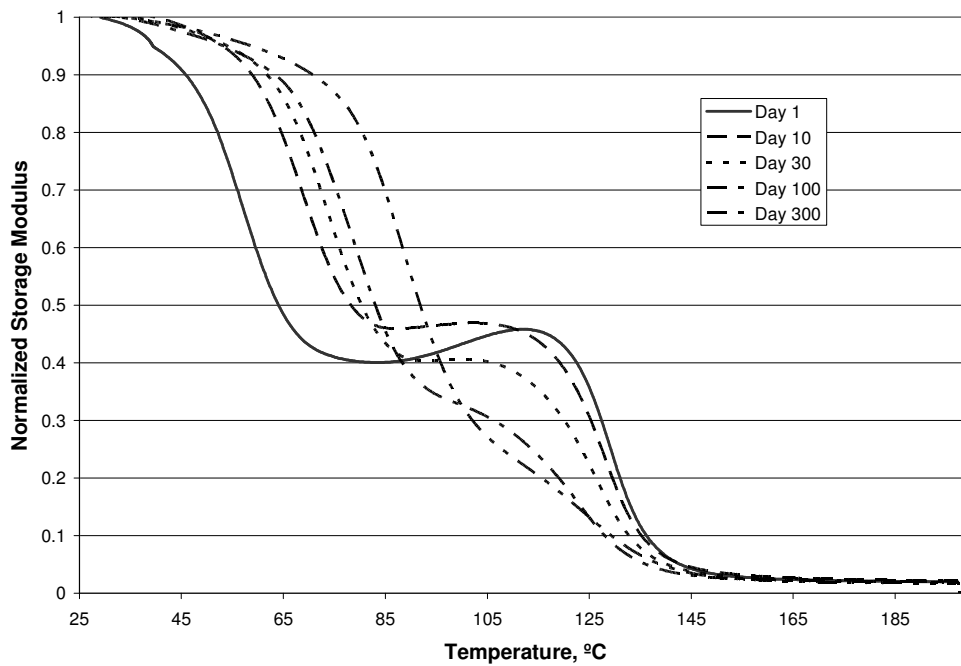


Figure 11: Normalized DMA storage modulus for panel 4501-NPC on all days.

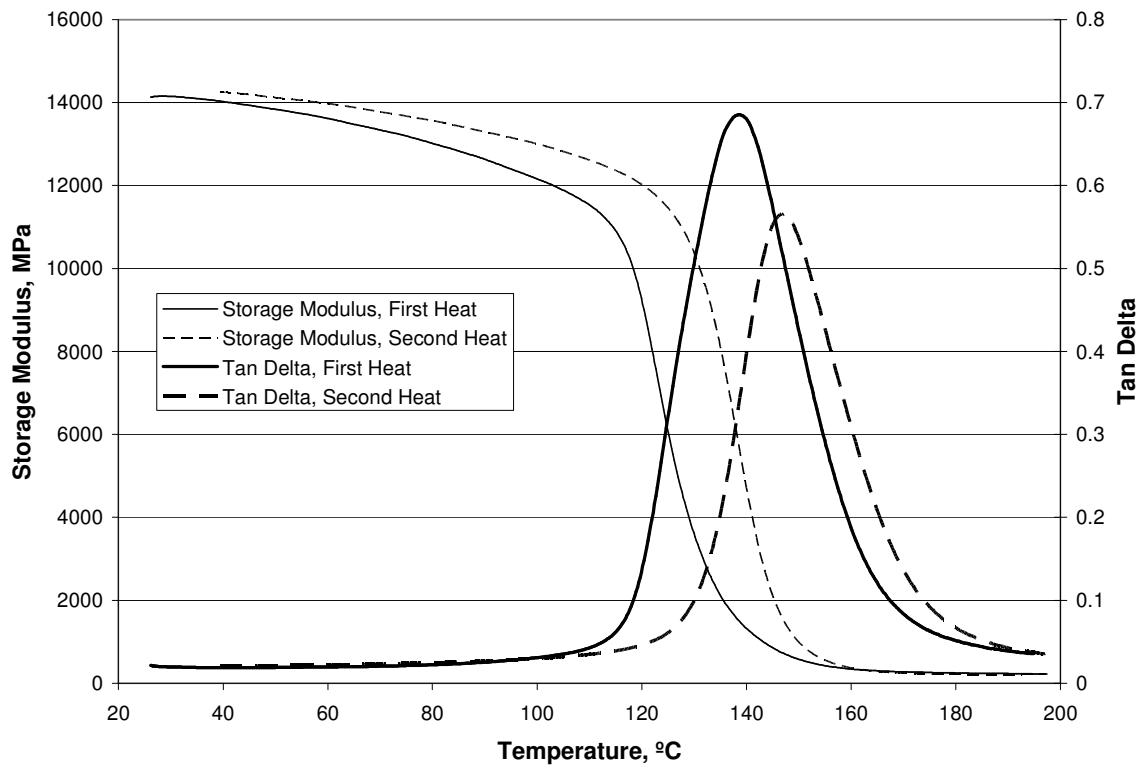


Figure 12: DMA storage modulus and tan delta curves for two replicates from panel 4504-93 on day 300.

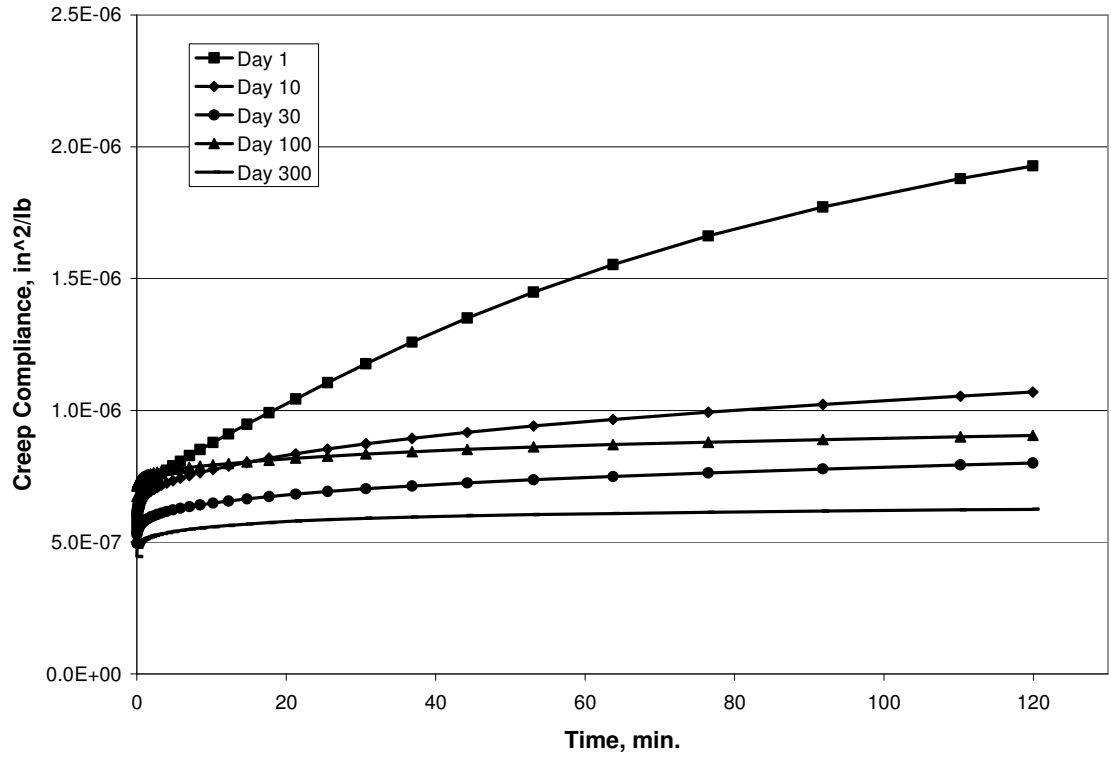


Figure 13: Creep compliance curves for panel 4501-NPC on all days.

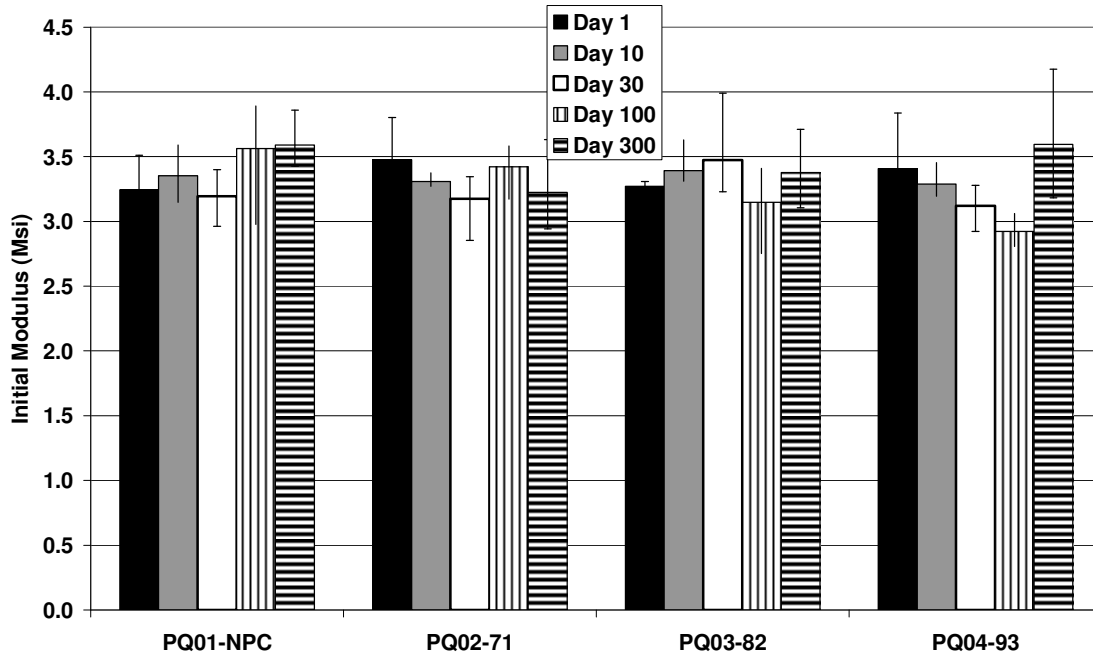


Figure 14: Mean initial modulus values of pseudo-quasi-isotropic specimens as a function of time and post-cure. Note that the error bars indicate the range of the data.

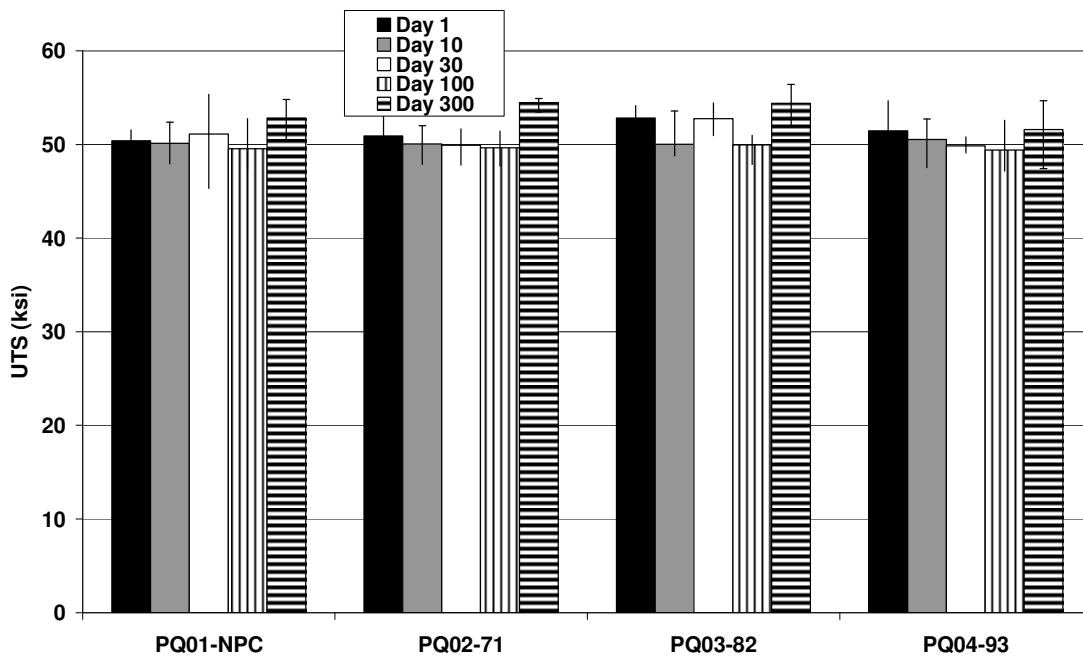


Figure 15: Mean ultimate tensile strength of pseudo-quasi-isotropic specimens as a function of time and post-cure. Note that the error bars indicate the range of the data.

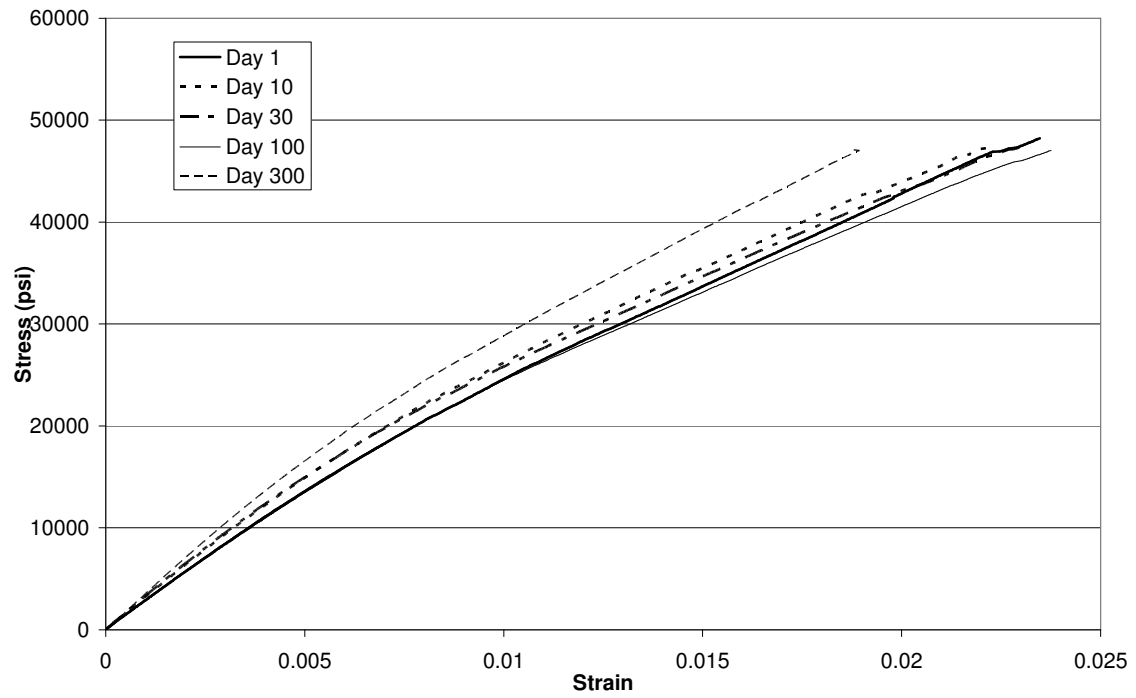


Figure 16: Stress-strain diagrams of panel PQ04-93 during quasi-static tension tests on all days.

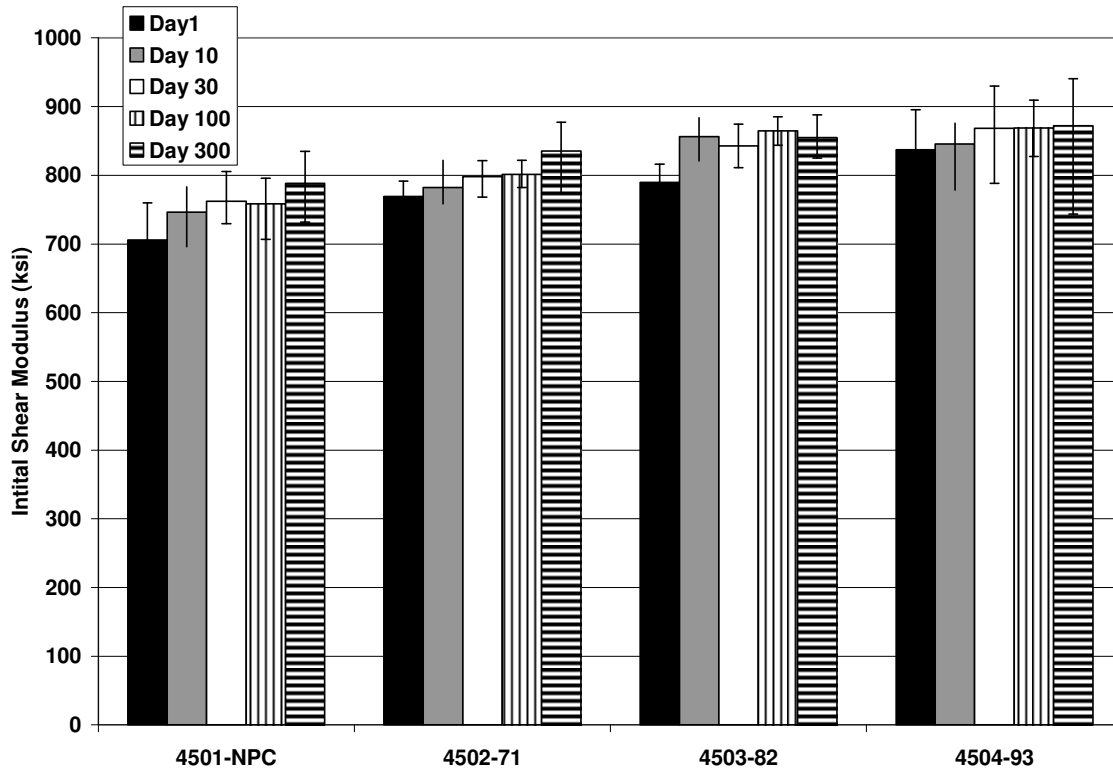


Figure 17: Mean initial shear modulus of $[\pm 45]_{2s}$ samples as a function of post-cure and time.

Note that the error bars indicate the range of the data.

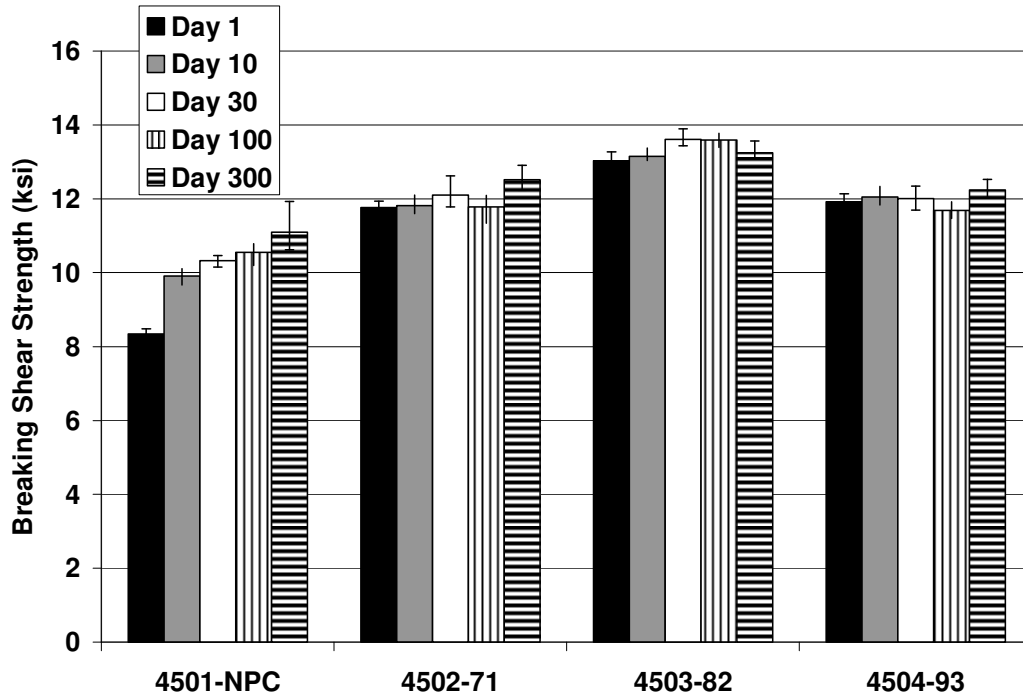


Figure 18: Shear strength for $[\pm 45]_{2s}$ panels as a function of post-cure and time. Note that the error bars indicate the range of the data.

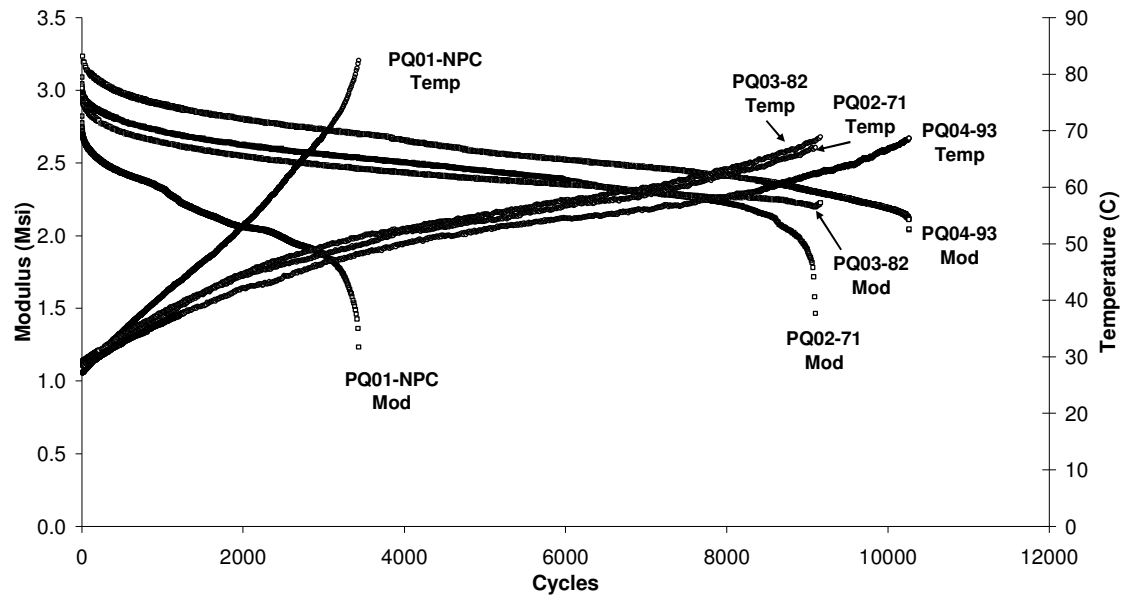


Figure 19: Typical stiffness reduction and temperature data for all panels on fatigue testing day

1.

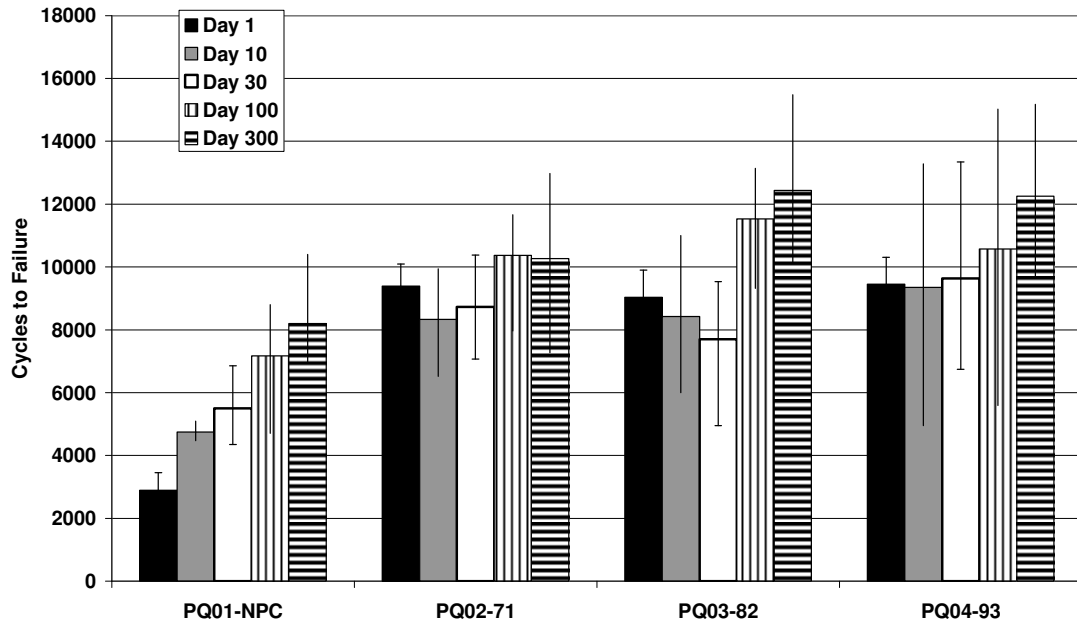


Figure 20: Cycles to failure data for all panels on all testing days. Note that the error bars indicate the range of the data.

4. The Effect of Mean Stress and the R-ratio on the Fatigue Performance of E-glass/Vinyl-ester Composites for Naval Applications

4.1. Introduction

In recent years the use of fiber reinforced polymer (FRP) composites in engineering applications has been growing, including in structural applications such as civil and naval engineering. Quite often these materials are subjected to static and cyclic loading conditions (either mechanical, hygrothermal, UV-related, etc.) of varying nature and severity. For the purposes of design, it is necessary to know how the resistance of the material to failure changes as a function of these applied loads. Furthermore, a full statistical description of the material behavior is desirable if one wishes to be able to assign probability values to material failure at a given point in the service life.

Therefore, in order to implement this approach, the statistical attributes of the material properties, such as material initial strength and residual strength after a given loading history, on which the model depends must be known, and this knowledge requires fairly extensive testing for characterization of the material. Towards this end the Materials Response Group is engaged in on-going work with a goal of developing a material database and a suitable and robust life-prediction methodology, which together will enable a more complete and accurate approach to reliability-based design and life prediction of composite materials, in particular those composite materials of interest to designers of naval vessels..

The portion of this program detailed in this chapter is focused on investigating the effect on fatigue durability of the R-ratio. The impact of R-ratio on composite materials has previously been investigated by several researchers, particularly Mandell et al. [84], who have conducted extensive testing to establish “complete” Goodman diagrams for fiberglass/polyester composites involving tensile-tensile, tensile-compressive, and compressive-compressive loading for use in the wind turbine industry. Mandell et al. then use these Goodman diagrams to predict failure in coupons tested using load spectra that are commonly used in the wind turbine industry and which are primarily tensile in nature. The purpose of the data collected by Mandell et al. is to allow the

prediction of fatigue lives of these materials given a spectrum representative of real world loads for wind turbine blades.

Similarly, this chapter will focus on constant- and variable amplitude fatigue loading of nearly-quasi-isotropic, E-glass/vinyl-ester laminates commonly used in naval applications for the purposes of life prediction for spectrum loads. A composite life prediction model that was developed by Case and Reifsnider [85] will be used to fit residual strength data. Based on the results of that data fitting, conclusions will be drawn concerning the applicability of the model to this type of testing, including possible limitations. In particular, two aspects of the modeling are of great interest. First, this chapter will address the question of whether the residual strength model is able to accurately fit constant-amplitude fatigue data, both in terms of the predicted median strength values, but also in terms of the statistical distributions of residual strength for various loading conditions. This prediction of stochastic lifetimes and strengths is important in the context of LRFD-type design applications that are of interest to the US Navy and which are being investigated by the Materials Response Group at Virginia Tech. Two related, but substantially different materials will be characterized in this way. The first material uses Ashland Derakane 510-A resin, a brominated vinyl ester resin that is designed to have fire-retarding properties, and E-glass fabric reinforcement. The second material to be discussed uses a matrix of Ashland Derakane 8084, a toughened vinyl-ester resin, and E-glass reinforcement. In both cases SN plots will be developed, and two model fit parameters (A and B , the slope and intercept of the power-law SN fit, respectively) will be found. Then the Case/Reifsnider residual strength model will be fit to the residual strength data in order to find the third and final fit parameter, j , required for the model.

The second question to be investigated by this chapter is whether, using the Case/Reifsnider model, it is possible to characterize a composite material, as above, in constant amplitude fatigue, and then use the knowledge gained from that characterization to make useful predictions concerning the expected performance of the material under variable-amplitude fatigue loading. Such an approach would be of great use to investigators looking at new materials, as it would require only that the material be characterized using relatively simple and straightforward constant-amplitude tests, rather than the more complicated variable-amplitude testing. This portion of the investigation will be performed using the E-glass/8084 vinyl-ester material alone.

The variable-amplitude fatigue condition investigated involves the application of a 5,000-cycle spectrum with an auto-correlation of 0.95 between adjacent extrema. This spectrum was developed by the US Navy for this project in response to Post's [22, 32] findings that purely random spectra were far more damaging to E-glass/vinyl-ester composites than an ordered (ascending or descending) spectrum with the same load levels, suggesting that cycle order effects seemed to be an important consideration for life prediction of these materials. However, purely random spectra are not realistic loading conditions for sea-going vessels that the Navy is concerned with. Furthermore, the life-prediction model currently used by the Materials Response Group was unable to account for the cycle order dependence of the fatigue life described above. The highly correlated spectra developed was seen as a way to begin to come to terms with the implications of variable-amplitude loading, while also providing the Navy with data that were more directly related to the service conditions that naval vessels could be expected to see.

For both materials and for all tests, the R-ratio was seen to have significant qualitative and quantitative effects on fatigue performance, since the materials exhibit different fatigue sensitivities to different damage modes. Furthermore, differences in the goodness of fit of the model to the residual strength data, both in terms of the median values and the statistical distributions of strengths, were seen depending on the matrix material and the loading ratio. Overall, the model was seen to have some difficulties in accurately modeling the distributions of residual strength for certain loading conditions, while modeling them quite well for others. Furthermore, the value of the model fitting parameter, j , derived from the fitting of the constant-amplitude residual strength data was found to be useful in the calculation of lifetime prediction for variable-amplitude loading for the investigated R-ratios of $R=-1$, $R=0.1$, and $R=10$. In all cases, the residual strength model provided good prediction of the variable-amplitude performance and suggests that it is a useful tool for allowing the prediction of variable-amplitude fatigue lives based on knowledge of the constant-amplitude material characterization.

4.2. Material description

Two composite materials were examined in this work. The first material was manufactured by the Northrup-Grumman Corporation using the vacuum-assisted resin transfer molding (VARTM) technique, and using Vetrotex 324 woven roving E-glass and Derakane 510-A resin. The lay-up was $[0/45/90/-45/0]_s$, where the directions refer to the orientation of the warp direction of the weave. Five 0.9 m x 0.9 m subpanels were cut from an original 5.2 m x 1.1 m panel. Testing samples were then cut from these five subpanels. This material was used in the constant-amplitude fatigue portion of this work, but not for the variable-amplitude portion.

The second material was manufactured in-house by the Materials Response Group using Derakane 8084 resin instead of the 510-A. All other material parameters were nominally identical. This material was characterized for both constant-amplitude and variable-amplitude fatigue.

For each material, straight-sided, un-tabbed samples were cut to a nominal size of 15.2 cm x 2.54 cm (long dimension in the 0° direction) using a water-cooled diamond saw, and the long edges were then surface ground to ensure consistent widths, and parallel edges free of large-scale defects.

Previous investigation [13] into the stability of material properties for composite materials suggests that E-glass/vinyl-ester composites may evolve with time if the material is not post-cured after manufacture. Therefore, for this study, the samples from each material set were post-cured at 82°C for 4 hours and slow-cooled before testing began.

4.3. Details of the Case and Reifsnider residual strength model and its application to fatigue data

The constant-amplitude fatigue data presented in this chapter were fit using a model originally developed by Reifsnider et al. [86] in which it is assumed that the initial strength of the material is a stochastic variable, specifically belonging to a Weibull [44] distribution, in which the probability of failure is given by

$$P_f = 1 - \exp\left[-\frac{\sigma_{init}}{\beta}\right]^\alpha \quad (19)$$

where α and β are the Weibull shape and location parameters, respectively. Rearranging, we see that the initial ultimate strength is given by

$$\sigma_{init} = \ln\left[\frac{1}{1-P_f}\right]^{\frac{1}{\alpha}} \beta. \quad (20)$$

Reifsnider and Case have shown that the remaining strength of composite materials subjected to cyclic load can be modeled by the following equation

$$Fr(n) = 1 - \left\{ \int_0^n (1 - Fa(n))^{1/j} \frac{dn}{N(Fa)} \right\}^j, \quad (21)$$

where Fr is the remaining strength normalized by the ultimate initial strength; Fa is the applied stress normalized by the ultimate initial strength; n is cycles; N is the number of predicted cycles to failure for a constant amplitude loading of Fa , and j is a fitting parameter that influences the shape of the residual strength curve.

Failure is considered to occur when the applied stress is equal to or greater than the residual strength. That is, the material fails when

$$Fr(n) \leq Fa(n), \quad (22)$$

where

$$Fr = \frac{\sigma_{residual}}{\sigma_{init}} \quad (23)$$

and

$$Fa = \frac{\sigma_{applied}}{\sigma_{init}}. \quad (24)$$

For constant amplitude loading, Equation 21 simplifies to

$$Fr(n) = 1 - (1 - Fa(n)) \left(\frac{n}{N(Fa)} \right)^j. \quad (25)$$

In Equation 25, $N(Fa)$ is determined from the SN curve developed from the constant-amplitude fatigue-to-failure data by fitting the data to the form

$$\log(N) = A \log\left(\frac{\sigma_a}{\sigma_{ult}}\right) + B \quad (26)$$

A and B are two of the three fitting parameters required for the use of the residual strength model. Once A and B have been found using the fatigue-to-failure data, the third fitting parameter, j , is fit using the residual strength data. For each R-ratio, all residual strength data points are fit to the form of Equation 25, and j is iteratively solved for using a spreadsheet in such a way as to minimize the sum of the squared differences between the modeled residual strength and the residual strength data.

Since, in Equation 25, Fr , Fa , and N are all functions of the stochastic, Weibull-distributed initial strength, the predicted remaining strength is represented by a Weibull probability distribution, as well. The cumulative distribution function of the remaining strength for a given R-ratio and applied stress level can be calculated as given in Figure 21. Here, a distribution of values for probability of failure is created (first column in Figure 21). From these values, the corresponding distribution of initial strengths can be generated (second column). Knowing these initial strengths, and the applied load, a distribution of normalized applied load, Fa , is generated (third column), and finally the expected lifetime for a given load and initial strength is calculated (fourth column) from the use of the SN curve. (This last step will be modified for certain cases, as described in 4.5.1) Once these values are known, they are used in Equation 25 to predict the residual strength for those conditions at a given number of cycles (columns 5-10).

More detailed information concerning the statistical distribution of the predicted residual strength can be determined from a Weibull analysis. To calculate the values of the scale and location Weibull parameters for the residual strength distribution, a plot is made of $\ln(\ln(1/(1-P_f)))$ versus $\ln(\text{residual strength})$, as seen in Figure 22. The slope and intercept of the resulting line are easily found, and if the slope is m and the intercept b , then the Weibull parameters can be calculated as

$$\alpha = m \quad (27)$$

and

$$\beta = e^{-b/m} \quad (28)$$

These parameters are valuable measurements of the model's ability to fit the data, since they describe not only the fit of the prediction through the data, but the prediction of the distribution of the data.

4.4. Testing plan for constant- and variable-amplitude fatigue of E-glass/510-A and E-glass/8084 composites

4.4.1. Constant-amplitude fatigue testing

For each material, S-N curves were generated for three R-ratios, specifically R=0.1, R=-1, and R=10. Table 2 lists the details of the fatigue-to-failure testing for each material. As Table 2 shows, for each R-ratio, several stress levels were chosen in such a way as to provide data over a range of lifetimes from approximately 10^3 to 10^6 cycles. It should be noted that the applied stresses listed in Table 2 for R=-1 refer to the amplitude of the loading curve, not the stress range.

The fatigue-to-failure data for each R-ratio were fit to log-log stress-life relationships (SN curves). The two constants in the equation (*A* and *B*) comprise two of the three curve fitting parameters used for fitting the residual strength model.

Constant-amplitude residual strength tests were also performed on each material. As Table 3 shows, residual strength tests were performed at various stress levels and percentages of the nominal lifetimes at those stress levels. The distribution of residual strength as a function of cycles allowed for the fitting of the third model fitting parameter needed, *j*.

All tests were conducted using an 89-kN servo-hydraulic load frame. Fatigue and residual strength tests were run at a frequency of 10 Hz for the 510-A material, and at 5 Hz for the 8084 material. While this difference in frequency might be suspected of biasing the results, Post (to be published, 2008/2009) has seen that the fatigue behavior for these materials does not change significantly over a range of frequencies from 5 Hz to 20 Hz.. Quasi-static loads were applied at a rate of 667 N/sec. The average widths and thicknesses for each sample were measured and recorded for use in calculating the applied stress.

4.4.2. Variable-amplitude fatigue testing

As mentioned in section 4.1, the variable-amplitude testing was performed using only the E-glass/8084 material, and at the 5 Hz frequency used for that material in the constant-amplitude testing.

The testing consisted of the repeated application of a 5,000-cycle spectrum of variable-amplitude. The spectrum was generated by engineers at the US Naval Surface Warfare Center for the purposes of investigating the effect of variable-amplitude loading on naval composites under conditions approximating real world operating conditions. To that end, the spectrum was created to have an autocorrelation between successive extrema of approximately 0.95. This condition creates a spectrum in which the extrema are not completely random, and which is more consistent with the nature of ocean waves, in which wave size varies randomly, but the amplitudes of successive waves are generally not vastly different from one another. Figure 37 shows the first few seconds of the time history of the spectrum.

This spectrum was provided in a form in which the RMS value was 1.0. Therefore, various applied stress levels were achieved by scaling the given spectrum by the stress scale factors shown in Table 4 for the same three R-ratios investigated for the constant-amplitude testing.

It should be noted that the spectrum used for the R=-1 loading case was qualitatively different than those used for the R=10 and R=0.1 load cases due to the way the latter two spectra were derived from the former. As mentioned above, the R=-1 spectrum was created to have an autocorrelation of approximately 0.95 with respect to successive extrema. This means that the spectrum is nominally R=-1, but nowhere in the spectrum (unless by chance) are there examples of a valley with magnitude equal (but of opposite sign) to the previous peak, and therefore, no cycles within the spectrum are truly fully reversed.

To generate the R=0.1 spectrum, however, the valleys of the R=-1 loading spectrum were dropped, and replaced with valleys with amplitudes equal to 1/10th of the previous peak. In this way, each cycle within the R=0.1 spectrum does actually correspond exactly to an R-ratio of 0.1. However, in this case successive extrema no longer have an autocorrelation of 0.95.

The R=10 spectrum was derived from the R=0.1 spectrum by “flipping” it around the time axis of the time history plot into the compressive regime of negative loads. That is to say that the R=10 valleys were set equal to the corresponding R=0.1 peaks multiplied by -1, and the R=10 peaks were set equal to the corresponding R=0.1 valleys multiplied by -1.

4.5. Constant-amplitude experimental results

4.5.1. Data and analysis for the E-glass/510-A constant-amplitude testing

Figure 23 shows the S-N curves generated for the three R-ratios examined for the 510-A material. It is clear that there are qualitative differences in the fatigue behavior for each loading ratio. While the R=0.1 data are fit rather well by a single power-law curve, the R=10 and R=-1 data each exhibit a “knee” where a transition in the fatigue sensitivity occurs. This transition is largest and especially abrupt for the case of R=-1, where at an applied stress of approximately 30% of the UCS, and a projected lifetime of approximately 10,000 cycles, the material behavior changes drastically. At higher applied stresses (and shorter lifetimes), the material shows a relatively high fatigue resistance, which is to say that for relatively small changes in applied stress the predicted lifetimes change by a small amount. At lower applied stresses, however, the material is very sensitive to fatigue, i.e. for small changes in applied stress the lifetimes vary drastically because of the shallow slope of the S-N curve in this region. As a result, the scatter in the data in this region is much larger than is seen in portions of the curve with larger slope due to the broadening of the distribution of fatigue lives with decreasing stress and increasing fatigue lives.

Table 5 gives the curve fit parameters for the various power law S-N curves fit through the data of the form of Equation 29.

$$\log(N) = A \log(Fa) + B \quad (29)$$

where

$$Fa = \frac{\sigma_a}{\sigma_{ult}} \quad (30)$$

For this material the ultimate tensile strength was found to have a median value of 333.0 MPa, and the ultimate compressive strength was 298.5 MPa. It should be noted that since the failure mechanism for R=0.1 is tension failure, and the failure mode for R=-1 and R=10 appears to be compressive failure, results from the former case were normalized by the ultimate tensile strength (UTS), and results from the latter two were normalized by the ultimate compressive strength (UCS).

Example data from residual strength tests at R=0.1 are shown in Figure 24. Here, the residual strength data are plotted as a function of the percentage of the predicted lifetime to which they were cycled. In each case there is a clear and fairly linear decrease in the residual strength as a function of cycles. When the residual strength model was fit to these data, the fit parameter j was found to have the value $j=1.16$. The near-linear behavior of the residual strength curve is explained by the small deviation of j from a value of unity. The data and the resultant residual strength fits for R=0.1 are shown in Figure 25 on a semi-log scale.

A Weibull analysis, as described in 4.3 and shown in Figure 22 was performed on the residual strength data points, and the relevant results are summarized in Table 6.

The residual strength data were fit to a Weibull distribution; the cumulative distribution functions (CDF) for the various cases are given in Figure 26. It is clear that the predictions from the residual strength model (solid lines) are fairly successful at representing the Weibull distribution of the experimental residual strength data for an R-ratio of R=0.1, especially at longer lifetimes. The fit is less good, but still reasonable, at shorter lifetimes.

For a loading ratio of R=-1, however, the residual strength curves show much less strength degradation over the majority of the lifetimes. For instance, Figure 27a shows the residual strength curves for an R-ratio of R=-1, and a loading level of 29.9% UCS. Over the first 60% of the predicted lifetime the residual strength does not change significantly; after about 60%, however, the strength drops more quickly. This “sudden death” behavior, where most strength degradation is seen in the latter stages of the test, is indicative of a j value greater than unity. A similar result was seen for the much longer tests run at 28.8% UCS.

When the residual strength model was fit to the data, a value of $j=1.64$ was found. This value provided adequate fitting of the residual strength model to the data, as seen in Figure 28.

The Weibull analysis results for the experimental residual strength distribution for $R=-1$ are given below, in Table 7.

Despite the reasonable fit of the residual strength model to the data, when the residual strength cumulative distribution functions (CDFs) were plotted, it was clear that the model was not giving good predictions of the shape of the residual strength Weibull distribution. Figure 29 shows the residual strength CDF for one loading level at $R=-1$. Clearly, the model is not capturing the correct distribution of residual strength.

In order to correct this problem, it was necessary to make a modification to the process used for calculating the CDF values. As described in section 4.3 and shown in Figure 21, the value of N is calculated as a function of P_f . However, this introduces numerical difficulties into the model calculation under certain circumstances. The excessively flat slope of the low stress end of the $R=-1$ SN curve causes the term N (the predicted lifetime for a given initial strength) in the residual strength calculation to span an inordinately large range over the $0 \rightarrow 1$ range of P_f . As a result, the term n/N in the residual strength prediction calculation tends toward zero for the high end of the initial strength distribution, and thus drives the residual strength prediction towards being equal to the initial strength, as seen in the convergence of all residual strength distributions in Figure 29 toward the right hand side.

Several attempts were made to modify the calculation method described in section 4.3 and shown in Figure 21. In the end, for $R=-1$ and $R=10$, described below, and for the E-glass/510-A material, the following modification was found to be somewhat useful in modeling the data. The value of N calculated in Figure 21 was no longer calculated from the SN curve, but was instead calculated from an alternative method that removed the stretching of the Weibull distribution of residual strength and greatly reduced the numerical difficulties involved in calculating the Weibull CDFs. Figure 30 shows the resulting residual strength CDF plots. It is clear that the stretching of the distribution has been lost, and furthermore, the location of the distribution is shifted unrealistically. However, this is still an improvement on the original method.

Like the residual strength behavior at $R=-1$, for $R=10$, also, the behavior is indicative of a relatively large value for j . Figure 27b shows the residual strength curve for $R=10$ and a loading

level of 58.7% UCS. Again, the failure is of the “sudden death” type, so much so that the data seems to describe a straight, horizontal line. Note that the outlying data points plotted at a strength of approximately 175.1 MPa represent premature failure tests, in which the sample failed before reaching the prescribed lifetime percentage, and which were plotted at the applied load level.

When the residual strength model was fit to the data, a value of $j=0.464$ was found. This value provided adequate, but not extremely good, fitting of the residual strength model to the data, as seen in Figure 31. In this case, a larger value of j was expected due to the sudden death failures. And indeed, even though the value of j was found using a least-squares fitting method and, thus, represents the “best” fit through the data, a larger value of j would undoubtedly have provided a better-looking fit. It is likely that the lower-than-expected value of j is an artifact of the large number of premature failures that were encountered during the testing, as well as the general difficulty in fitting data with such a pronounced and rapid change in slope in such a short span.

The Weibull analysis results for the experimental residual strength distribution for $R=-1$ are given below, in Table 8.

Similar results were seen for the model-predicted residual strength CDFs as with the $R=-1$ case. Figure 32 shows a typical example.

4.5.2. Data and analysis for the E-glass/8084 constant-amplitude testing

Stress-life plots for the E-glass/8084 material are qualitatively reminiscent of those for the E-glass/510-A material, as seen in Figure 33. One significant difference, however, is the reduced severity of the “knees” at approximately 10,000 cycles for $R=-1$ and $R=10$. In fact, the $R=10$ data can be fit very satisfactorily with a single power-law curve. The $R=-1$ data, however, still seems to possess a bilinear nature, and so has two sets of fitting parameters given in Table 9.

It is also apparent from Figure 33 that the fairly shallow area of the $R=-1$ curve (above ~10,000 cycles) is significantly steeper than the corresponding portion of the curve for the 510-A matrix material. As discussed in the previous section, the excessive flatness of the latter curve led to numerical difficulties when calculating residual strength predictions. We will see that since the

8084 material does not suffer from quite such a flat curve, that the residual strength predictions will be somewhat more accurate as a result.

Residual strength data for R=0.1 is shown in Figure 34. For this fit a value of $j=0.784$ was found, and the fit seems to be a very good one, as both the trends and the median values of the experimental data seem well represented by the model.

Figure 35 and Figure 36 show the residual strength data for R=-1 and R=10 with fit parameters of $j=1.21$ and $j=0.791$, respectively. In general, the fits are very good, though again, as with the 510-A material, the R=10 case presents some problems for the model, and the fit is not quite as good as for the other loading ratios.

The E-glass/8084 material showed the same trends as the E-glass/510-A material in terms of the sudden death nature of the failures at R=10 and R=-1, especially the former. However, like the shallow slopes of the SN curves, this phenomenon seemed less pronounced in this material than the E-glass/510-A material. As a result of this and the relatively smaller number of premature failures, the residual strength distributions predicted by the model for this material were somewhat better than for the 510-A material. Though they were far from perfect, it was decided that it was not necessary to alter the method of calculating N for the distribution calculation as it was for the data of the previous section.

Weibull analyses on the residual strength experimental data for R=0.1, R=-1, and R=10 are given in Table 10, Table 11, and Table 12, respectively.

4.6. Variable-amplitude experimental results

As discussed in Section 4.1, the purpose of the constant-amplitude testing described above is to provide material characterization information that can be used by the Reifsnider/Case residual strength model to predict variable-amplitude fatigue lives.

Equation 31 represents the discrete version of the residual strength model of Equation 21.

$$Fr = 1 - \left[\sum_{n=1}^M (1 - Fa(n))^{1/j} \frac{1}{N(Fa)} \right]^j \quad (31)$$

If we make a substitution for the terms inside the large brackets and take $M=5000$ (the number of cycles in the spectrum), then we can see that the residual strength of the material at the end of the K th repeat of the spectrum is given by

$$Fr = 1 - \Delta^j K \quad (32)$$

where the value of Δ is calculated using discrete values of Fa (and subsequently N) calculated from the peak load of each cycle in the spectrum.

Furthermore, if we set $Fr=Fa_{\max}$, where we have assumed that the material fails on the highest peak in the spectrum, then we can arrive at the following expression for the number of spectrum repeats that can be expected for a given material and loading:

$$K = \frac{1 - Fa_{\max}}{\Delta^j} \quad (33)$$

Multiplying K by 5,000 to arrive at an approximation of the expected life, and plotting this value against applied RMS stress, an SN curve for variable amplitude fatigue can be plotted. Figure 38 shows these plots for all three R-ratios. While the fits are not perfect, they are quite good; the fits for $R=0.1$ and $R=-1$ are particularly good. This is encouraging since $R=-1$ is the loading ratio of most interest for many naval applications. The fit for $R=10$ is not as good as for $R=-1$, but is still very close, and furthermore, is always conservative, at least over the lifetimes examined. In all cases the predicted slopes are very close to those of the experimental data.

4.7. Conclusions

Fatigue and residual strength tests have shown that for E-glass/vinyl ester composites the effect on lifetimes and strength degradation of the R-ratio during cyclic loading may be dramatic. Fatigue life (S-N) curves were generated for three different R-ratios: $R=0.1$, $R=10$, and $R=-1$. For tension-tension tests ($R=0.1$), the observed failure mechanism was tensile failure, while for compression-compression ($R=10$) and fully-reversed ($R=-1$) loading the observed failure mechanism was compressive. The three S-N curves show not only quantitative differences in lifetime, but also qualitative differences in shape. The curve generated for $R=10$ shows a moderate “knee” at roughly 20,000 cycles, with the slope becoming somewhat flatter at higher

lifetimes. The $R=-1$ curve shows a much more pronounced “knee” at approximately 8,000 cycles; the slope of the curve becomes very flat at higher cycles, leading to a much greater fatigue resistance and data scatter.

Residual strength tests also show a qualitative difference in behavior among the three R -ratios analyzed. For $R=0.1$, the residual strength was seen to decrease significantly during most of the life of the specimen in a roughly linear fashion, with the residual strength model fitting parameter, j , having a value near unity (1.16). For fully-reversed loading, the residual strength did not change significantly over most of the life of the test, but then declined fairly rapidly after approximately 60-70% of the test. Loading at $R=10$ also produced residual strength curves in which no visible strength degradation occurred over most of the specimen lifetime. In fact, the strength was seen to be roughly constant over the range of lifetime percentages tested (75%), suggesting the final reduction in strength occurred rapidly near the end.

In the past, the Case/Reifsnider residual strength model has been shown to provide a reasonable fit to data from constant-amplitude $R=0.1$ loading, in which the failure mode is tensile. More recent testing at $R=-1$ and $R=10$ have shown that the model is limited in its ability to model the residual strength statistical distribution for these loading ratios. The ratio of n/N in the model was shown to be a source of error for S-N curves of almost zero slope, since under these conditions in the stochastic model a relatively small range of possible initial material strengths results in this ratio approaching zero, thus eliminating the strength-degradation term from the equation. However, the model does provide a good fit to the residual strength mean value curves.

More importantly, the model has been shown to be very good at predicting the fatigue lives for variable-amplitude loading cases in which the applied spectrum has a fairly large autocorrelation value. Such a spectrum was applied in fully-reversed loading ($R=-1$), and a similar spectrum derived from the first was applied in compressive-compressive ($R=10$) loading, and in each case the predicted variable-amplitude lives agreed fairly well with the experimental data, especially for $R=-1$. Because real-world loads for naval vessels (and for many other applications) involve variable-amplitude loading, and since constant-amplitude loading is much more readily available in the literature and more easily obtainable in the laboratory, the above results suggest that the Case/Reifsnider model may be a very useful tool for designers of composite structures.

The ability of the Case/Reifsnider model to so accurately model the variable-amplitude data using material characterization derived from constant-amplitude testing is a strong validation of its usefulness for designers of naval vessels.

4.8. Figures and Tables

Table 2: Constant-amplitude fatigue to failure testing for E-glass/510A and E-glass/8084

	E-glass/510-A		E-glass/8084	
	% Ult. strength*	# replicates	% Ult. strength*	# replicates
R=0.1	32.0	6	23.9	10
	36.0	18	32.9	10
	40.0	17	43.7	10
	44.0	17	50.7	10
	52.0	18	55.7	10
	72.0	16		
R=-1	27.7	12	19.9	10
	28.8	10	24.9	10
	29.9	10	27.8	10
	54.3	12	29.8	10
			41.2	10
R=10	49.8	12	47.2	10
	54.3	10	50.7	10
	58.7	10	55.3	10
	66.5	12	57.6	10
			64.5	10

* Ultimate strength is considered to be the ultimate tensile strength (UTS) for R=0.1, and ultimate compressive strength (UCS) for R=-1 and R=10.

Table 3: Test plan for constant-amplitude residual strength testing.

E-glass/510A								
R=0.1			R=-1			R=10		
% UTS	% Life	Repl.	% UCS	% Life	Repl.	% UCS	% Life	Repl.
52.0	10	15	29.9	35	10	58.7	35	10
	30	10		50	10		43	10
	50	15		60	10		50	10
	60	10		75	10		60	10
	70	15		85	10		75	10
44.0	10	15	28.8	35	10	49.8	20	15
	30	10		50	10		35	15
	50	15		60	10		50	15
	60	10		75	10		60	15
	70	15		85	10			
E-glass/8084								
R=0.1			R=-1			R=10		
% UTS	% Life	Repl.	% UCS	% Life	Repl.	% UCS	% Life	Repl.
43.7	10	10	31.9	10	10	54.7	10	10
	30	10		30	10		30	10
	50	10		50	10		50	10
	70	10		70	10		70	10
32.9	10	10	28.5	10	10	50.1	10	10
	70	10		70	10		70	10
23.8	10	10	22.8	10	10	46.7	10	10
	30	10		30	10		30	10
	50	10		50	10		50	10
	70	10		70	10		70	10

Table 4: Test plan for variable-amplitude fatigue to failure testing with Rayleigh-distributed spectrum.

R=-1				
Desired cycles	# of spectrum repeats	Scale factor (MPa)	Maximum <i>Fa</i> (based on median initial strength)	# of repl.
25,000	5	42.14	0.546	15
200,000	40	32.76	0.424	10
1,000,000	200	27.78	0.360	10
R=10				
Desired cycles	# of spectrum repeats	Scale factor (MPa)	Maximum <i>Fa</i> (based on median initial strength)	# of repl.
30,000	6	64.2	0.846	10
50,000	8	60.0	0.791	10
200,000	40	56.4	0.744	10
R=0.1				
Desired cycles	# of spectrum repeats	Scale factor (MPa)	Maximum <i>Fa</i> (based on median initial strength)	# of repl.
20,000	4	59.9	0.669	10
50,000	10	50.0	0.558	10
200,000	40	45.7	0.510	10

Table 5: Curve fit parameters for normalized E-glass/510-A S-N curves for three R-ratios.

R-ratio	<10,000 cycles		>10,000 cycles	
	A	B	A	B
0.1	-8.59	1.64	Same	Same
-1	-51.1	-22.5	-3.63	1.99
10	-6.62	2.42	-21.9	-1.09

Table 6: Results of Weibull analysis of E-glass/510-A constant amplitude residual strength tests at R=0.1.

Applied stress (MPa)	Cycles applied	# of premature failures	# of RS data points	Median (MPa)	α	β (MPa)
173.2	1000	0	15	310	22.3	315
173.2	3000	0	10	292	16.7	293
173.2	5000	0	15	280	24.1	284
173.2	6000	2	10	272	17.8	279
173.2	7000	1	15	264	19.8	266
146.5	5000	0	15	294	22.0	299
146.5	15,000	0	10	266	15.7	275
146.5	25,000	1	15	249	15.6	259
146.5	30,000	4	10	245	11.1	249
146.5	35,000	4	15	232	9.1	244
120.0	50,000	0	9	275	18.2	285
120.0	150,000	1	10	273	13.1	277
120.0	250,000	1	4	254	15.4	260

Table 7: Results of Weibull analysis of E-glass/510-A constant amplitude residual strength tests at R=-1.

Applied stress (MPa)	Cycles applied	# of premature failures	# of RS data points	Median (MPa)	α	β (MPa)
86.0	44700	0	10	277.9	15.1	267.2
86.0	63800	0	10	268.7	12.9	235.2
86.0	76600	0	10	253.5	11.2	210.1
86.0	95700	0	10	260.8	8.32	167.2
86.0	108500	2	8	256.5	8.04	134.8
89.3	4300	0	10	271.1	16.5	287.2
89.3	6200	0	10	278.9	15.3	270.6
89.3	7400	0	10	262.3	14.5	258.2
89.3	9300	0	10	249.8	12.9	235.9
89.3	10500	1	9	247.2	11.9	220.1

Table 8: Results of Weibull analysis of E-glass/510-A constant amplitude residual strength tests at R=10.

Applied stress (MPa)	Cycles applied	# of premature failures	# of RS data points	Median (MPa)	α	β (MPa)
148.9	63000	2	13	279.9	11.2	239.0
148.9	110300	6	9	247.1	12.0	217.8
148.9	157600	10	5	148.9	12.0	201.7
148.9	189000	10	5	148.9	12.6	192.5
175.4	4400	0	10	271.0	14.4	217.8
175.4	5400	5	5	211.9	15.2	209.4
175.4	6300	4	6	245.1	16.1	202.9
175.4	7560	5	5	208.3	17.9	195.1
175.4	9450	6	4	175.4	22.7	186.2

Table 9: SN curve fitting parameters for constant-amplitude fatigue testing of E-glass/8084 material.

R-ratio	<10,000 cycles		>10,000 cycles	
	A	B	A	B
0.1	-6.88	1.548	Same	Same
-1	-5.18	1.283	-11.15	-1.408
10	-14.40	0.500	Same	Same

Table 10: Weibull analysis for the residual strength of E-glass/8084 at constant-amplitude R=0.1 loading.

Applied stress (MPa)	Cycles applied	# of RS data points	# of pre-mature failures	Median (MPa)	α	β (MPa)
151.7	727	11	0	327.5	18	337.8
151.7	868	5	0	310.9	18.3	317.8
151.7	2180	11	0	309.5	14.6	317.1
151.7	3633	9	1	275.8	9.8	274.4
151.7	5086	10	0	254.4	7.7	273.0
114.4	7250	12	0	307.5	3.1	337.1
114.4	50751	5	5	206.8	1.9	168.2
82.7	90304	10	0	294.4	12.1	304.0
82.7	270911	9	1	242.0	3.8	247.5
82.7	451519	9	2	253.7	4.3	246.1
82.7	632127	4	3	200.6	3.9	193.7

Table 11: Weibull analysis for the residual strength of E-glass/8084 at constant-amplitude R=-1 loading.

Applied stress (MPa)	Cycles applied	# of RS data points	# of pre-mature failures	Median (MPa)	α	β (MPa)
-96.5	1298	10	0	311.6	11.8	324.0
-96.5	3894	11	0	288.2	16.5	294.4
-96.5	6491	4	5	265.4	4.9	246.8
-96.5	9087	7	3	245.4	5.7	255.8
-86.2	5481	10	0	286.8	17.7	292.3
-86.2	38364	7	4	260.6	12.3	254.4
-68.9	55635	10	0	287.5	7.7	293.7
-68.9	166904	10	0	283.3	9.5	291.6
-68.9	278174	9	1	264.0	5.8	269.6

Table 12: Weibull analysis for the residual strength of E-glass/8084 at constant-amplitude R=10 loading.

Extreme stress applied (MPa)	Cycles applied	# of RS data points	# of pre-mature failures	Median (MPa)	α	β (MPa)
-165.5	1620	10	0	326.8	22.3	331.6
-165.5	4860	9	1	297.8	9	294.4
-165.5	8100	5	5	280.6	8.5	272.3
-165.5	11339	0	6	N/A	N/A	N/A
-151.7	10313	11	0	301.3	13.5	302.6
-151.7	72184	0	6	N/A	N/A	N/A
-141.3	22551	10	0	293.0	16	302.6
-141.3	67652	5	5	271.6	3.7	258.5
-141.3	112753	8	2	259.9	7.8	265.4
-141.3	157854	1	7	234.4	N/A	N/A

Prob. of failure distribution	Calculated as function of Pf.			Cycles of fatigue before RS measurement					
	Strength	Fa	N	0	4300	6200	7400	9300	10500
0.01	34477	0.376	3427	34477	12960	12960	12960	12960	12960
0.05	37770	0.343	4770	37770	16837	12960	12960	12960	12960
0.1	39322	0.330	5520	39322	21812	12960	12960	12960	12960
0.15	40287	0.322	6028	40287	24571	12960	12960	12960	12960
0.2	41008	0.316	6428	41008	26491	14572	12960	12960	12960
0.25	41595	0.312	6768	41595	27974	16790	12960	12960	12960
0.3	42098	0.308	7070	42098	29193	18598	12960	12960	12960
0.35	42545	0.305	7346	42545	30239	20136	12960	12960	12960
0.4	42953	0.302	12022	42953	37386	32815	29407	23256	18925
0.45	43333	0.299	18857	43333	40636	38422	36771	33791	31693
0.5	43693	0.297	28796	43693	42329	41209	40374	38867	37806
0.55	44040	0.294	43173	44040	43330	42746	42311	41526	40973
0.6	44381	0.292	64006	44381	44004	43694	43463	43047	42754
0.65	44720	0.290	94474	44720	44518	44353	44230	44007	43851
0.7	45064	0.288	139830	45064	44957	44869	44803	44685	44602
0.75	45421	0.285	209345	45421	45365	45319	45285	45223	45180
0.8	45802	0.283	320900	45802	45774	45751	45733	45702	45680
0.85	46225	0.280	513772	46225	46212	46201	46193	46178	46168
0.9	46729	0.277	894373	46729	46723	46719	46716	46710	46706
0.95	47422	0.273	1899333	47422	47420	47419	47418	47416	47415
0.99	48577	0.267	6501986	48577	48576	48576	48576	48576	48576

Figure 21: Calculation of predicated residual strength Weibull CDF values.

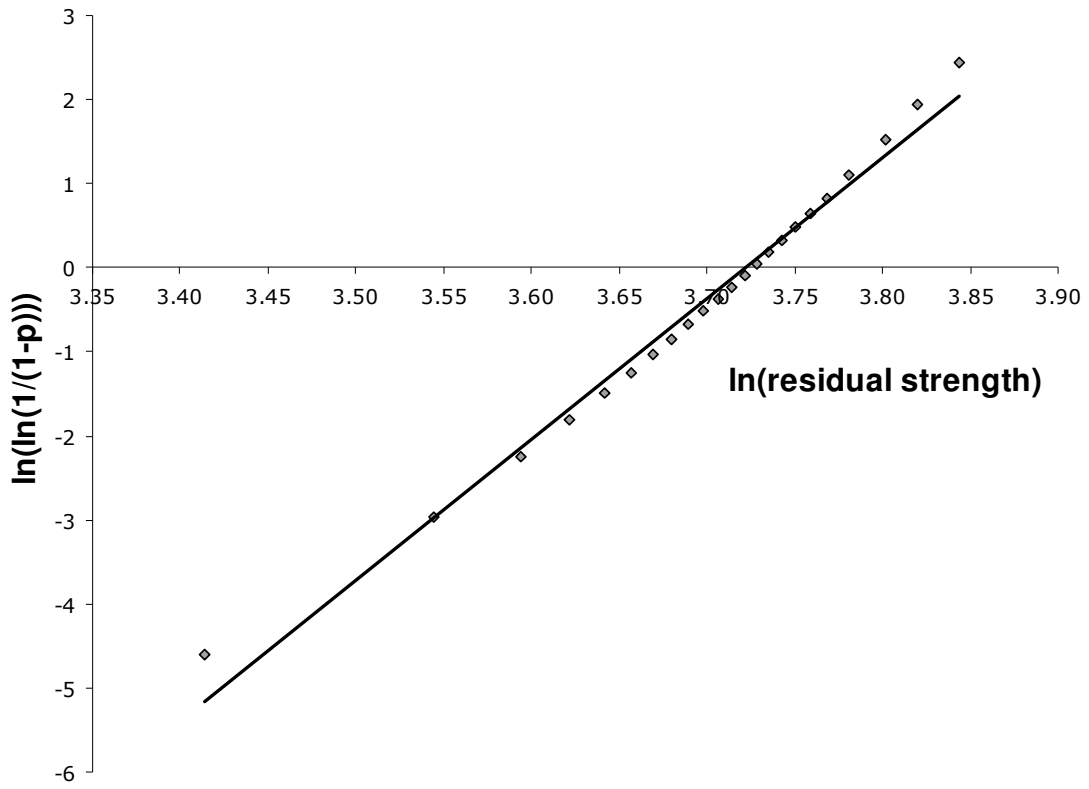


Figure 22: Weibull analysis of residual strength data for E-glass/8084 composite.

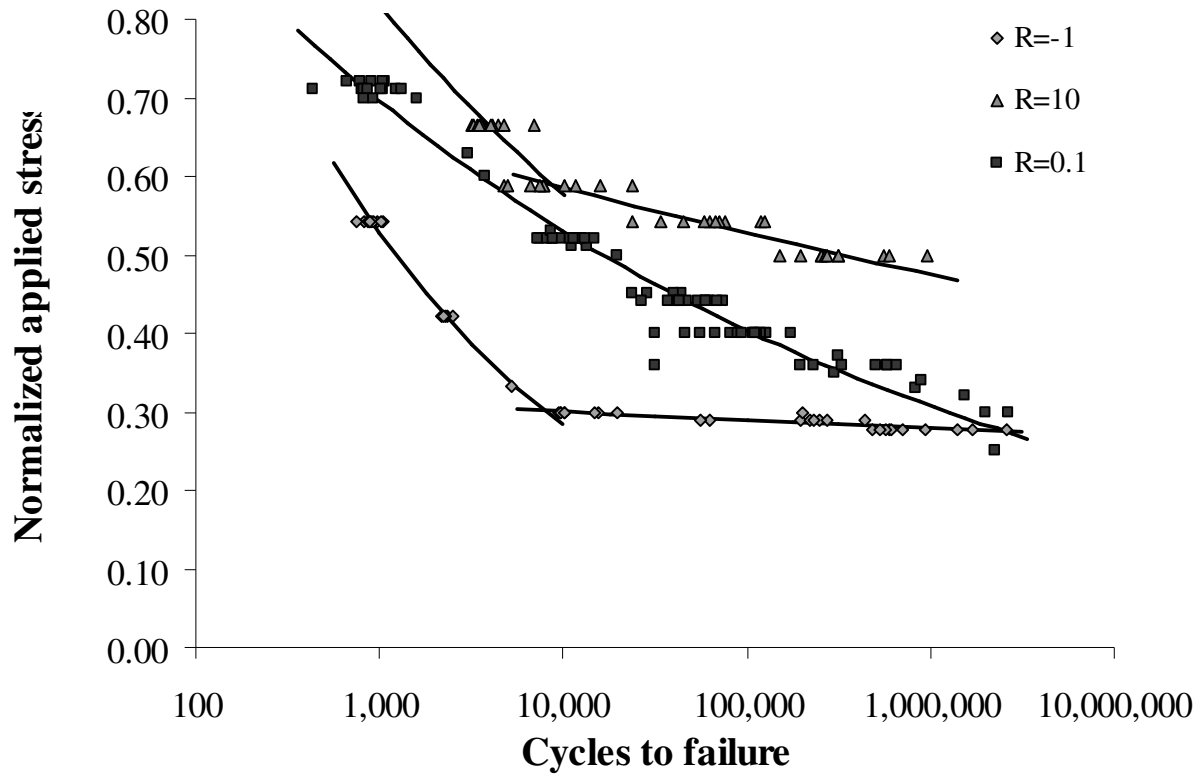


Figure 23: Normalized constant amplitude stress-life (SN) plots for R=0.1, R=-1, and R=10 (E-glass/510-A).

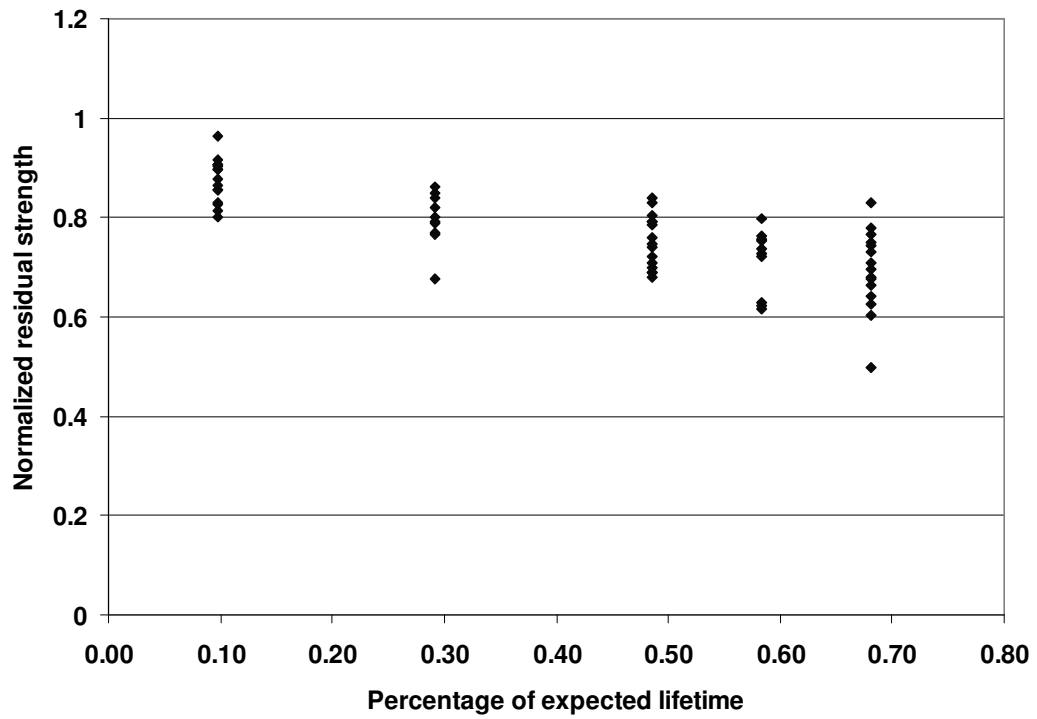


Figure 24: Residual strength data for $R=0.1$ and loading of 44% UTS for E-glass/510-A composite.

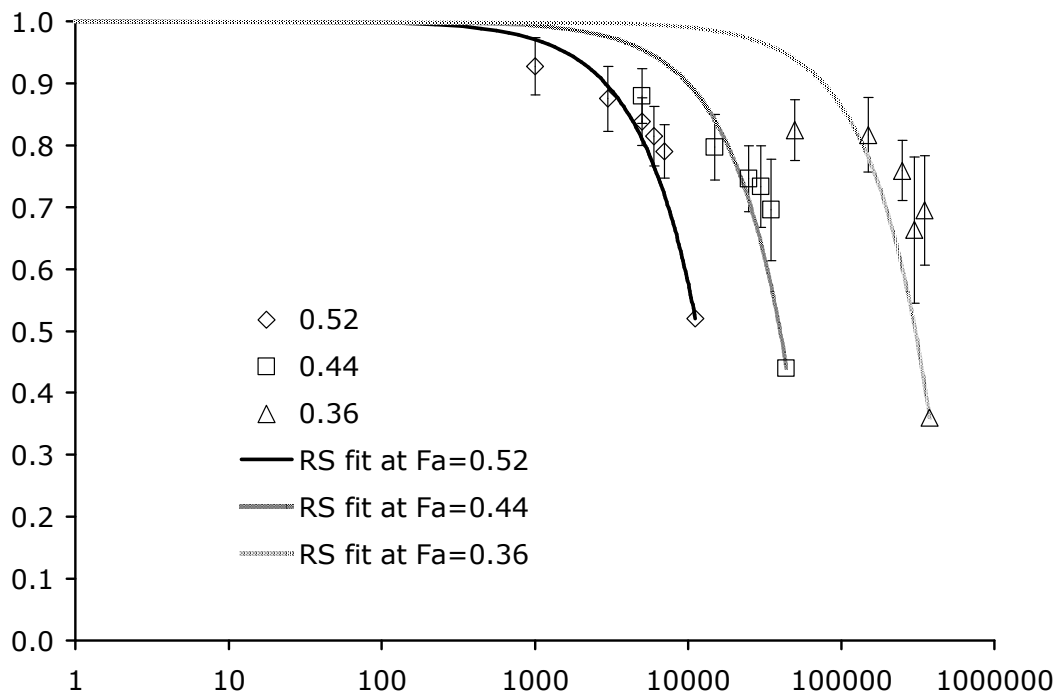
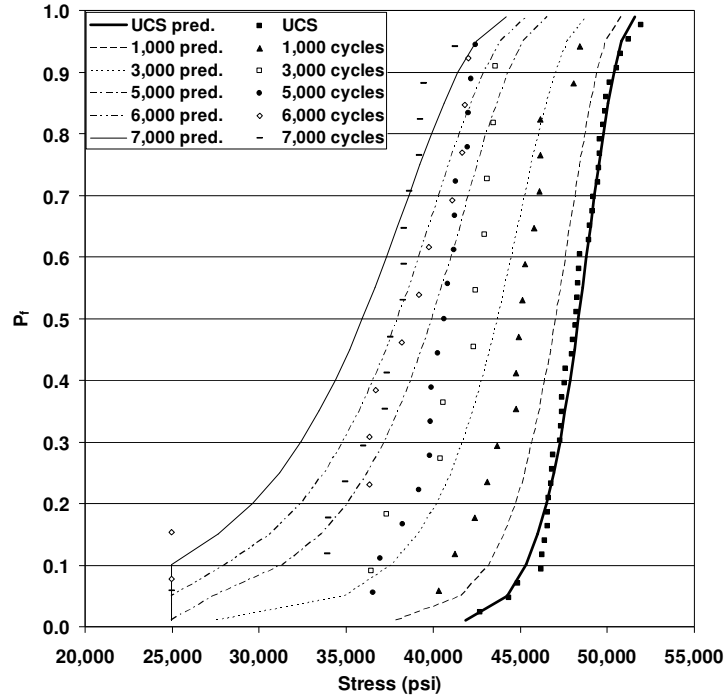
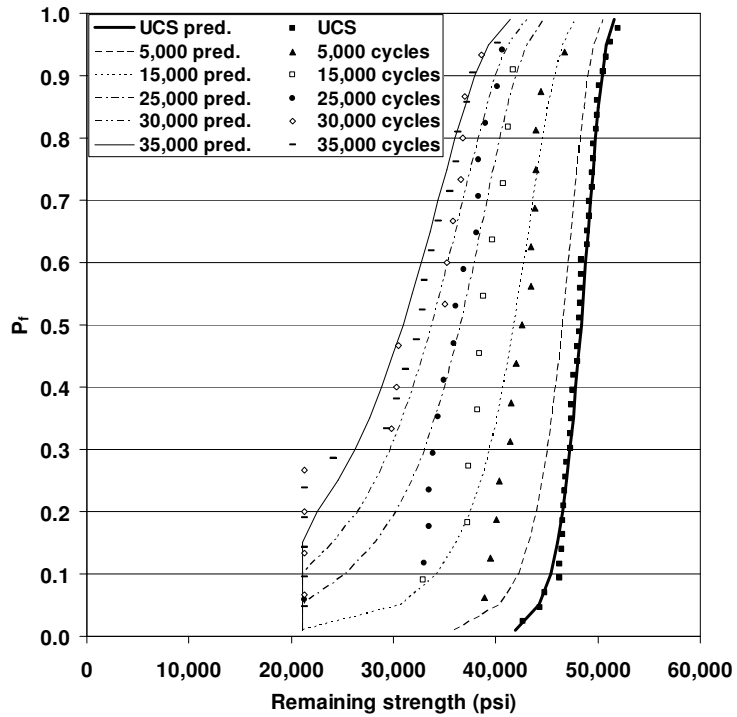


Figure 25: Residual strength fit plots for E-glass/510-A material, at R=0.1 constant-amplitude loading.

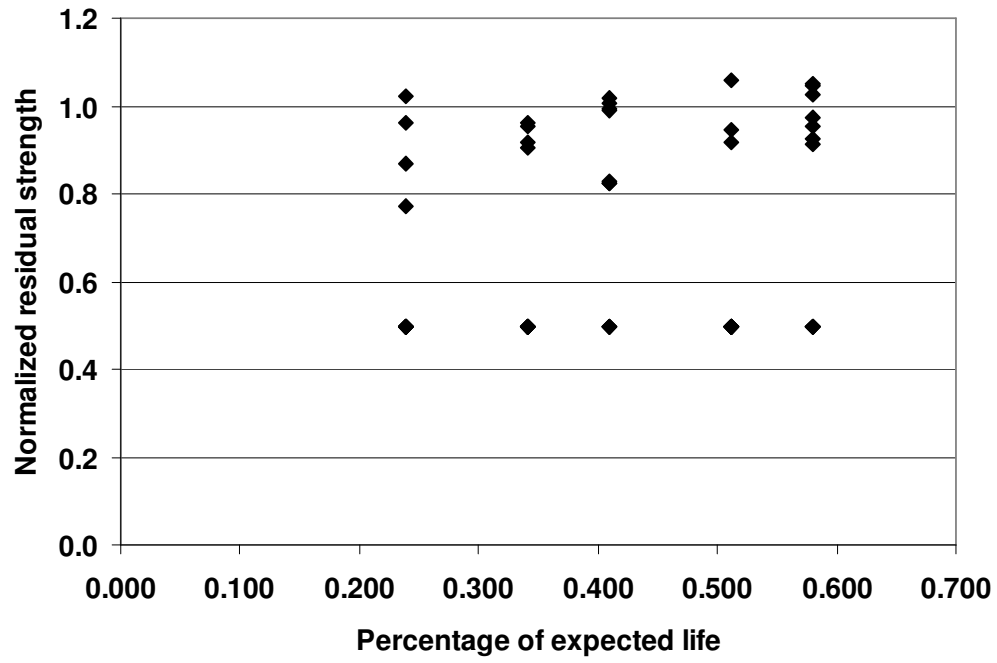


a)

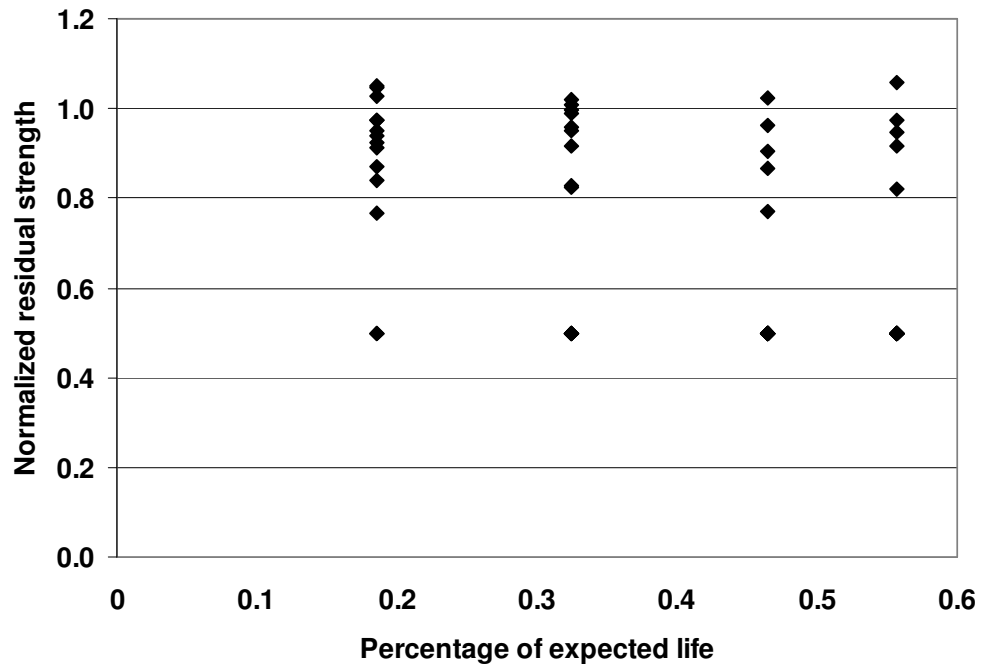


b)

Figure 26: Residual strength data and predicted CDFs for $R=0.1$ and loading of a) 52% UCS and b) 44% UTS for E-glass/510-A composite.



a)



b)

Figure 27: Residual strength data for a) $R = -1$, and b) $R = 10$ for E-glass/510-A composite showing sudden-death behavior, especially for $R = 10$.

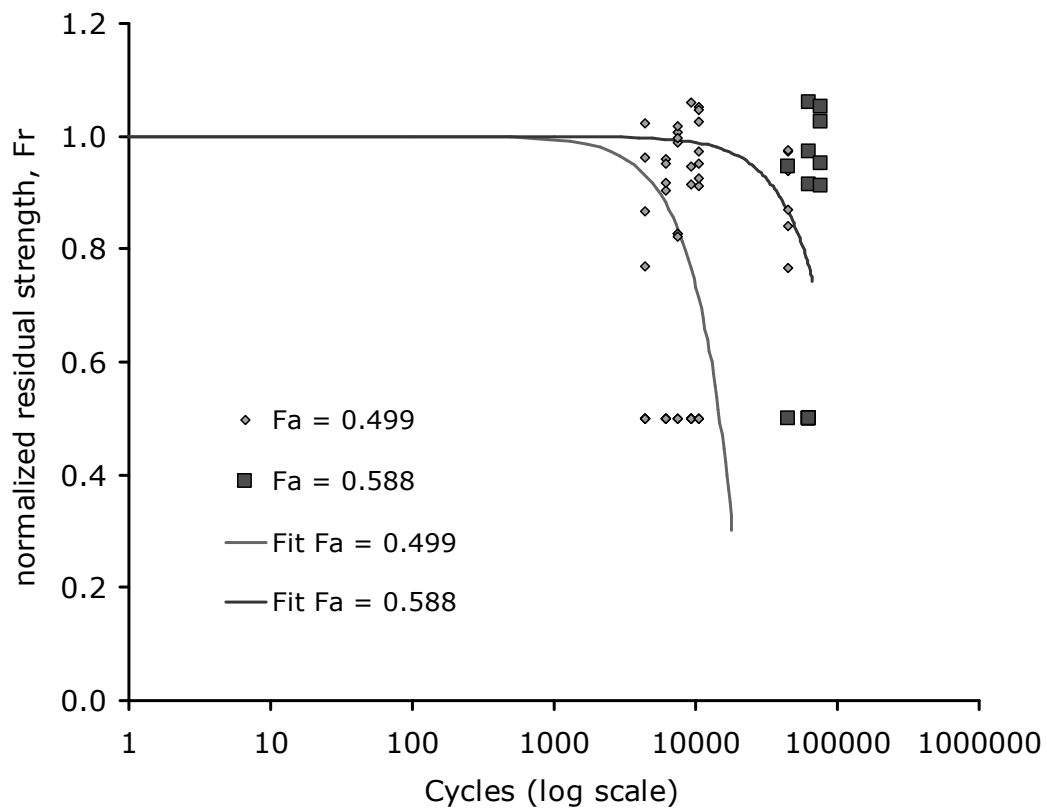


Figure 28: Residual strength fit plots for E-glass/510-A material, at $R=-1$ constant-amplitude loading.

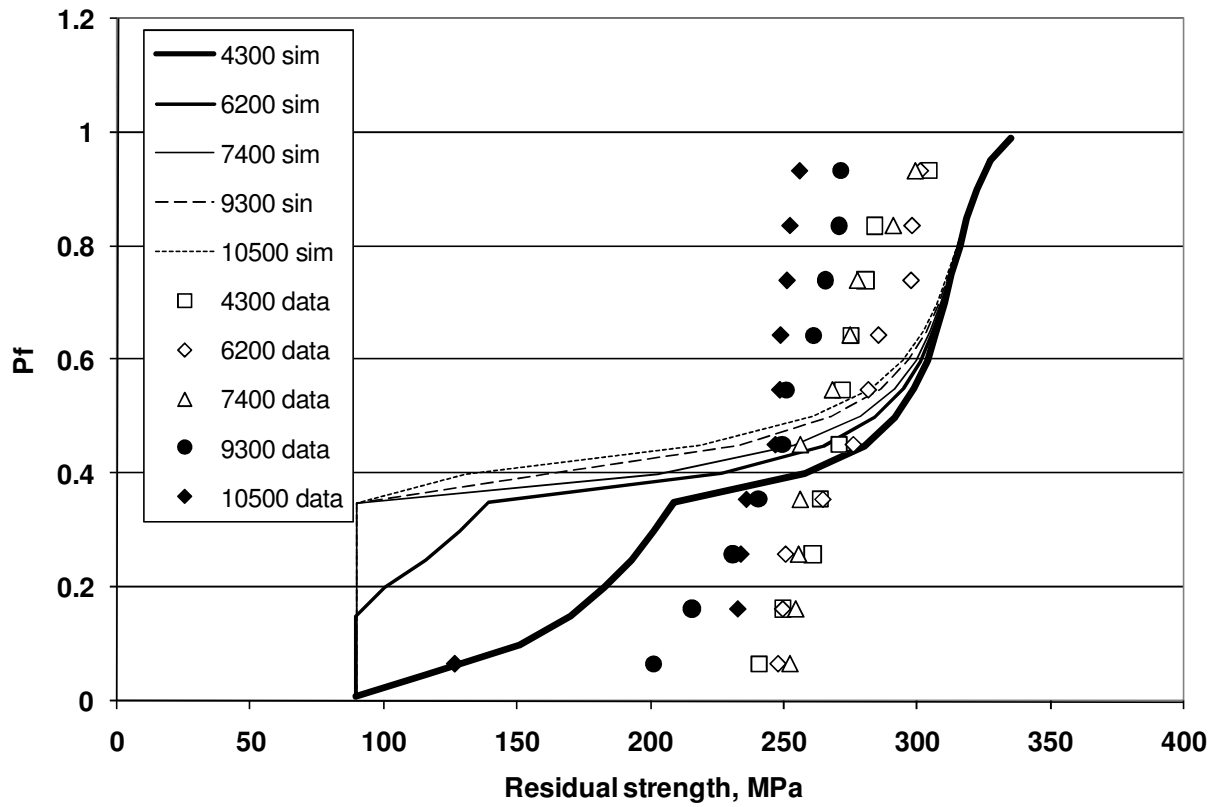


Figure 29: Unacceptable cumulative distribution function for the residual strength of E-glass/510-A material at loading ratio of R=-1 resulting from numerical difficulties.

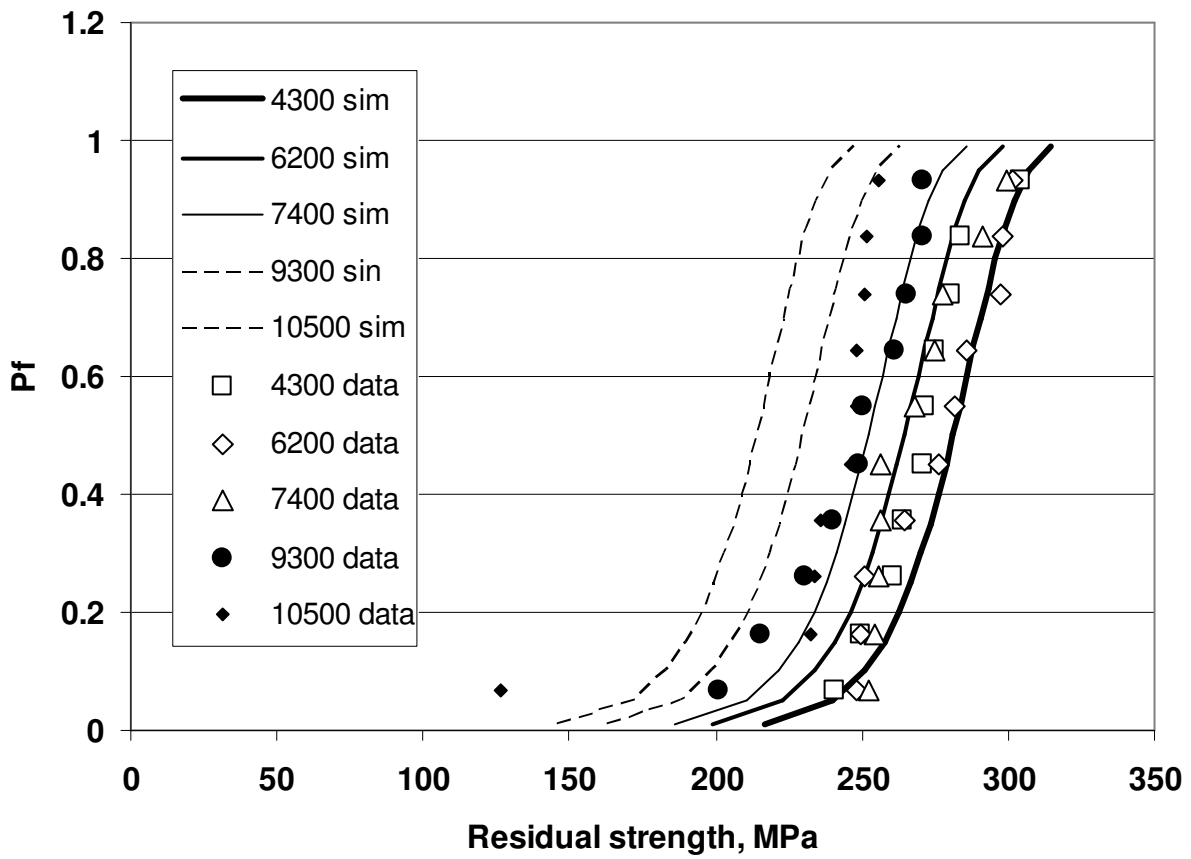


Figure 30: An acceptable cumulative distribution function for the residual strength of E-glass/510-A material at loading ratio of $R=-1$ at a loading of 29.9% UCS and several lifetimes.

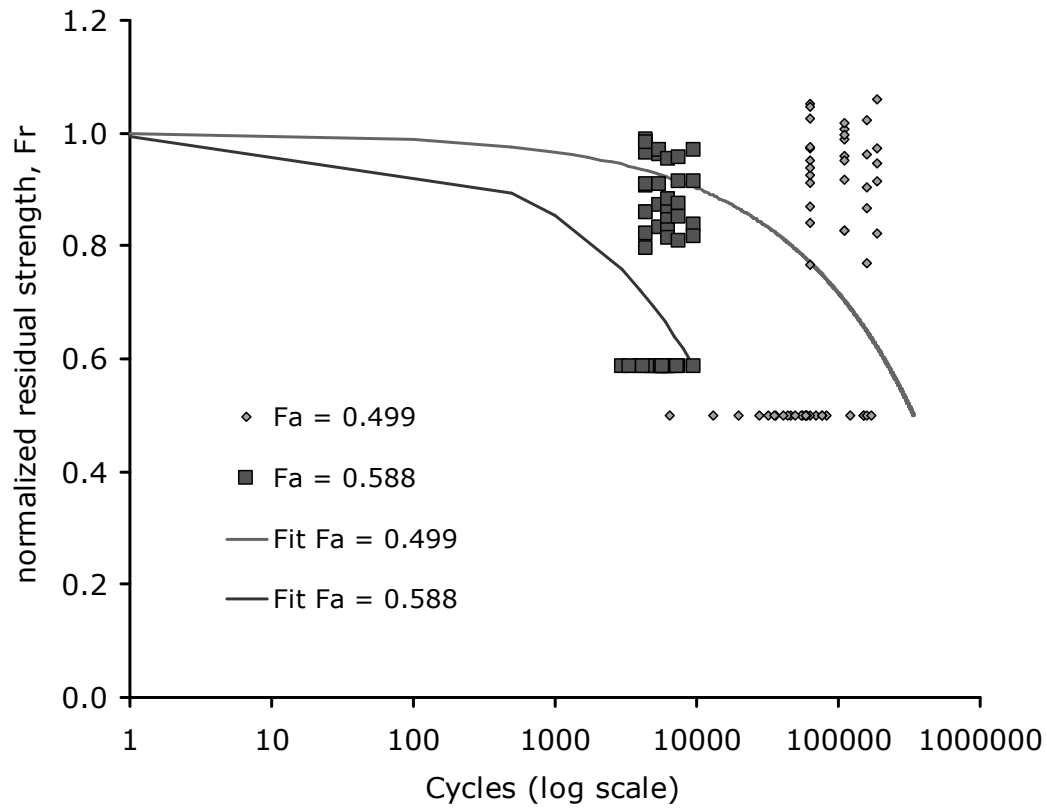


Figure 31: Residual strength data and model fit for R=10 for E-glass/510-A material under constant-amplitude load.

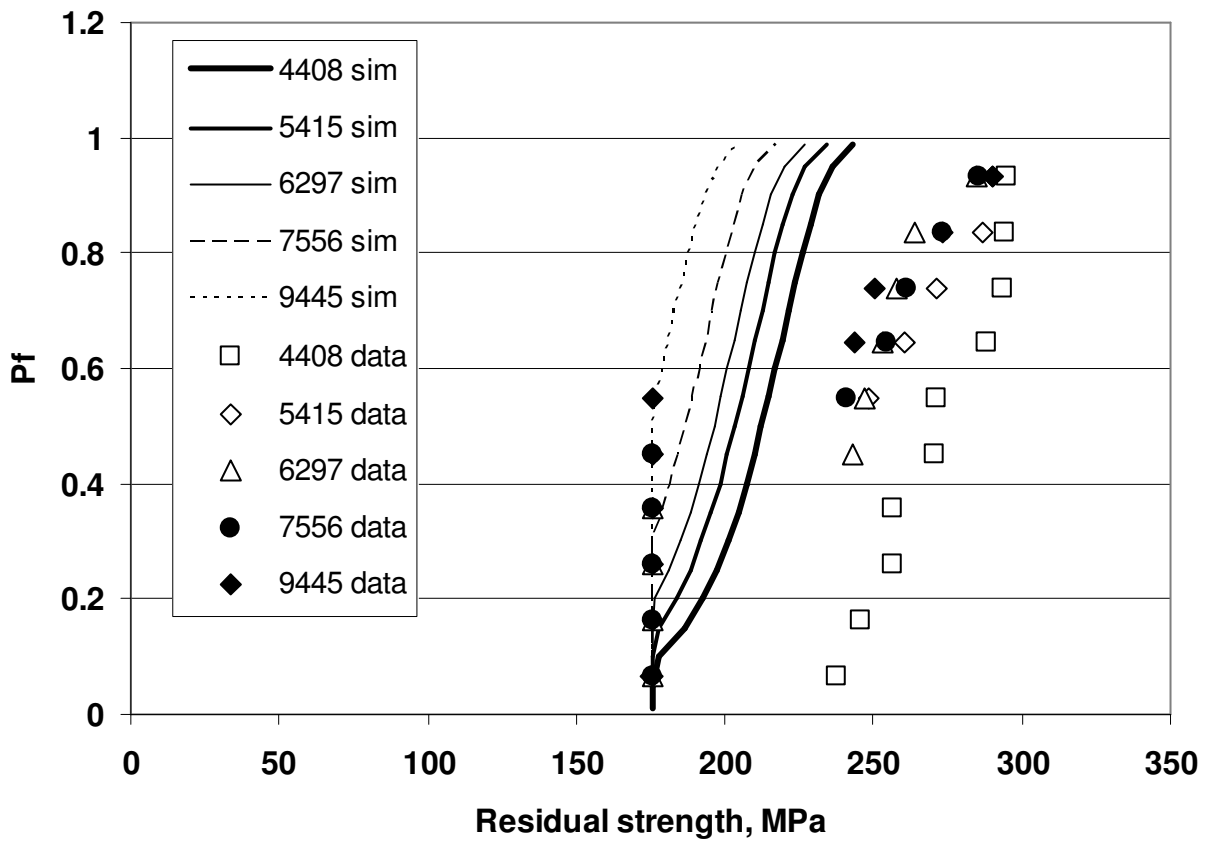


Figure 32: Cumulative distribution function for the residual strength of E-glass/510-A material at loading ratio of R=10 and several lifetimes.

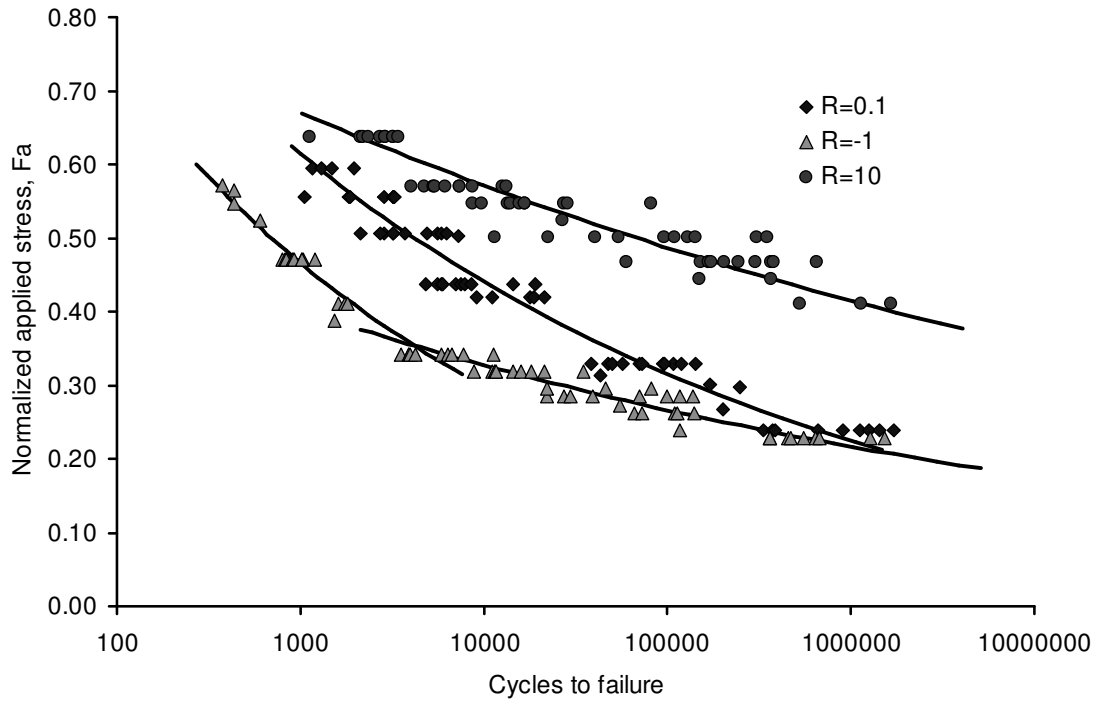


Figure 33: Constant amplitude stress-life (SN) plots for $R=0.1$, $R=-1$, and $R=10$ (E-glass/8084).

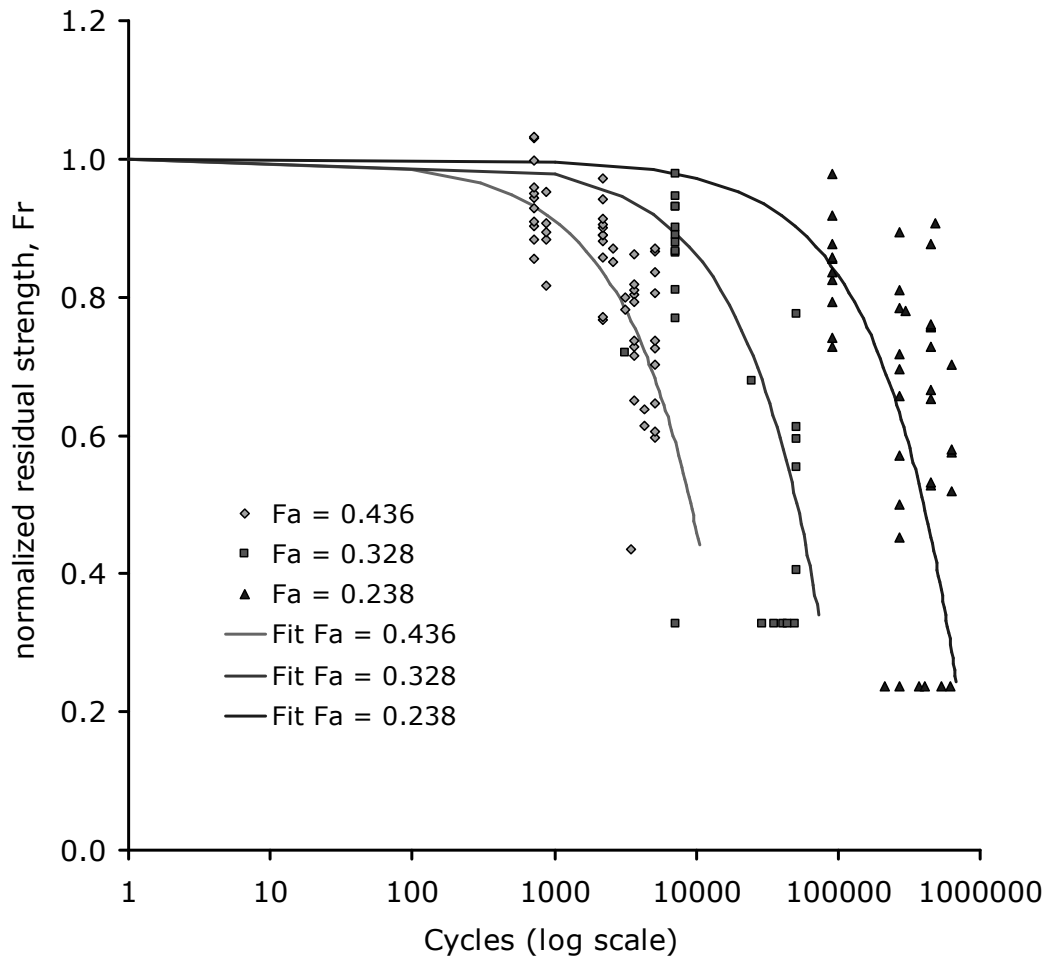


Figure 34: Residual strength data and model fit for $R=0.1$ for E-glass/8084 material under constant-amplitude loading.

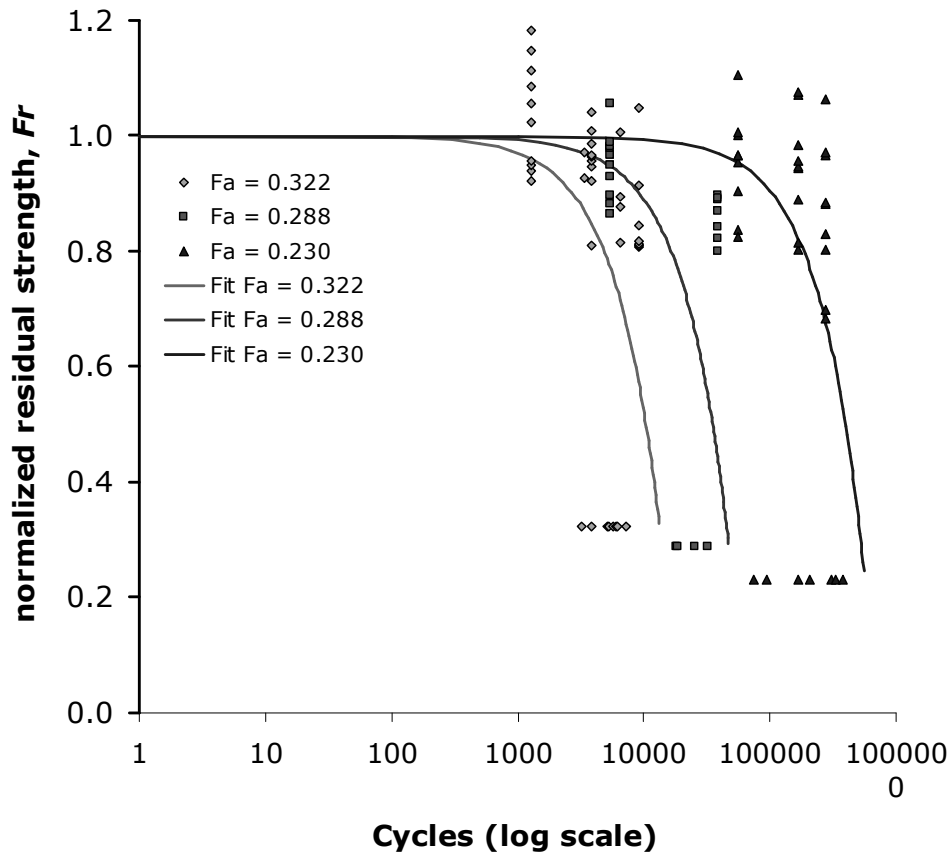


Figure 35: Residual strength and model fit for E-glass/8084 material at a constant-amplitude loading ratio of $R=-1$.

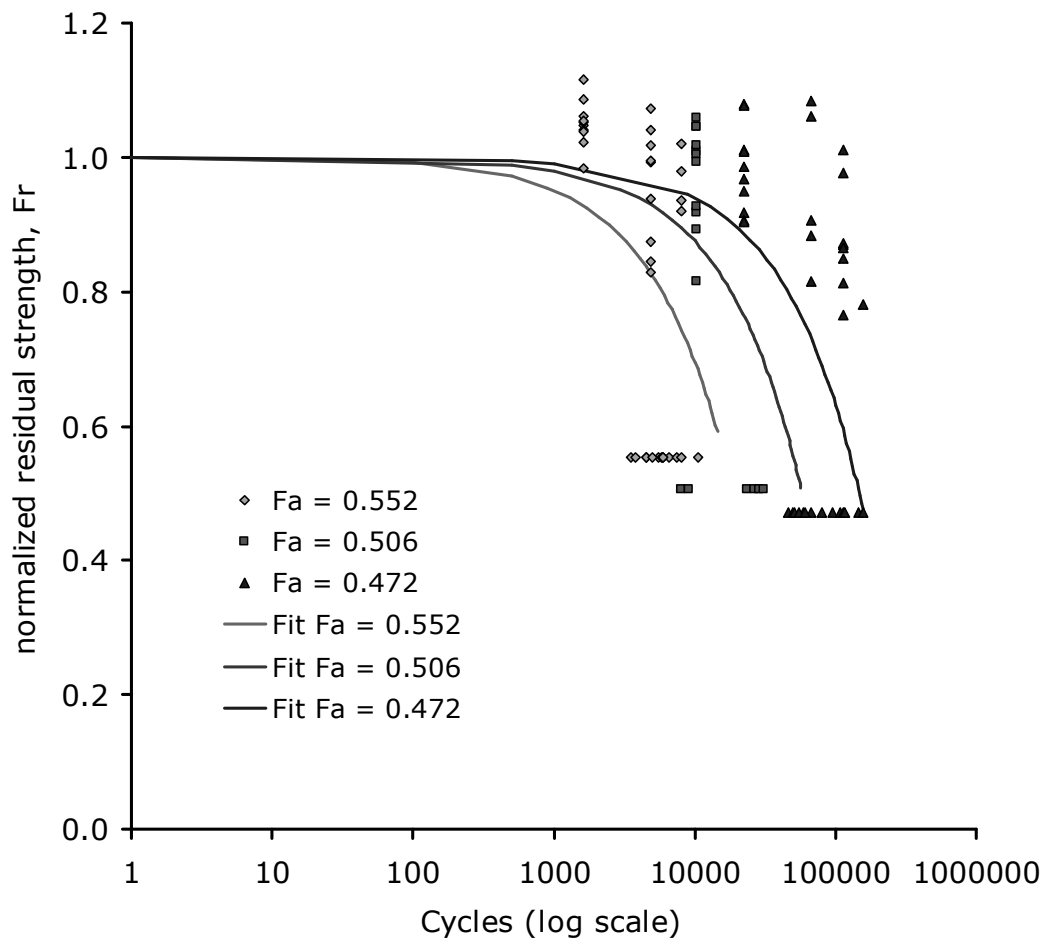


Figure 36: Residual strength data and model fit for E-glass/8084 for a constant-amplitude loading ratio of $R=10$.

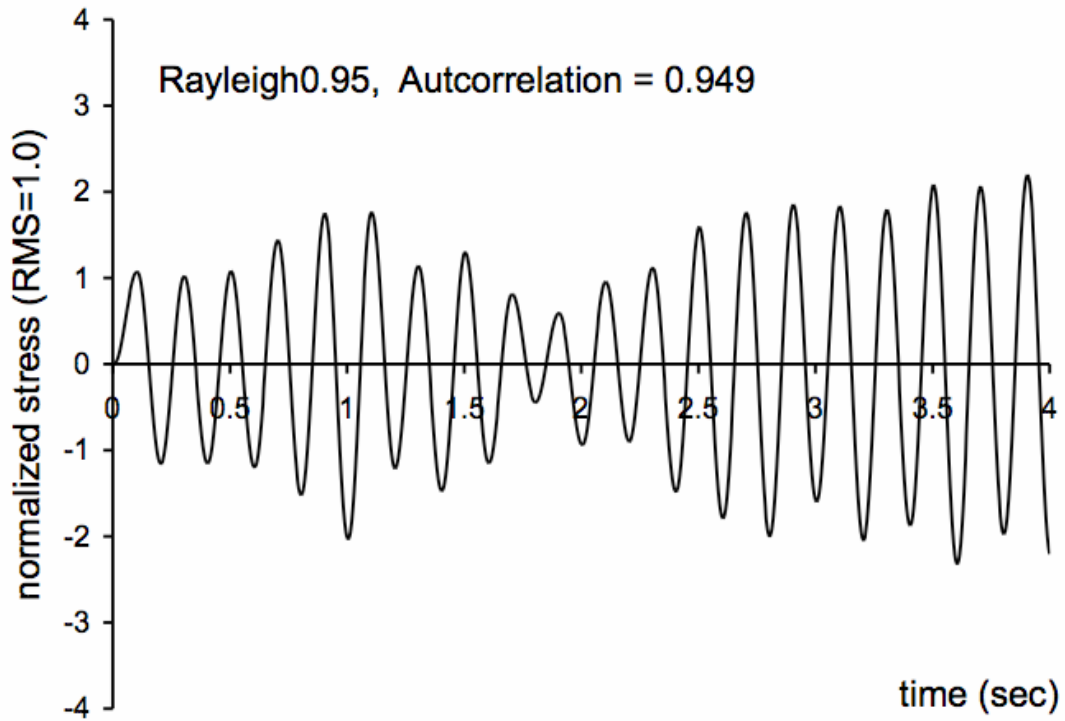


Figure 37: The first few seconds of the time history of the Rayleigh-distributed spectrum with autocorrelation of 0.95.

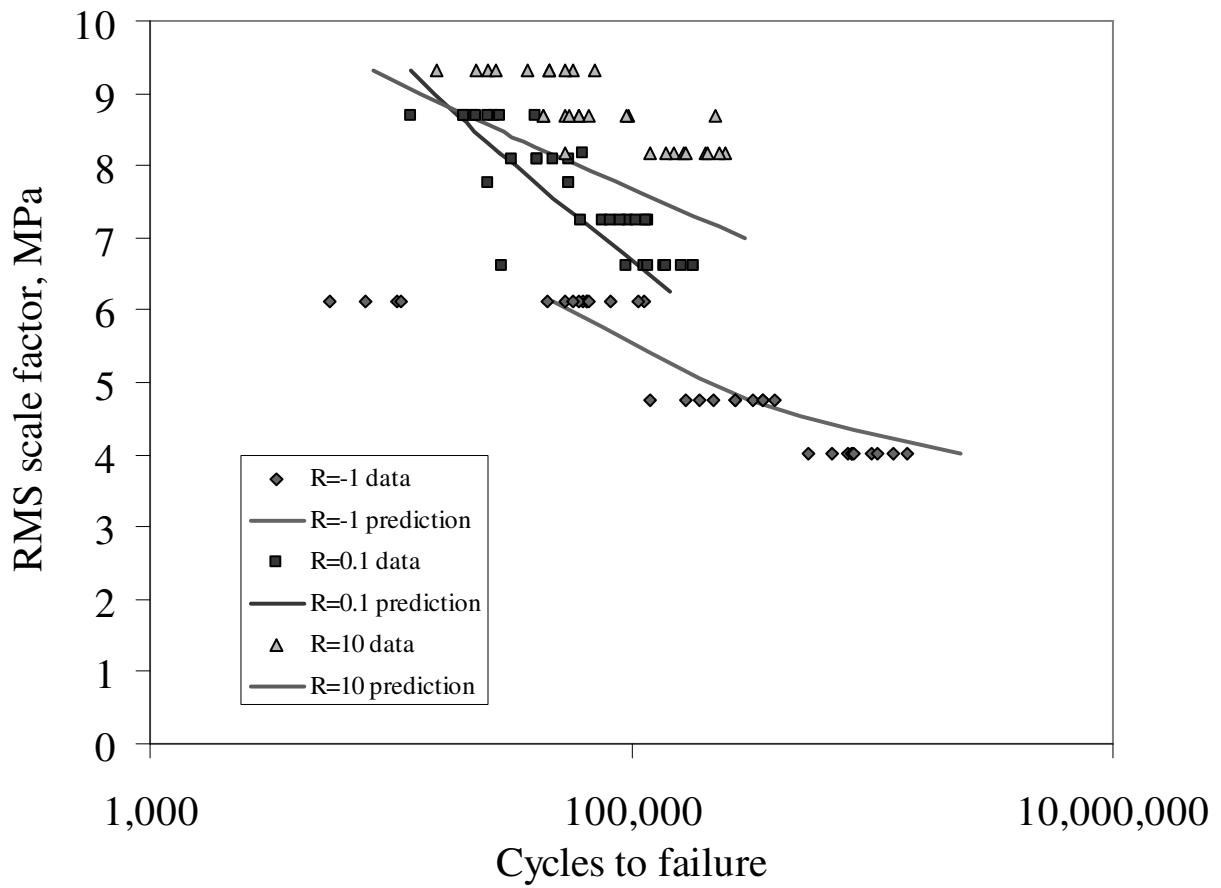


Figure 38: SN plot for variable-amplitude spectrum loading of E-glass/8084 material at R=10.

5. Testing of Hygrothermally Aged E-glass/Epoxy Cylindrical Laminates Using a Novel Fixture for Simulating Internal Pressure

The following paper has been submitted to the Journal of Composites for Construction in December 2007, and is currently in the review process. Formatting and typesetting have been changed for consistency with the rest of this document.

Testing of Hygrothermally Aged E-glass/Epoxy Cylindrical Laminates Using a Novel Fixture for Simulating Internal Pressure

Jason Cain, Scott Case, Jack Lesko

Department of Engineering Science and Mechanics
Virginia Polytechnic Institute and State University

5.1. Abstract

This paper discusses the development of a novel test fixture for applying a uniform radial stress to cylindrical composite laminates in such a way as to eliminate bending moments and axial loads. This fixture requires the use of easily-fabricated poly-tetrafluoroethylene (PTFE) ring seals. These seals, which fit just inside the composite sample, are designed to be internally pressurized in the fixture and expand outwards, applying a uniform radial load to the sample. The results of detailed mechanics analyses of the PTFE ring seal and composite sample are presented, which estimate the radial stress applied to the composite sample as a fraction of the applied internal hydraulic pressure.

Further, results are presented from a prolonged hygrothermal aging study, in which the E-glass/epoxy, cylindrically-wound composite samples are aged under varying hygrothermal conditions (ambient dry; and 30°C, 40°C, and 50°C submerged). At various points during the aging, a subset of samples are removed and destructively tested to measure the reduction in strength from the initial values. Annular specimens are tested using the fixture, and hoop tensile strengths are recorded. In addition, samples cut axially from the cylindrical composite tubes are used to evaluate tensile and compressive axial strengths. Arrhenius fits are used to calculate activation energies for the strength loss in the axial (compression) and hoop (tension) directions.

5.2. Introduction

Composites are recognized as an attractive alternative to traditional methods of reinforcement for concrete infrastructure. In particular, concrete-filled fiber-reinforced polymer (CFFRP) composites show promise for use as reinforcement and protection of concrete columns and piles.

In this application, the composite provides reinforcement for the concrete during axial compression [87], primarily by confinement of the concrete [88]. Fam [88] developed a confinement model that showed that the axial load carrying capability of the CFFRP can be significantly greater than the sum of the load capacities of the concrete and FRP tube. Because the piles are usually subjected to wet environments, much of the research has been aimed at understanding the effects of moisture and temperature on the strength of the composite and concrete materials. Several researchers have investigated the behavior and durability of composite-reinforced concrete piles [89-94].

In this study, we characterize the nature of the strength degradation seen in cylindrical E-glass/epoxy composites as a function of time and hygrothermal state for moderate temperatures. Toward this end, material strengths in the axial and circumferential directions were measured for samples aged while immersed in water at three different temperatures (30°C, 40°C, and 50°C). To make these measurements, samples were removed at a number of times over the course of 500 days. The strength degradation was modeled using an Arrhenius relationship, as this has been found to be useful by others investigating hygrothermal strength degradation of glass fiber reinforced polymer composites (FRP) [72, 95, 96].

Axial strength was measured using traditional methods; however, the hoop tension strength was found using a novel fixture that allowed short, annular test samples to be loaded outward radially to simulate an internal pressure load. This fixture used hydraulic oil to exert pressure on the inner diameter of a custom PTFE ring seal, which fit just inside the sample, and which was forced by the pressure to expand radially, loading the sample radially in a manner similar to the loading that the composite is expected to see in operation. This is in contrast to other popular test methods, such as the split-disk method [97, 98], which has the disadvantage of introducing undesired bending stresses to the sample near the edges of the split-disk.

The fixture necessitated the machining of custom PTFE seals to transfer the pressure load of the hydraulic oil to the inner surface of the annular test specimen. These seals were relatively simple in design and were manufactured easily on a small, desktop lathe. The seals were found to be reusable many times, and allowed for a uniform, almost purely radial load to be applied to the specimen. With this configuration the samples experienced a “free-free” boundary condition at the ends, unlike a typical internal pressure test in which end cap effects may be significant.

5.3. Material/testing description

The material examined in this study was a helically-wound cylindrical E-glass/Epoxy composite, with a lay-up of $[(86/8)_2/\overline{86}]_5$ and a nominal inner diameter of 16.26 cm. The material was received as 33 cm long pre-cut cylindrical sections, which were subsequently post-cured and cut into test specimens. The post-curing, which consisted of a 4-hour heat treatment at 82°C, was undertaken in an attempt to minimize material property changes as a result of advancing cure of the matrix with time [83].

In order to assess the material strength degradation as a function of water temperature and moisture, specimens were stored under four conditions: 1) in room-temperature air, and submerged in distilled water at 2) 30°C, 3) 40°C, and 4) 50°C. The time dependence of the material degradation under these hygrothermal conditions was assessed by making measurements at regular intervals through time, as can be seen in Table 13, where the time refers to the accumulated hygrothermal aging time. On each day of testing, three types of quasi-static testing were performed: axial tension, axial compression, and hoop tension (burst).

Moisture uptake was also monitored by periodically measuring the mass of “traveler” specimens from each hygrothermal condition. Four traveler specimens were used for each water temperature.

Table 13: Test plan for composite testing (number of replicates).

	Days of Aging					
	0	10	30	100	300	500
30°C Water Aging						
Hoop Tension	30	10	10	10	10	10
Axial Tension	25	10	10	10	10	10
Axial Compression	25	10	10	10	10	10
40°C Water Aging						
Hoop Tension	0	5	5	5	5	5
Axial Compression	0	5	5	5	5	5
50°C Water Aging						
Hoop Tension	0	5	5	5	5	5
Axial Compression	0	5	5	5	5	5
Ambient Air Aged						
Hoop Tension	0	5	5	5	5	5
Axial Compression	0	5	5	5	5	5

5.3.1. Axial tension and compression testing

Axial tension specimens, which were 2.54 cm wide (measured across the outside edges of the cylindrical section) and 16.5 cm long, were cut from the cylinders using a custom fixture that allowed for cuts to be made in the plane of the centerline of the cylinder. The curved shape of the specimens necessitated special grip inserts which allowed them to be gripped in a standard 90 kN servo-hydraulic load frame without introducing unwanted bending moments. A gage length of approximately 7.6 cm was used for the axial tension tests and the specimens were loaded quasi-statically (under load control) at a load rate of 667 N/sec until failure. Load values were recorded from the controller output, and strain data was collected using a 2.54 cm extensometer.

Axial compression specimens were cut in a similar manner to the axial tension tests, but were sized 1.27cm wide and 14.0 cm long. The samples were end-loaded, with a gage length of 1.27 cm, in compression using an End-Loaded Side-Supported (ELSS) fixture manufactured by Wyoming Test Fixtures, Inc. and pictured in Figure 39, and a screw-driven load frame with platens. The samples were loaded quasi-statically until failure (under displacement control) at a rate of 2 mm/min. Strain data was collected from a 2.54 cm extensometer mounted to the ELSS fixture.

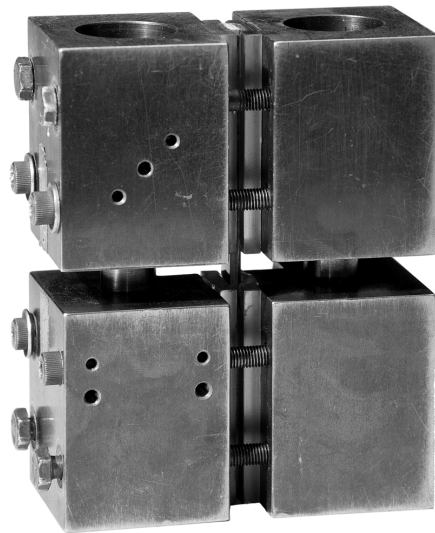


Figure 39: End-loaded side-supported fixture for axial compression testing.

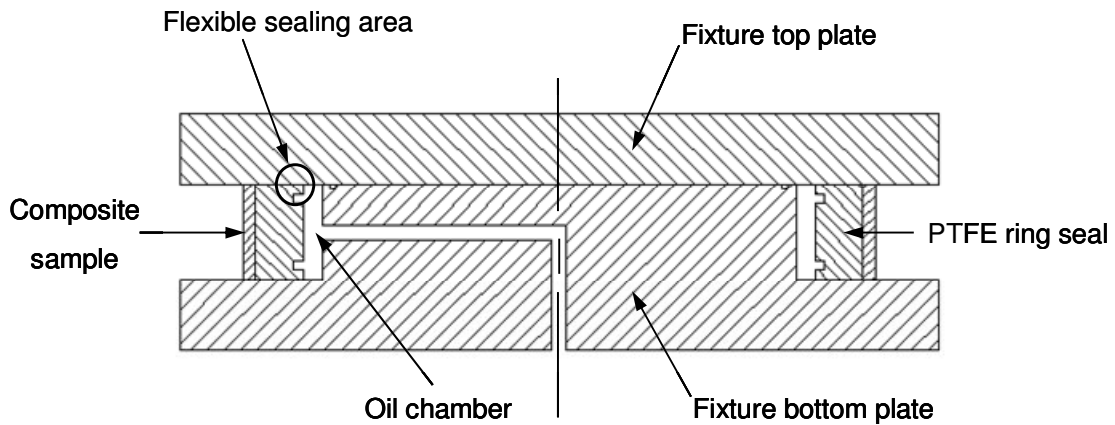
5.3.2. Hoop tension (burst) testing

The annular hoop tension specimens were 2.54 cm long (along the cylinder axis) and were loaded outward radially using the specially-machined PTFE seal and fixture. The fixture and seal provided containment for the hydraulic fluid that was used to load the specimen, as shown in Figure 40a, in which the dark composite sample is shown surrounding the white PTFE ring seal. In the annular space between the seal and the fixture (see Figure 40b), the fluid is increasingly pressurized using a hand pump, and the seal is forced outward into the sample, loading it radially in a near-uniform way. Annular grooves cut into the inner face of the seal create flexible sealing features, which, under pressure, deform outward axially to form a seal with the top and bottom plates of the fixture. The thickness of the seal in the axial direction is just smaller than the space between the top and bottom fixture plates, so that the only portion of the seal that is in contact with them is the small sealing area in order to reduce friction that might affect the results.

The outward radial stress applied to the sample by the seal was calculated by scaling the applied internal pressure to account for the load carried by the PTFE seal (see Section 4 for details of this calculation). Strain gages on the composite sample recorded hoop and axial strain, and the pressure was recorded as well. The breaking strength of each sample was recorded, and the approximate hoop stiffness was calculated from the measurement of the internal pressure and the axial and hoop strains of the sample. For the first several tests, three sets of strain gages, located 120° apart, were used to check for axisymmetric loading. After these results were found to suggest very good axisymmetric loading, only one set of strain gages (one hoop gage and one axial gage) per specimen was used.



(a) Hoop tension burst fixture photos



(b) Hoop tension burst fixture section view through center

Figure 40: Fixture and PTFE seal used for hoop burst testing.

5.4. Mechanics Analysis of PTFE Seal and Composite Cylindrical Hoop Tension Samples

In the hoop-tension tests performed using the fixture in Figure 40, the PTFE ring seal may carry a significant portion of the radial load. As a result, the radial stress applied to the composite sample by the ring seal (i.e. the radial stress at the interface between the seal and sample), is reduced somewhat from the internal pressure applied at the inner radius of the seal. The

reduction in the radial stress can be calculated by combining an elasticity analysis of the seal and a laminate analysis of the composite sample; a brief summary of this analysis follows. The analysis was performed in cylindrical coordinates, in which x is the axial direction, θ the circumferential direction, and r the radial direction. The displacements in the x , θ , and r directions are u , v , and w , respectively.

5.4.1. Elasticity Analysis of PTFE Ring Seal

The elasticity analysis for the ring seal was performed under the following assumptions:

- axisymmetric geometry and loading;
- linear elasticity;
- and, the seal is long in the axial direction.

Despite the short length of the seal in the axial direction in reality, the third assumption is valid according to simple finite element models that suggest that for this loading case the stresses and strains do not vary significantly in the axial direction, i.e. they are not functions of x , the distance along the axis of the cylinder.

If it is further assumed that no axial torque is applied, no rigid body motions are allowed, and no shear tractions are present on the radial faces of the seal, then the cylindrical equations of elasticity (equilibrium, strain-displacement, and constitutive equations) can be combined, resulting in equations of the following form.

$$u(x, r) = Bx \quad (34)$$

$$v(x, r) = 0 \quad (35)$$

$$w(r) = \frac{K_2}{r} + K_1 r \quad (36)$$

$$\sigma_x(r) = BC_{11} + C_{13} \left(K_1 - \frac{K_2}{r^2} \right) + C_{12} \left(K_1 + \frac{K_2}{r^2} \right) \quad (37)$$

$$\sigma_\theta(r) = BC_{12} + C_{23} \left(K_1 - \frac{K_2}{r^2} \right) + C_{22} \left(K_1 + \frac{K_2}{r^2} \right) \quad (38)$$

$$\sigma_r(r) = BC_{13} + C_{33} \left(K_1 - \frac{K_2}{r^2} \right) + C_{23} \left(K_1 + \frac{K_2}{r^2} \right) \quad (39)$$

where B , K_1 , and K_2 are unknown constants, and the C_{ij} are the elements of the stiffness matrix given by

$$C_{ij} = \frac{(1-\nu^2)E}{1-\bar{\nu}}; \quad i = j \quad (40)$$

$$C_{ij} = \frac{(\nu+\nu^2)E}{1-\bar{\nu}}; \quad i \neq j \quad (41)$$

$$\bar{\nu} = 3\nu^2 + 2\nu^3. \quad (42)$$

The following boundary conditions are applied on the radial stress on the inner and outer faces of the seal using equation 39:

$$\sigma_r(r = r_{inner}) = -p \quad (43)$$

$$\sigma_r(r = r_{interface}) = -\sigma_r^* \quad (44)$$

where r_{inner} is the inner radius of the seal, p is the internal pressure applied at that inner radius, $r_{interface}$ is the outer radius of the seal where it interfaces with the composite sample, and σ_r^* is the radial stress applied to the composite sample by the seal.

Since the seal is free of applied axial loads, and since the stresses are assumed not to be functions of x , the following condition can be applied using equation 37:

$$\int_{r_{inner}}^{r_{interface}} r \sigma_x(r) dr = 0. \quad (45)$$

The equations resulting from applying equations 37 and 39 to equations 43, 44, and 45 can be used to solve for the constants B , K_1 and K_2 . As manufactured, the inner and outer radii of the PTFE seal are $r_{inner}=6.86$ cm and $r_{interface}=8.13$ cm, respectively. The tensile modulus and Poisson's ratio are taken from the PTFE manufacturer's data (Enflo Corporation) to be $E=0.552$ GPa and $\nu=0.46$, respectively. (The tensile modulus is assumed to be the modulus during low strain, which is the regime under which the seal operates before failure of the composite specimen.) After these numerical geometric and material properties are substituted, the constants are found to be, for pressure and stress in units of pascals,

$$K_1 = (2.419 \times 10^{-9})p - (3.398 \times 10^{-9})\sigma_r^* \quad (46)$$

$$K_2 = (4.321 \times 10^{-11})(p - \sigma_r^*) \quad (47)$$

$$B = (-4.122 \times 10^{-9})p + (5.790 \times 10^{-9})\sigma_r^* \quad (48)$$

Finally, equations 46 and 47 are combined with equation 36 to find the displacement in meters of the outer radial surface of the seal as (again for units of Pa).

$$w(r = r_{interface}) = (7.283 \times 10^{-10})p - (8.079 \times 10^{-10})\sigma_r^* \quad (49)$$

This equation will be used with the result from the laminate analysis to assess the relationship between the radial pressure at the interface of the seal and composite sample to the inner applied hydraulic pressure.

5.4.2. Donnell Theory Laminate Analysis of Cylindrical Composite Sample

For the composite sample, a standard CLT analysis was used to find the ABD matrix of the laminate. The material and geometric parameters used were as follows:

Fiber-direction modulus of ply,	$E_1 = 50.0$ GPa
Transverse-direction modulus,	$E_2 = 15.2$ GPa
Major Poisson's ratio,	$\nu_{12} = 0.254$
Shear modulus,	$G_{12} = 4.70$ GPa
Inner sample radius,	$r_{interface} = 81.3$ mm
Number of plies,	$n = 9$
Ply thickness,	$t = 0.34$ mm

The moduli values were assumed as typical values for this type of material, which, when used in the Donnell theory analysis, resulted in laminate stiffness values consistent with those measured during testing.

For a symmetric, cylindrical laminate subjected to only a radial load, it can be shown that the radial displacement of the midsurface is given (in terms of the entries in the A matrix; the radial stress at the inner diameter, σ_r^* ; and the radius, R , at the midsurface) by

$$w^0 = \frac{(A_{16}^2 - A_{11}A_{66})\sigma_r^* R^2}{A_{16}^2 A_{22} - 2A_{12}A_{16}A_{26} + A_{11}A_{26}^2 + A_{12}^2 A_{66} - A_{11}A_{22}A_{66}} \quad (50)$$

For the given material properties,

$$w^0 = (6.777 \times 10^{-11})\sigma_r^* \quad (51)$$

The radial displacement of the laminate must equal the radial displacement of the seal on its outer radius. Therefore, by equating the right-hand sides of equations 49 and 51, the ratio of interface pressure to internal pressure is solved for:

$$\frac{\sigma_r^*}{p} = 0.83 \quad (52)$$

Thus, for all hoop tension tests run in this study, it is assumed that the radial stress applied to the composite sample is 83% of the value of the applied internal pressure in the fixture.

5.5. Results

Mechanical testing has been completed through 500 days. However, moisture-uptake measurements have continued through 830 days.

Moisture absorption

Average moisture uptake measurements for the three hygrothermal conditions over approximately 830 days are shown in Figure 41. It can be seen that saturation has been reached at approximately 700 days.

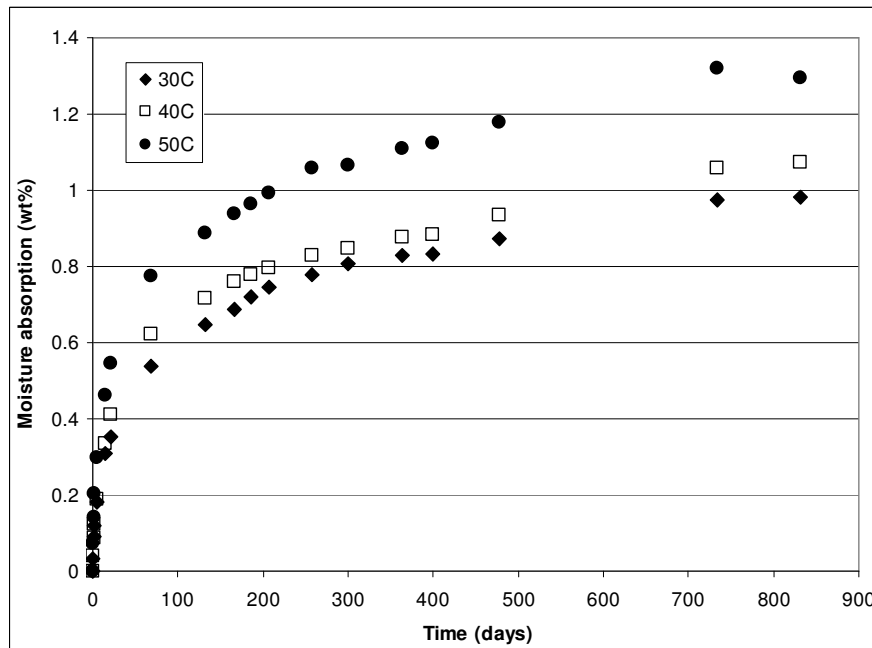


Figure 41: Moisture absorption of E-glass/Epoxy helically-wound tubes.

5.6. Axial compression and tension tests

Axial compression and tension strength data from 500 days of aging are given in Figure 42. Compression data from all three hygrothermal aging conditions suggest that all three lose some strength over 500 days, but that the 40°C and 50°C samples lose a more significant portion of their strength, as expected. The ambient-aged data are relatively unchanged over the course of 300 days, though there is an apparent drop in strength near day 500. Samples from the tension tests, which were aged in 30°C water, appear to also show approximately a 10% decrease in strength over 500 days.

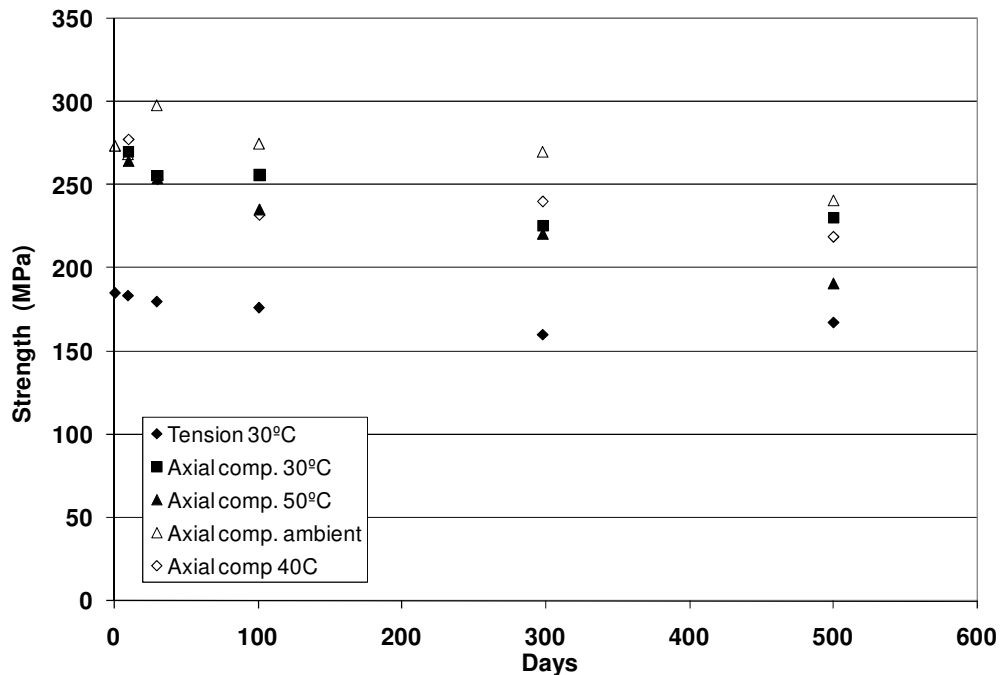


Figure 42: Axial compressive and tensile strength of aged FRP cylinders.

Since it was expected that the diffusivity might accurately be modeled using an Arrhenius relationship, and since hygrothermal degradation of FRPs is often modeled in such a way, it was thought an Arrhenius approach might also be useful, at least as a first estimate, to model the strength degradation of the composite under hygrothermal conditions. The Arrhenius relation is expressed in Equation 53,

$$\log(a_T) = -\frac{E_a}{RT} \quad (53)$$

where a_T is the time-based shift factor, R is the universal gas constant, and T is the temperature. The shift factors for each temperature were found by minimizing the R^2 value for a least squares fit through the strength versus $\log(t a_T)$ data. This method yielded the shift factors given in Table 14.

Table 14: Time-based shift factors for axial compression strength.

Aging water temperature	Shift factor, a_T
30°C	0
40°C	1.27
50°C	2.89

Shifting the data in this way results in the graph of Figure 43, in which the predicted axial strengths are plotted as a function of the shifted time and displayed on a semi-log graph.

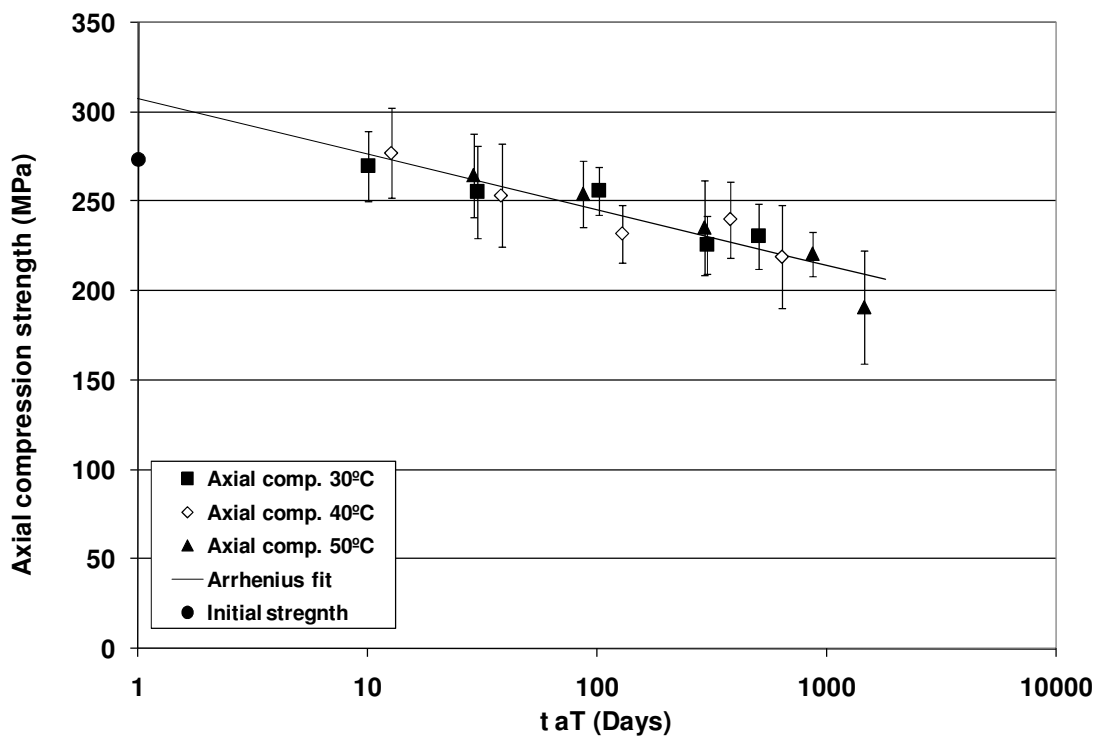


Figure 43: Shifted axial compression strength plot with fit line.

Taking the slope of a line fit through the a_T versus $1/T$ data, we find that an estimate of the activation energy for the compression strength degradation is $E_a=42.9 \text{ kJ/mol}$.

5.7. Hoop tension tests

The PTFE ring seals were found to be reusable for many tests. However, after several tests, the inner and outer diameters of the ring seals were found to have grown by as much as 1.5 mm during the test; this was usually large enough to make fitting the seal into another sample impossible. Fortunately, experimentation showed that annealing the seals in air for 4 hours at a temperature of approximately 310°C resulted in a nearly-full recovery of the original dimensions.

As in the axial tests, the strength degradation in the hoop direction over 500 days was approximately 10% for samples soaked at 30°C, and approximately 20-30% for the 40°C and 50°C samples. These results are shown in Figure 44.

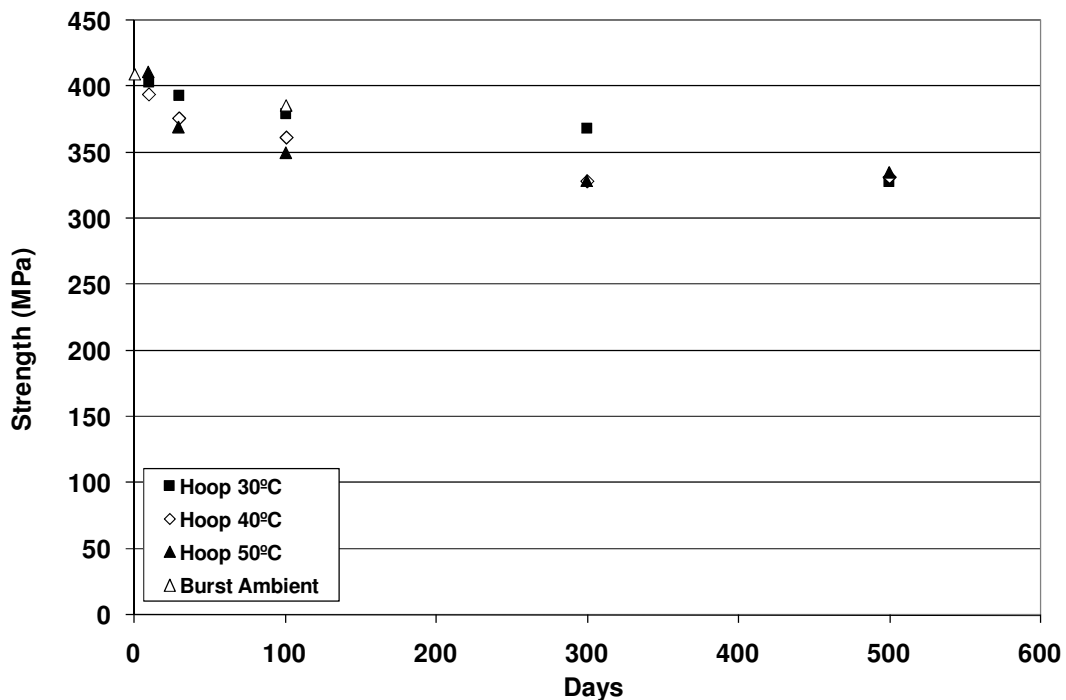


Figure 44: Hoop strength of aged FRP cylinders.

Like the axial compression data, it was assumed the hoop strength data could be modeled by the Arrhenius equation. Following the same procedure as above, we find the shift factors for hoop strength given in Table 15. With these shift factors, the data is plotted in Figure 45, below.

Table 15: Time-based shift factors for hoop tensile strength.

Aging water temperature	Shift factor, a_T
30°C	0
40°C	2.78
50°C	2.83

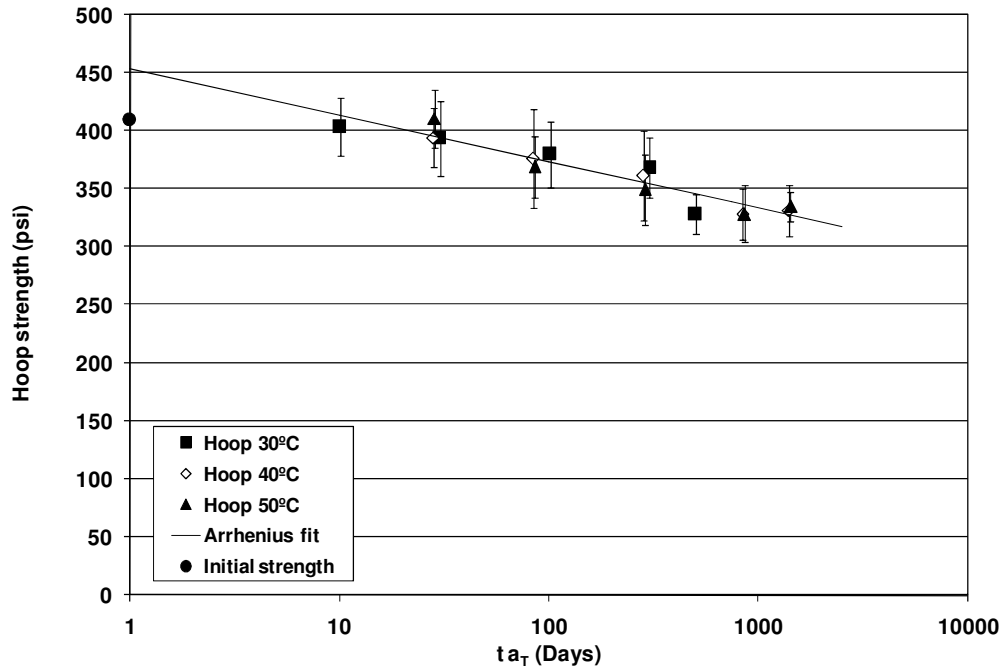


Figure 45: Time-shifted hoop strength with Arrhenius fit line.

Again taking the slope of a line fit through the a_T versus $1/T$ data, we find that an estimate of the activation energy for the hoop tension strength degradation is $E_a=42.8 \text{ kJ/mol}$.

5.8. Conclusions

In this study the quasi-static strength degradation of helically wound E-glass/epoxy laminates was tracked over the course of 500 days as a function of the hygrothermal storage conditions. Specifically, samples were stored in dry, ambient conditions, and submerged in distilled water at

30°, 40°, and 50°C. Axial compression, axial tension, and hoop tension tests were performed at specific intervals of time to monitor the loss in material properties as a function of time and moisture. As expected, higher temperatures led to quicker strength degradation. This temperature dependence of the material strength was modeled using an Arrhenius relationship, which allows for the prediction of estimated strengths at future times. Activation energies of 75.4 kJ·mol⁻¹ and 76.2 kJ·mol⁻¹ were found for the hoop tension and axial compression strength losses, respectively.

The hoop tension tests were performed on short annular specimens using a novel test fixture developed for this application, in which outward radial loading is achieved through the use of pressurized hydraulic fluid acting on a PTFE seal which transfers the load to the sample. This approach allows for a purely radial and uniform load to be applied to the sample, while maintaining “free-free” boundary conditions at the sample ends. The uniform load exerted on the sample using this fixture is also preferable to that applied using a standard split-D test, which has often been used to test tensile strength of annular specimens, and which results in bending stresses that are usually uncharacteristic of the loading that the material will see in operation.

The stiffness of the PTFE seal must be taken into account, and the load applied to the sample calculated based on the internal fluid pressure and the load carried by the seal. But this calculation is fairly straightforward. For this study, the load carried by the seal was found using two independent means: finite element analysis and mechanics of material / elasticity analysis. The results of the two analyses were very consistent with one another, lending credence to the results. After each test, the PTFE seals experienced an increase in their outer diameter. However, annealing at approximately 310°C for four hours eliminated this growth, and the seals generally returned to their original dimensions.

6. The Application of a Static-Fatigue-Based Model for Accelerated Aging of Glass Fiber Reinforced Composites

6.1. Introduction

Glass fiber reinforced composites are widely used in many demanding applications. Glass reinforced concrete (GRC) is used extensively in architectural applications, usually in cosmetic applications such as facades, but which nevertheless require a significant level of structural integrity and durability. Generally in the applications the material experiences static dead loads, with perhaps intermittent small dynamic mechanical loads. However, such materials are of a matter of course subjected to significant hygrothermal loads as they are often exposed to ambient weather conditions.

Glass reinforced polymer composites (GRP), on the other hand, are routinely used in naval and civil applications in which they carry very large dynamic active loads as well as static dead loads, and they, too, are often subjected to substantial hygrothermal conditions.

For both types of material, the hygrothermal and mechanical loadings are deleterious to the strength of the material; often these loads work synergistically toward an accelerated degradation of strength.

Designers of applications in which these materials are used face significant challenges in predicting the composite strength as a function of time and loading history. The complexity of the system, both in terms of geometrical complexity of the constituents and chemical complexity make life prediction and prognosis a difficult task, since the complexity has lead to a lack of effective mechanistic models. As a result, the most common way of handling the problem has been to collect large amounts of experimental data, using accelerated aging techniques to acquire the data in manageable amounts of time. While these approaches have certainly been helpful in both the worlds of GRC and GRP, most approaches have nevertheless been purely phenomenological techniques, in which no underlying cause of strength degradation is proposed. An early and definitive example of this approach was put forth for use in GRC applications by

Litherland and Proctor [76, 99], in which accelerated aging data from a laboratory and real-world data taken from around the world were analyzed using an Arrhenius approach in which residual material strength was plotted against $\log(\text{time})$. The Arrhenius relation allowed for the definition of a rate constant, which related strength loss rate at a given temperature to that at some known reference temperature condition.

As useful as these approaches have been, however, as Purnell et al. [100, 101] have pointed out, the form of the strength loss relationship is flawed, as it predicts infinite strength at $t=0$. While this is generally not an issue since material strengths near zero are not of interest (and known, besides), it nevertheless highlights the non-mechanistic basis of these approaches. Purnell [100, 101] has also pointed out that the rate parameters and acceleration factors that are derived from such an analysis are not generally applicable to other materials, since they are highly dependent on the ambient chemistry, which, for GRCs, is dependent on the matrix used in the composite.

Several years ago Purnell [101] proposed a modification of the Proctor method in which a mechanistic explanation is theorized for the strength degradation of GRCs under hygrothermal conditions. This model assumes that the GRC strength degradation is controlled by the mechanism of static fatigue, in which small surface flaws (cracks) on the glass fiber surface grow under hygrothermal and mechanical loading to lead to failure. Recently, Purnell, Lesko, and Cain [100] proposed the possibility of applying this model to GRPs and made a preliminary investigation into the efficacy of this approach with the analysis of a dataset of E-glass/vinyl-ester composites collected at Virginia Tech. In this analysis, activation energies were derived from an Arrhenius relationship and were compared to activation energies found by Purnell and other researchers investigating GRC, as well as several *ab initio* approaches by material scientists looking at silica glass in aqueous environments. The results obtained were far from conclusive, but hinted at the promise that perhaps, in many cases, strength degradation of glass-reinforced composites under hygrothermal loading was, in fact, controlled by static fatigue of the glass. As a result, a further literature review was initiated with the goal of collecting all available relevant GRP data and any new relevant GRC data. This chapter will describe the analysis of these data sets and will attempt to draw conclusions concerning the applicability of the Purnell model to GRP data, and concerning its underlying hypothesis of static fatigue-controlled strength loss.

6.2. The Static Fatigue Model of Glass Degradation in the Presence of Moisture

In practical, real-world settings, the strength of glass fibers is largely a function of surface flaws caused during the manufacture of the glass. It is not uncommon for these microscopic flaws to reduce the strength by half [102] over that which would be predicted for a “perfect” fiber. Purnell [103] has shown that this reduction in strength can result from flaws as shallow as 100 nm; given that their width would be much smaller than that these flaws are not often visualized through microscopy.

In 1965, Charles and Hillig [104] first suggested that these flaws might be susceptible to stress corrosion. They hypothesized that such stress corrosion might cause the stress concentration effect of the flaws to become greater, leading to crack growth rates that would be functions of temperature and the corrosive environment. Under a stress-free environment, they thought, the internal surface of the crack would be uniformly corroded, eventually leading to a blunting of the crack tip, and a cessation of further crack growth. However, under an applied stress in the glass fiber, the crack tip would corrode preferentially with respect to the rest of the crack face, causing the crack to sharpen and advance. This process would continue as long as the stress was applied, and given a high enough stress and sufficiently corrosive environment, lead to accelerating (unstable) crack growth and subsequent fiber failure. Studies have shown that there is a stress limit (for any given environment), below which the fiber’s strength does not degrade, and above which it does. As this is reminiscent of the fatigue limit that many materials show under cyclic loading, the degradation process is referred to as “static fatigue”, and the limiting stress the “static fatigue limit”.

This theory has been supported experimentally by Ritter et al. [105] who showed that the strength loss process was a function of the loading rate. That is, at slower loading rates, the strength loss is accelerated. Presumably at higher loading rates, the crack tip spends more time shielded from the environment due to its very small size initially.

The process of static fatigue can be characterized by the following, taken from [100]:

- spontaneous failure occurs at constant applied stress (rupture behavior),

- temperature dependence of rupture time at constant applied stress (higher temperature, shorter time to rupture),
- the rate of the process is dependent on the presence of moisture (or an alkaline environment).

6.3. The Purnell Model

In light of these shortcomings, in 2001, Purnell et al. [101] derived an expression for residual strength of glass-reinforced concrete composites as a function of time and temperature. It will be shown that this model may be applicable to GRPs, as well. This model assumed that:

1. the rate of flaw growth is approximately constant in time and its relation to temperature is of the form of an Arrhenius relation;
2. the fiber strength is a function of the flaw size and can be predicted by fracture mechanics ideas; that is, as in Equation 53:

$$\sigma_f = \frac{BK_{IC}}{\sqrt{a}} \quad (53)$$

where B is a constant and K_{IC} is the critical stress intensity factor for the glass;

3. and, that the strength of the composite is proportional to the strength of the fibers.

Based on the first assumption, Purnell et al. developed the following equation for the rate of flaw growth in glass-reinforced concrete composites, Equation 54:

$$a = k_c k_T C e^{-\frac{E}{RT}t} + a_0 \quad (54)$$

where a is the flaw size, k_C and k_T are rate parameters corresponding to the OH^- concentration of the pore solution and temperature, respectively, E is the Arrhenius activation energy, R is the universal gas constant, T is temperature, t is time, and a_0 is the initial flaw size.

Then from fracture mechanics and the second assumption, it is known that the strength of the fiber is given by Equation 55:

$$\sigma_f = \frac{K_{IC}}{1.12\sqrt{\pi a}} \quad (55)$$

where K_{IC} is the stress intensity factor.

The third assumption suggests that Equation 56 will predict the strength of the composite based on the strength of the fibers:

$$\sigma_c = \eta_o \eta_l V_f \sigma_f \quad (56)$$

where η_o and η_l are efficiency parameters for the fiber orientation and length, respectively, and V_f is the fiber volume fraction.

Combining Equations 53-56 results in Equation 57, an expression for the strength of the composite as a function of time:

$$\sigma_c = \frac{\eta_o \eta_l V_f K_{IC}}{1.12 \sqrt{\pi \left(k_c k_T C e^{-\frac{E}{RT}t} + a_0 \right)}} \quad (57)$$

The authors then normalize this strength by the original strength (found by solving Equation 20 for $t=0$) and arrive at Equation 58:

$$S = \frac{\sigma_c}{\sigma_{c,t=0}} = \frac{1}{\sqrt{1 + \frac{k_c k_T C e^{-\frac{E}{RT}t}}{a_0}}} \quad (58)$$

The various material constants and parameters can be combined into one fitting parameter and the whole expression simplified as Equation 59:

$$S = \frac{1}{\sqrt{1+kt}} \quad (59)$$

where k is now a curve fitting parameter that is a function of temperature, pH, fiber orientation and length, etc, and which has the form of Equation 60:

$$k = k_0 e^{-\frac{E}{RT}} \quad (60)$$

There is also a modified ‘nonlinear’ version of his model, shown in Equation 61:

$$S = \frac{1}{\sqrt{1+(kt)^n}} \quad (61)$$

where n is an additional curve fitting parameter.

Both versions of the model will be assessed in this chapter. The rate parameters k will be used to derive activation energies. Before reviewing the data sets, however, it is useful to look at other sources of activation energy values for the degradation of glass in water.

6.4. Previously reported activation energies for the strength degradation of glass-reinforced composites and the dissolution of silica glass

The large GRC data sets originally collected by Proctor resulted in reported activation energies of approximately 89-93 kJ mol⁻¹.

In the 2001 paper [101], Purnell et al. applied his model to a large dataset of approximately 1,100 GRC tests, some performed by Purnell and many taken from the literature including data from GRC made with matrices not investigated by Proctor. It was confirmed that different formulations lead to different activation energies, as expected. Values of k were found for each formulation and used to find activation energies using Arrhenius plots. Significantly, the paper also brought attention to the fact that at sufficiently high aging temperatures (for some materials as low as 65°C) it is possible that chemistries that would not normally be activated during normal

operating conditions may be activated during the accelerated aging, which effectively limits the degree of acceleration that can be applied.

In [100], Purnell et al. applied both his linear model and non-linear model to a large data set taken from the literature and from testing conducted at Virginia Tech. Most of the data were residual tension data taken from cross-ply E-glass/epoxy laminates. The samples were hygrothermally aged at several temperatures, from room temperature up to 80°C for almost 1,000 days. This dataset of approximately 400 specimens was comprised of three types of specimens: pre-cracked specimens loaded to 4,000 microstrain; uncracked specimens with no initial damage; and uncracked samples with their edges sealed with copper to prevent moisture ingress through the edges. The remainder of the samples came from a study (discussed in Chapter 5 of this dissertation) conducted at Virginia Tech [106] in which helically wound E-glass/epoxy tubes were hygrothermally aged in water at 30, 40, and 50°C. Axial and circumferential samples were cut from the tubes (before aging) and tested in tension and compression (axial) and a simulated internal pressure (circumferential). The remaining strength as a function of aging was recorded. Based on these data, Purnell et al. calculated activation energies in the range of 84-93 kJ/mol for the former set, and 74 kJ/mol for the latter set. However, the value of 74 kJ/mol has since been modified to a significantly lower value of approximately 42.8 kJ/mol with the analysis of subsequent additional data, as reported in Chapter 5. Furthermore, the very nonlinear nature of the Arrhenius plots for this material shown in Chapter 5 suggest that there is more than one degradation mechanism involved, and therefore, the Purnell static fatigue model is not considered appropriate for this data set.

Before that, there had not been many attempts to use the static fatigue model on glass-reinforced polymer composites, though Beddows et al. [107] made an attempt. In this paper, Beddows calculated an activation energy of approximately 51 kJ mol⁻¹, though the data set was rather small. Purnell [100] has calculated that the data collected by Helbling [108] can be reevaluated using the static fatigue model with results showing activation energies on the order of 60-90 kJ mol⁻¹.

Several researchers have looked at the process of glass hydrolysis on the atomic scale using *ab initio* quantum mechanical calculations. In these calculations, the area of interest (in this case the region surrounding the tip of a crack in silica glass) is modeled numerically. Generally, only

a very localized region is considered due to the computational power required to perform larger simulations. Often, on the order of 100 atoms are modeled. There are several sets of assumptions and approximations that can be made to simplify the models at the cost of accuracy. But all of these models attempt to predict chemical and mechanical behavior at the nanoscale by modeling atomic interactions.

West et al. [109-111] investigated the fracture of strained silica glass exposed to a water environment. Their work was based on the Michalske-Bunker [112] (MB) model of silica fracture in water, which includes the effect of strain on the reaction. Specifically, the MB model predicts that for a silica ring under strain, the O-Si-O bond angle will decrease (pinch) and form a “kink”, defined as a bond whose reaction rate is greatly increased due to its strained condition. Thus the strain, and the resulting kink, decreases the activation energy of a hydrolysis reaction at this site (see Figure 46). They used the Austin Method [113] (AM1) to model the hydrolysis and subsequent Si-O bond breaking in 3- and 4-member rings, as well as a 5-member ring-chain structure and found that hydrolysis of the strained 3-member rings is exothermic, that is spontaneous, while the strained 4-member rings and 5-member ring-chain structures are hydrolyzed with barriers of 92.0 and 94.6 kJ mol⁻¹, respectively. Figure 47 shows the reaction path for a five-fold Si-O ring exposed to water, in which the water spontaneously bonds to the silica structure, resulting in a penta-coordinated silicon atom. At this point, given sufficient energy to pass the barrier of 94.6 kJ mol⁻¹, the Si-O bond is broken. As will be seen in the following section, the similarity between this activation energy and those found in some data sets of moisture-induced composite degradation suggest that this hydrolysis reaction may be the controlling degradation mechanism.

Walsh et al. [114] investigated the activation barriers for the hydrolysis of amorphous silica surfaces using *ab initio* quantum mechanics calculations, as well. These calculations were performed using cluster models in which a small portion of the extended silica surface was modeled to include one of four common defect sites. They found that according to their models, the lowest barrier (of several possible reaction paths) for hydrolysis of a defect pair embedded in a 3-member ring was 86.9 kJ mol⁻¹.

6.5. Review of the sources of the data sets to be analyzed

This chapter will discuss the fitting of the Purnell model to three datasets, each with subsets comprising different test methods. Two of these sets have been fit with the linear Purnell model. However, the author is not aware of their having been fit with the nonlinear version, and so for completeness the data will be refit with both the linear and nonlinear models and the results compared. The reason for this will be seen when the GRP results are reported and clear differences in the two results are revealed.

The first GRC data set, and by far the most extensive, has been fit using the model by Purnell [115] using the linear (original) version of his model. In this chapter, however, both the linear and nonlinear models will be fit to the data. This data set was collected by Litherland [76] in 1981 and was described in a previous section of this chapter. The data set consisted of two types of tests: strand-in-cement (SIC) and composite samples. Each subset will be analyzed separately in this chapter. The fibers were first generation alkali-resistant fibers and the matrix was standard ordinary Portland cement (OPC).

The second GRC data set was collected by Orlowsky [116], and consists of three subsets. The first involves SIC tests run using Type A concrete (pH~13.5; see [116] for a full description of the concrete parameters.) The second utilized TSP tests (composite “T-bone” specimens), again with Type A concrete. The third and final subset involved SIC tests again, but with Type C concrete (pH~11; see [116].)

The final GRC data set was collected by Purnell himself, and has, of course been analyzed using the original, linear model. The author, however, is unaware that the data has been fit using the nonlinear model, so it will be refit using both versions of the model.

The number of available useful GRP datasets in the literature is very small. This chapter will discuss virtually all sets that were found by the author. Purnell et al. [100] have previously analyzed two sets of GRP data, both collected Virginia Tech. The smaller of the two is that data reported in Chapter 5 of this dissertation.

Three additional GRP data sets were found in the literature. The first was collected by Helbling [117] and involves unidirectional pultruded E-glass/vinyl-ester composites subject to tension

loads. The samples were subjected to hygrothermal conditioning while being held in bending at 0, 30, and 45% of the tension failure strain.

The second GRP set was collected by Karbhari-Zhang [57]. The material was VARTMed E-glass/vinyl-ester composite, subjected to tension. Uniirectional [0], bidirectional [0/90], and tri-directional [0/45/-45] materials were used in both 2-layer and 4-layer configurations, each.

The third and final data set was collected by Chu/Karbhari [118] and used pultruded E-glass/vinyl-ester composites and consists of two subsets: one subset was tested immediately after removal from immersion, and the second was allowed to “recondition” for an extended period of time in 46%RH air.

6.6. Results

The data sets discussed in this section are comprised of various materials and testing and conditioning methods. Therefore, for simplicity, the designations listed in Table 16 will be used as shorthand for the various datasets.

In order to fit the models to the data, for each subset the ‘error’ between model and experimental data was minimized using a least-squares fitting algorithm in commercial spreadsheet software. For the linear model, the rate parameter k was the fitting parameter. For the nonlinear model, both k and n were solved for. Once the values of k were determined, an Arrhenius plot was generated in order to 1) assess the linearity of the $1/T$ vs $\ln k$ relationship, and 2) to determine an activation energy from the slope of the line (multiplied by the gas constant, R .) Figure 48 is an example, taken from the PP_comp data set. A similar procedure was used on all data sets, and the results are presented in Table 17, at the end of this chapter.

The results of Table 17 demonstrate a significant difference in the modeled activation energies for glass-reinforced concrete compared to glass-reinforced polymer composites. In general, the GRPs show markedly lower activation energies, at least when using the linear model, while the nonlinear model often gives quite high values. This discrepancy in the results is difficult to explain, since Purnell has seen very good consistency in the past [100].

In general, the modeling of the GRCs shows fairly consistent results for linear and nonlinear models, the exceptions being Orłowsky's OJ_SIC_A and OJ_TSP_A beton-A matrix tests. Furthermore, the GRC values tend to be more consistent with previous values found by Purnell and are not inconsistent with activation energies calculated by material scientists using *ab initio* methods (see supplementary next section.)

Figure 49 gives typical life curves from the model and the data to which they were fit. This fit is typical of the data sets reviewed in this chapter.

6.7. Conclusions

The results of the literature review and metastudy indicate that the Purnell model is effective when used as a fitting model for glass-reinforced composites. It is able to model most glass-degradation data reviewed here without difficulty. Furthermore, when used on the GRC data, it returns predicted degradation activation energies in the range of approximately 75-110 kJ/mol. These values are not inconsistent with those predicted by *ab initio* calculations performed by researchers investigating the dissolution of silica glass through ring-opening mechanisms, where activation energies of approximately 85-95 kJ/mol were predicted. This similarity in activation energies is evidence in support of the hypothesis (inherent in the Purnell model) that static fatigue is the primary cause of strength degradation of hygrothermally-aged glass-reinforced composites.

When used on GRP data, however, the model in its current form returns inconsistent values between the linear and nonlinear models, and neither matches extremely well with values from other sources. However, the available GRP database is very small, and so it may be that the application of the model to GRP may be appropriate in many cases.

Purnell is currently developing alternative forms of the basic model, and early results suggest that these other, more sophisticated forms provide much better and more consistent results for the limited GRP data set reviewed here.

6.8. Tables and Figures

Table 16: Data set designations for GRC and GRP data sets.

Source	Description	Subset differentiation	Designation
[117]	Unidirectional pultruded E-glass/VE. Sustained bending load during conditioning.	0% strain	HK-0
		30% of ultimate strain	HK-30
		45% of ultimate strain	HK-45
[57]	VARTM E-glass/VE, uni-, bi-, and tri-directional.	None*	KZ
[118]	Pultruded E-glass/VE	Conditioned	CK-C
		Re-conditioned	CK-RC
[76]	1st gen AR fibers, OPC	Composite	Lith_comp
		SIC	Lith_SIC
[116]	SIC tests, beton-A	-	OJ_SIC_A
	TSP beton-A	-	OJ_TSP_A
	SIC beton-C		OJ_SIC_C
[103]	OPC/glass fiber composite	1 st gen AR fibers	PP_COMP1
		2 nd gen AR fibers	PP_COMP2

*Model failed to converge. Details withheld for simplicity.

Table 17: Model fit results for all data sets.

Designation	E_a (linear) (kJ/mol)	E_a (nonlinear) (kJ/mol)	R² value of Arrhenius. Fit (linear)	R² value of Arrhenius. Fit (nonlinear)
HK-0	53.8	128.8	0.9989	0.9314
HK-30	56.2	121.8	0.9999	0.954
HK-45	73.4	148.5	0.9987	0.9121
KZ	*	*	*	*
CK-C	41.4	50.8	0.9783	0.9858
CK-RC	47.2	59.2	0.989	0.9961
Lith_comp	100.0	97.0	0.9913	0.9966
Lith_SIC	88.4	92.5	0.9986	0.9955
OJ_SIC_A	75.3	187.6	0.9949	0.9434
OJ_TSP_A	87.9	109.3	0.9591	0.8946
OJ_SIC_C	63.2	57.5	0.9993	0.9993
PP_COMP1	76.0	86.5	0.9845	0.9140
PP_COMP2	101.3	104.6	0.9978	0.9984

*Model failed to converge. No results reported.

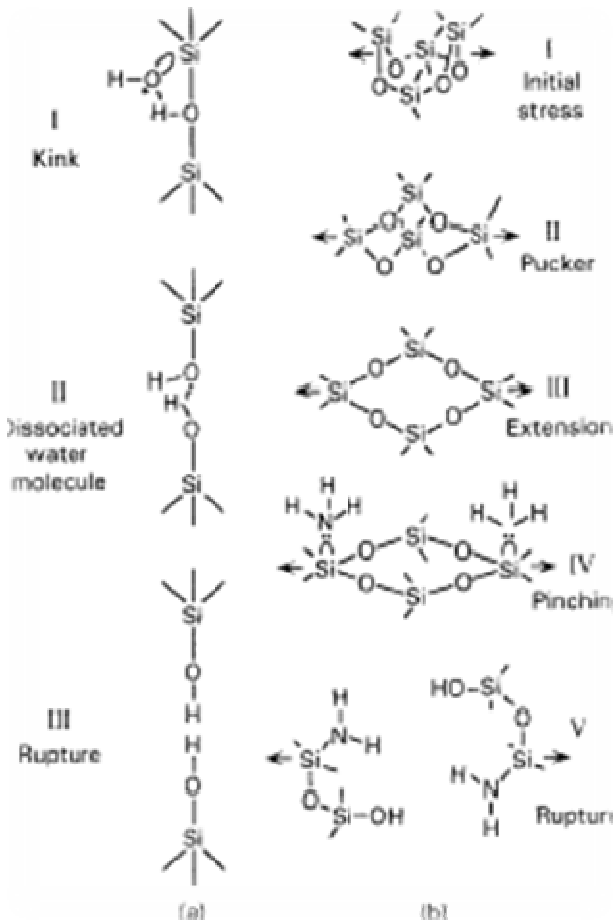


Figure 46: Reaction steps in environmentally enhanced fracture of vitreous silica in (a) the Michalske-Freiman model and (b) the Michalske-Bunker model. (Excerpted from West and Hench [109]).

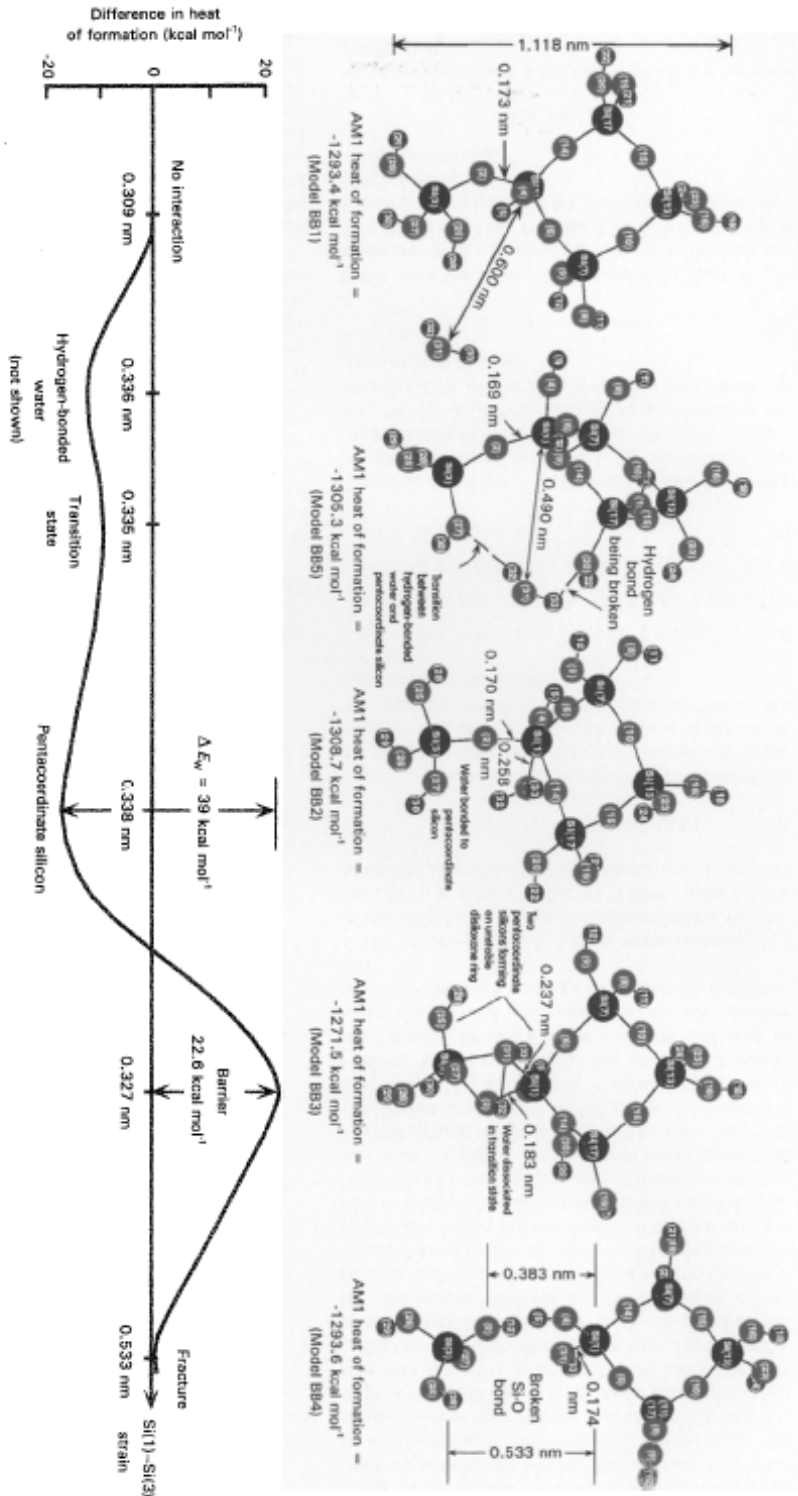


Figure 47: The reaction path for the Si-O bond fracture with the interaction of water with the five-fold ring-chain structure. (Excerpted from West and Hensch [109]).

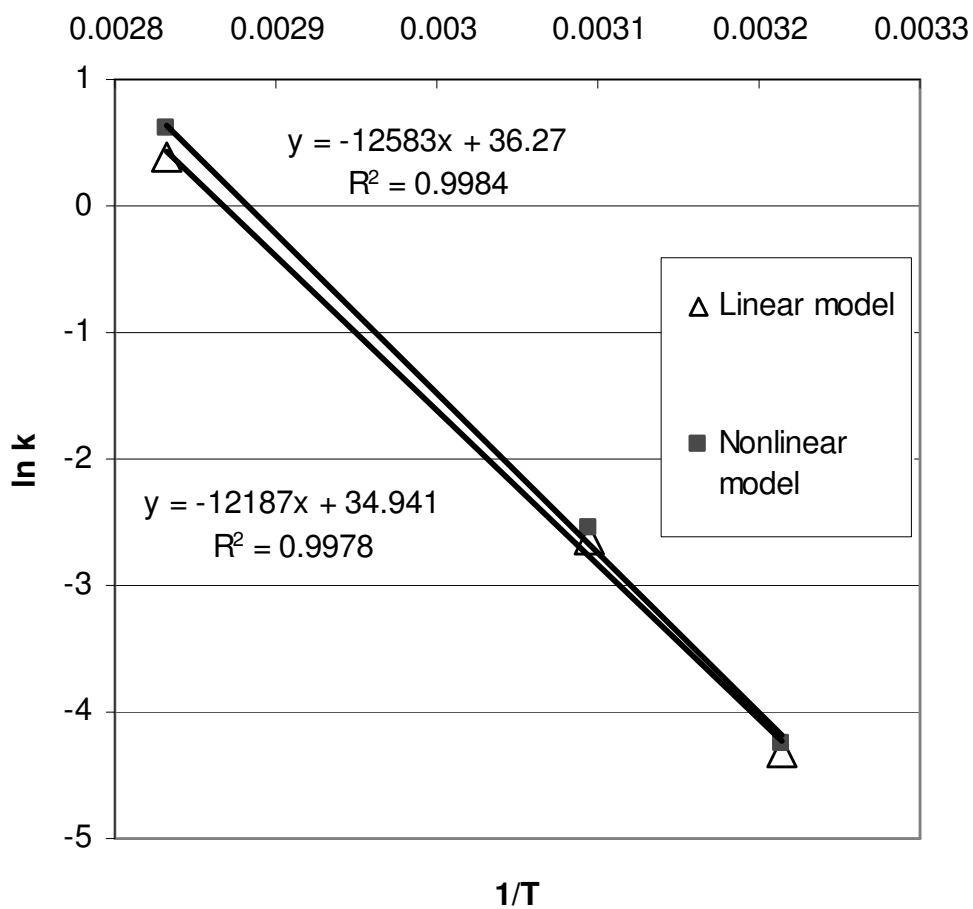


Figure 48: Arrhenius plot for PP_comp_OPCI data set showing the fits for the linear and nonlinear models. The slopes of the lines represent the activation energy divided by the gas constant, R.

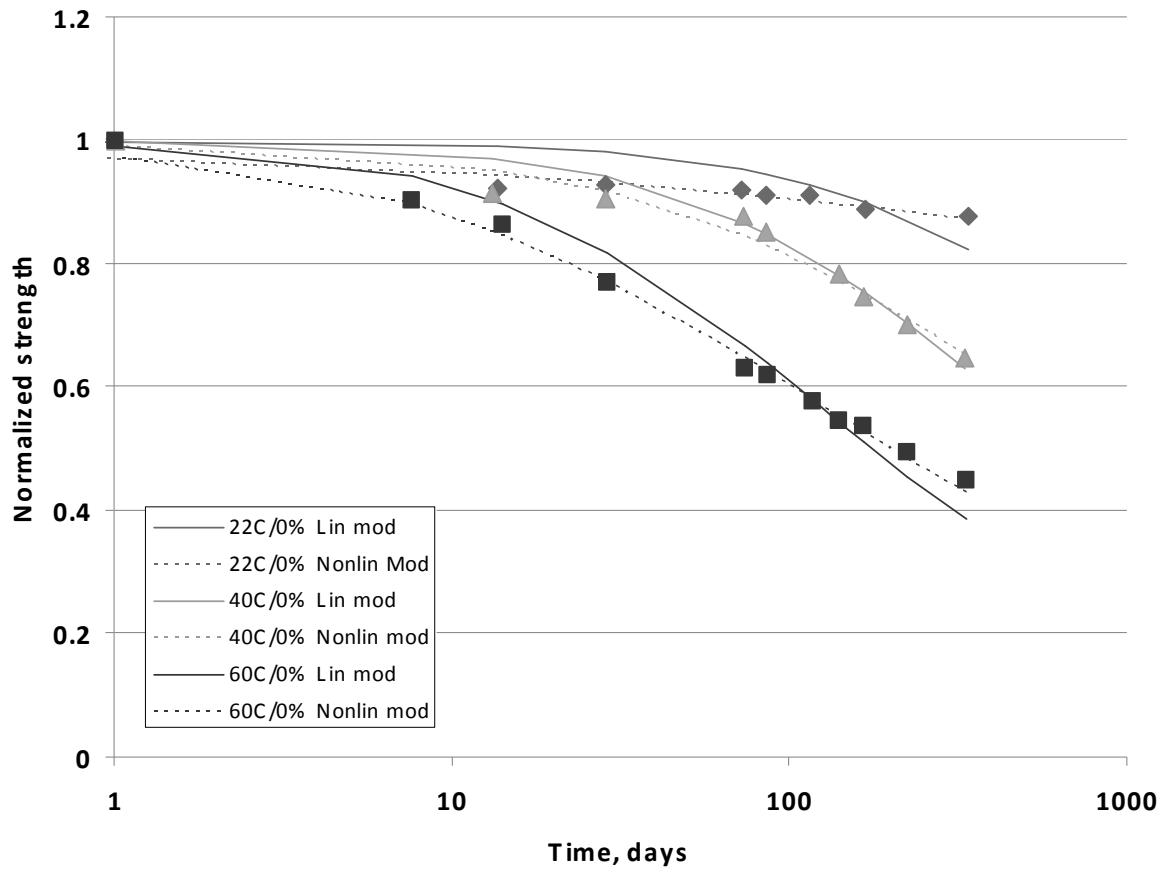


Figure 49: The Purnell model [101] fit to strength data, taken from HK-0 data set

7. Conclusions

This dissertation has discussed a number of topics related to the long-term durability of glass-reinforced composites.

The first portion of the document described work that was done to assess the effect that post-curing has on widely used E-glass/vinyl-ester composites. This study was designed to determine how a correct post-cure can not only enhance the composite material properties, but can stabilize them by progressing the cure to a meta-stable degree. As such, the recommendations that came from the study became the default processing parameters for materials made in the Materials Response Group at Virginia Tech. By stopping or nearly stopping material property evolution due to matrix curing over time, the post-cure regime isolated and allowed the study of other time-dependent effects, such as hygrothermal degradation, as well as helping to ensure that test materials will not significantly change with time.

The second portion of this paper discussed the effect that mean stress and R-ratio have on the fatigue performance of the same material. Qualitative and quantitative differences were seen in the performance as a function of the loading ratio. A fatigue life prediction model developed at Virginia Tech was applied to the fatigue data, characterizing the material in constant-amplitude loading. The parameters that came from that fit were then used along with the model to predict variable-amplitude fatigue lives, with remarkably good results.

The final portion of the dissertation concerned the effect of hygrothermal and accelerated aging on glass-reinforced composites. A meta-study was performed on data from the literature, and a model put forth by Purnell was applied to the data. It was seen that the model can predict activation energies associated with glass-reinforced composite strength degradation in the case of glass-reinforced concrete. For glass-reinforced polymer composites the results were less promising. However, the available GRP data sets were generally small, and there may be hope yet that the model will find success in the GRP regime when more comprehensive data becomes available in the literature.

8. Bibliography

1. Venditti, R.A. and J.K. Gillham, *Anomalous behavior of thermosetting systems after cure vs. chemical conversion: a normalized conversion-temperature-property diagram*. Journal of Applied Polymer Science, 1995. **56**(13): p. 1687-1705.
2. Venditti, R.A. and J.K. Gillham, *Relationship between the glass transition temperature (T_g) and fractional conversion for thermosetting systems*. Journal of Applied Polymer Science, 1997. **64**(1): p. 3-14.
3. Wisanrakkit, G. and J.K. Gillham, *Glass transition temperature (T_g) as an index of chemical conversion for a high- T_g amine/epoxy systems Chemical and diffusion-controlled reaction kinetics*. Journal of Applied Polymer Science, 1990. **41**(11-12): p. 2885-2929.
4. Chang, S.S., *Effect of Curing History on Ultimate Glass Transition Temperature and Network Structure of Crosslinking Polymers*, in *Reprint: Effect of Curing History on Ultimate Glass Transition Temperature and Network Structure of Crosslinking Polymers*. 1992: United States. p. 11p.
5. Couchman, P.R. and F.E. Karasz, *Macromolecules*, 1978. **11**(117).
6. DiBenedetto, A.T., *Prediction of the glass transition temperature of polymers: a model based on the principle of corresponding states*. Journal of Polymer Science, Part B (Polymer Physics), 1987. **25**(9): p. 1949-69.
7. Pascault, J.P. and R.J.J. Williams, *Glass transition temperature versus conversion relationships for thermosetting polymers*. Journal of Polymer Science, Part B (Polymer Physics), 1990. **28**(1): p. 85-95.
8. Verghese, N., D. Potts, and A. Shafi, in *COMPOSITES 2003 Convention and Trade Show Composites Fabricators Association 2003*.
9. Hale, A., C.W. Macosko, and H.E. Bair, *Glass transition temperature as a function of conversion in thermosetting polymers*. *Macromolecules*, 1991. **24**(9): p. 2610-2621.
10. Li, H., et al., *Network structure and properties of dimethacrylate-styrene matrix materials*. Journal of Composite Materials, 2000. **34**(18): p. 1512-1528.
11. Ziaee, S. and G.R. Palmese, *Effects of temperature on cure kinetics and mechanical properties of vinyl-ester resins*. Journal of Polymer Science, Part B: Polymer Physics, 1999. **37**(7): p. 725-744.
12. Bradley, S.W., et al., *Viscoelastic creep characteristics of neat thermosets and thermosets reinforced with E-glass*. Journal of Composites Technology & Research, 1998. **20**(1): p. 51-58.

13. Cain, J.J., et al., *Post-curing effects on marine VARTM FRP composite material properties for test and implementation*. Transactions of the ASME. Journal of Engineering Materials and Technology, 2006. **128**(1): p. 34-40.
14. Cvetanovska, A. and P. Compston, *Degree of cure and tensile properties of vinylester resin cured with ultraviolet light*. Journal of Materials Science, 2004. **39**(5): p. 1791-3.
15. He, Y., Y. Zhong, and J. Zhou. *Post-curing effects on physical and mechanical properties of IM7/5250-4 composites*. 1998. San Antonio, TX, USA: SAMPE, Covina, CA, USA.
16. Ota, T., T. Matsuoka, and K. Sakaguchi, *Effect of post-cure time on mechanical properties of plain-woven glass fabric composites*. Journal of the Society of Materials Science, Japan, 2006. **55**(10): p. 958-64.
17. Tucker, R., P. Compston, and P.Y.B. Jar, *The effect of post-cure duration on the mode I interlaminar fracture toughness of glass-fibre reinforced vinylester*. Composites Part A (Applied Science and Manufacturing), 2001. **32A**(1): p. 129-34.
18. Miner, M.A., *Cumulative damage in fatigue*. Journal of Applied Mechanics, 1945. **12**: p. A159-A164.
19. Palmgren, A., *The life of ball bearings Die Lebensdauer von Kugellagern*. Zeitschrift des Vereines Deutscher Ingenieure, 1924. **68**(14): p. 339-341.
20. Broutman, J. and S. Sahu. *A new theory to predict cumulative fatigue damage in fiberglass reinforced plastics*. in *Composite materials: Testing and design, ASTM STP 497*, ASTM. 1972. West Conshohocken, Pa.,.
21. Adam, T., et al., *Life prediction for fatigue of T800/5245 carbon-fibre composites: II. Variable-amplitude loading*. International Journal of Fatigue, 1994. **16**(8): p. 533-47.
22. Post, N.L., et al., *Residual strength prediction of composite materials: Random spectrum loading*. . Engineering Fracture Mechanics, 2007. **Accepted for publication**.
23. Poursartip, A., M.F. Ashby, and P.W.R. Beaumont, *Fatigue Damage Mechanics of a Carbon-Fibre Composite Laminate: I - Development of the Model*. Composites Science and Technology, 1986. **25**(3): p. 193-218.
24. Poursartip, A. and P.W.R. Beaumont, *Fatigue Damage Mechanics of Carbon-Fibre Composite Laminate: II - Life Prediction*. Composites Science and Technology, 1986. **25**(4): p. 283-299.
25. Schaff, J.R. and B.D. Davidson, *Life prediction methodology for composite structures. II. Spectrum fatigue*. Journal of Composite Materials, 1997. **31**(2): p. 158-81.
26. Schaff, J.R. and B.D. Davidson, *Life prediction methodology for composite structures. Part I-constant amplitude and two-stress level fatigue*. Journal of Composite Materials, 1997. **31**(2): p. 128-157.

27. Kedward, K.T. and P.W.R. Beaumont, *The treatment of fatigue and damage accumulation in composite design*. International Journal of Fatigue, 1992. **14**(5): p. 283-94.
28. van Paepegem, W. and J. Degrieck, *Simulating in-plane fatigue damage in woven glass fibre-reinforced composites subject to fully reversed cyclic loading*. Fatigue and Fracture of Engineering Material and Structures, 2004. **27**(12): p. 1197-208.
29. Van Paepegem, W., J. Degrieck, and P. De Baets, *Finite element approach for modelling fatigue damage in fibre-reinforced composite materials*. Composites Part B:Engineering, 2001. **32**(7): p. 575-588.
30. Yang, J.N., S.H. Yang, and D.L. Jones, *Stiffness-based statistical model for predicting the fatigue life of graphite/epoxy laminates*. Journal of Composites Technology & Research, 1989. **11**(4): p. 129-134.
31. Yang, J.N., et al., *A stiffness degradation model for graphite/epoxy laminates*. Journal of Composite Materials, 1990. **24**(7): p. 753-69.
32. Post, N.L., *Modeling the residual strength distribution of structural gfrp composite materials subjected to constant and variable amplitude tension-tension fatigue loading*. 2005, Virginia Polytechnic Institute and State University.
33. Diao, X.X. and X.S. Xing, *Statistical fatigue damage analysis of unidirectional composites*. Theoretical and Applied Fracture Mechanics, 1995. **22**(1): p. 29-34.
34. Osiroff, R. and W.W. Stinchcomb. *Dynamic mechanical analysis as a complementary damage characterization technique for composite materials*. 1992. San Antonio, TX, USA: Publ by ASTM, Philadelphia, PA, USA.
35. Kortschot, M.T., et al., *Crack Advancement in a Carbon Fibre-Epoxy Composite Observed by Dynamic Scanning Microscopy*. 1987. p. 9.
36. Doucet, A.B. and J. Qin, *Microstructural analysis of impact damage in two glass/epoxy composite laminates*. Composites Engineering, 1992. **3**(1): p. 55-68.
37. Scida, D., Z. Aboura, and M.L. Benzeggagh. *The effect of ageing on the damage events in woven-fibre composite materials under different loading conditions*. 2002. Cachan, France: Elsevier.
38. Barchan, A., *The analysis of fatigue damage to glass-fiber reinforced composites*. Materials Science, 2001. **37**(6): p. 918-27.
39. Degrieck, J. and W. Paepegem, *Fatigue damage modeling of fibre-reinforced composite materials: Review*. Applied Mechanics Review, 2001. **54**(4): p. 279-300.
40. Chou, P.C. and R. Croman, *Residual strength in fatigue based on the strength-life equal rank assumption*. Journal of Composite Materials, 1978. **12**: p. 177-94.

41. Yang, J.N. and M.D. Liu, *Residual strength degradation model and theory of periodic proof tests for graphite/epoxy laminates*. Journal of Composite Materials, 1977. **11**: p. 176-203.
42. Schultz, D. and J.J. Gerharz, *Fatigue strength of a fibre-reinforced material*. Composites, 1977. **10**: p. 245-250.
43. Reifsnider, K.L. and S.W. Case, *Damage Tolerance and Durability in Material Systems*. 2002, New York: John Wiley & Sons.
44. Weibull, W., *Statistical theory of strength of materials*. Ingeniors Vetenskaps Akademien -- Handlingar, 1939(151): p. 45.
45. El Kadi, H. and F. Ellyin, *Effect of stress ratio on the fatigue of unidirectional glass fibre/epoxy composite laminae*. Composites, 1994. **25**(10): p. 917-24.
46. Al-Assaf, Y. and H. El Kadi, *Fatigue life prediction of unidirectional glass fiber/epoxy composite laminae using neural networks*. Composite Structures, 2001. **53**(1): p. 65-71.
47. Vassilopoulos, A.P., E.F. Georgopoulos, and V. Dionysopoulos, *Modelling fatigue life of multidirectional GFRP laminates under constant amplitude loading with artificial neural networks*. Advanced Composites Letters, 2006. **15**(2): p. 43-51.
48. Epaarachchi, J.A. and P.D. Clausen, *An empirical model for fatigue behavior prediction of glass fibre-reinforced plastic composites for various stress ratios and test frequencies*. Composites Part A (Applied Science and Manufacturing), 2003. **34A**(4): p. 313-26.
49. Sendekyj, G.P., ed. *Life prediction for resin matrix composite materials*. Fatigue of composite materials, ed. K.L. Reifsnider. 1990, Elsevier: Amsterdam.
50. Conle, A. and J.P. Ingall, *Effects of Mean Stress on the Fatigue of Composite Materials*. Journal of Composites Technology & Research, 1985. **7**(1): p. 3-11.
51. Rotem, A., *The fatigue behavior of composite laminates under various mean stresses*. Composite Structures, 1991. **17**(2): p. 113-26.
52. Sutherland, H.J. and J.F. Mandell, *Effect of mean stress on the damage of wind turbine blades*. Journal of Solar Energy Engineering, Transactions of the ASME, 2004. **126**(4): p. 1041-1049.
53. Sutherland, H.J. and J.F. Mandell, *The effect of mean stress on damage predictions for spectral loading of fibreglass composite coupons*. Wind Energy, 2005. **8**(1): p. 93-108.
54. Mandell, J.F. and D.D. Samborsky, *DOE/MSU Composite Material Fatigue Database: Test Methods, Materials, and Analysis, SAND97-3002* 1997, Sandia National Labs, Albuquerque, NM.

55. Cain, J., et al., *R-ratio Effects on Glass-reinforced Polymer Composite Life and Remaining Strength*, in *International Conference on Composite Materials*. 2007: Kyoto, Japan.
56. Akay, M., *Moisture absorption and its influence on the tensile properties of glass-fibre reinforced polyamide 6,6*. *Polymers & Polymer Composites*, 1994. **2**(6): p. 349-354.
57. Karbhari, V.M. and S. Zhang, *E-glass/vinylester composites in aqueous environments - I: Experimental results*. *Applied Composite Materials*, 2003. **10**(1): p. 19-48.
58. Kasturiarachchi, K.A. and G. Pritchard, *Water absorption of glass/epoxy laminates under bending stresses*. *Composites*, 1983. **14**(3): p. 244-250.
59. Loos, A.C., et al., *Moisture absorption of polyester-E glass composites*. *Journal of Composite Materials*, 1980. **14**: p. 142-54.
60. Perreux, D. and C. Suri, *A study of the coupling between the phenomena of water absorption and damage in glass/epoxy composite pipes*. *Composites Science and Technology*, 1997. **57**(9-10): p. 1403-1413.
61. Srihari, S., A. Revathi, and R.M.V.G.K. Rao, *Hygrothermal effects on RT-cured glass-epoxy composites in immersion environments. I. Moisture absorption characteristics*. *Journal of Reinforced Plastics and Composites*, 2002. **21**(11): p. 983-91.
62. Boukhoulda, B.F., E. Adda-Bedia, and K. Madani, *The effect of fiber orientation angle in composite materials on moisture absorption and material degradation after hygrothermal ageing*. *Composite Structures*, 2006. **74**(4): p. 406-18.
63. Fick, A., *Philosophical Magazine*, 1855. **10**(30).
64. Lundgren, J.-E. and P. Gudmundson, *Moisture absorption in glass-fibre/epoxy laminates with transverse matrix cracks*. *Composites Science and Technology*, 1999. **59**(13): p. 1983-1991.
65. Schutte, C.L., *Environmental durability of glass-fiber composites*. *Materials Science and Engineering: R: Reports*, 1994. **13**(7): p. 265-323.
66. Karbhari, V.M., et al., *Issues of variability and durability under synergistic exposure conditions related to advanced polymer composites in the civil infrastructure*. *Composites Part A (Applied Science and Manufacturing)*, 2006. **37**(8): p. 1102-10.
67. Ellyin, F., *The Influence of Aqueous Environment, Temperature and Cyclic Loading on Glass-Fibre/Epoxy Composite Laminates*. *Journal of Reinforced Plastics and Composites*, 2003. **22**(7): p. 615-636.
68. Ellyin, F. and R. Maser, *Environmental effects on the mechanical properties of glass-fiber epoxy composite tubular specimens*. *Composites Science and Technology*, 2004. **64**(12): p. 1863-1874.

69. Chiou, P.L. and W.L. Bradley, *Moisture-induced degradation of glass/epoxy filament-wound composite tubes*. Journal of Thermoplastic Composite Materials, 1996. **9**(2): p. 118-128.
70. Chiou, P.-L. and W.L. Bradley, *Seawater effects on strength and durability of glass/epoxy filament-wound tubes as revealed by acoustic emission analysis*. Journal of Composites Technology & Research, 1997. **19**(4): p. 214-221.
71. Post, N.L., et al., *The Effective Use of Material Knockdowns for the Modeling of Saturated Glass/Vinyl-ester Composites Subject to Fatigue Loading*, in *Technical Report to Naval Surface Warfare Center, Carderock Division*. 2006, Virginia Tech.
72. Liao, K., C.R. Schultheisz, and D.L. Hunston, *Long-term environmental fatigue of pultruded glass-fiber-reinforced composites under flexural loading*. International Journal of Fatigue, 1999. **21**(5): p. 485-495.
73. Bank, L.C., et al. *A model specification for frp composites for civil engineering structures*, in *FRP Composites in Engineering*. in *International Conference for FRP Composites in Civil Engineering*. 2001. Hong Kong: Elsevier.
74. Khennane, A. and R.E. Melchers, *A micromechanics model for environmental stress corrosion in GFRP*. International Journal of Materials & Product Technology, 2003. **19**(1-2): p. 2-14.
75. Chin, J.W., W.L. Hughes, and A. Signor. *Elevated temperature aging of glass fiber reinforced vinyl ester and isophthalic polyester composites in water, salt water and concrete pore solution*. in *American Society of Composites 16th Technical Conference*. 2001.
76. Litherland, K.L., D.R. Oakley, and B.A. Proctor, *Use of Accelerated Ageing Procedures to Predict the Long Term Strength of GRC Composites*. Cement and Concrete Research, 1981. **11**(3): p. 455-456.
77. Iskander, M.G. and M. Hassan, *Accelerated degradation of recycled plastic piling in aggressive soils*. Journal of Composites for Construction, 2001. **5**(3): p. 179-187.
78. Nkurunziza, G., et al., *Durability of GFRP bars: A critical review of the literature*. Progress in Structural Engineering and Materials, 2005. **7**(4): p. 194-209.
79. Vijay, P.V. and H.V.S. GangaRao. *Accelerated and natural weathering of glass fibre reinforced plastic bars*. in *4th International Conference on Fibre-Reinforced Plastics for Reinforced Concrete Structures (FRPRCS-4)*. 1999. Baltimore, MD.
80. Purnell, P., *Interpretation of climatic temperature variations for accelerated ageing models*. Journal of Materials Science, 2004. **39**(1): p. 113-118.
81. Muraoka, M., K. Ebata, and H. Abe, *Effect of Humidity on Small-Crack Growth in Silica Optical Fibers*. Journal of the American Ceramic Society, 1993. **76**(6): p. 1545-1550.

82. Ritter Jr, J.E., J.M. Sullivan, and K. Jakus, *Dependency of fatigue predictions on the form of the crack velocity equation*. Journal of the American Ceramic Society, 1981. **64**(6): p. 372-4.
83. Cain, J.J., et al., *Post-curing effects on marine VARTM FRP composite material properties for test and implementation*. Journal of Engineering Materials and Technology-Transactions of the Asme, 2006. **128**(1): p. 34-40.
84. Mandell, J.F., et al., *New fatigue data for wind turbine blade materials*. Journal of Solar Energy Engineering, Transactions of the ASME, 2003. **125**(4): p. 506-514.
85. Reifsnider, K.L. and W.W. Stinchcomb. *Critical-Element Model of the Residual Strength and Life of Fatigue-Loaded Composite Coupons*. 1986. Dallas, TX, USA: ASTM, Philadelphia, PA, USA.
86. Reifsnider, K., S. Case, and J. Duthoit, *Mechanics of composite strength evolution*. Composites Science and Technology, 2000. **60**(12-13): p. 2539-2546.
87. Fam, A., and Rizkalla, S., *Behavior of Axially Loaded Concrete-Filled Circular Fiber-Reinforced Polymer Tubes*. ACI Structural Journal, 2001. **98**(3): p. 280-289.
88. Fam, A., *Concrete-Filled Fibre-Reinforced Polymer Tubes for Axial and Flexural Structural Members*. 2000, University of Manitoba, Canada.
89. Fam, A.Z. and S.H. Rizkalla, *Flexural Behavior of Concrete-Filled Fiber-Reinforced Polymer Circular Tubes*. Journal of Composites for Construction, 2002. **6**(2): p. 123-132.
90. Iskander, M.G. and M. Hassan, *State of the Practice Review in FRP Composite Piling*. Journal of Composites for Construction, 1998. **2**(3): p. 116-120.
91. Mirmiran, A., *Innovative Combinations of FRP and Traditional Materials (Invited Paper)*, in *International Conference on FRP Composites in Civil Engineering*. 2001, Elsevier Science Ltd: Hong Kong, China.
92. Mirmiran, A. and M. Shahawy, *Behavior of Concrete Columns Confined by Fiber Composites*. Journal of Structural Engineering, 1997. **123**(5): p. 583-590.
93. Mirmiran, A., M. Shahawy, and M. Samaan, *Strength and Ductility of Hybrid FRP-Concrete Beam-Columns*. Journal of Structural Engineering, 1999. **125**(10): p. 1085-1093.
94. Pando, M.A., Filz, G. M., Lesko, J. J., Ealy, C. E. , , *A Laboratory and Field Study of Composite Piles for Bridge Substructures*, Federal Highway Administration Research Report.
95. Bank, L.C., et al., *A model specification for FRP composites for civil engineering structures*. Construction and Building Materials, 2003. **17**(6-7): p. 405-437.

96. Chin JW, H.W., Signor A. *Elevated temperature aging of glass fiber reinforced vinyl ester and isophthalic polyester composites in water, salt water and concrete pore solution.* in *The American Society for Composites, 16th Technical Conference Proceedings*. 2001.
97. *Apparent Tensile Strength of Ring or Tubular Plastics and Reinforced Plastics by Split Disk Method. (ASTM Standard)*. 1992: United States. p. 6p.
98. Knight, C.E., Jr., *Failure Analysis of the Split-D Test Method*. ASTM Special Technical Publication, 1977(617): p. 201-214.
99. Proctor, B.A., D.R. Oakley, and K.L. Litherland, *Developments in the Assessment and Performance of GRC Over 10 Years*. *Composites*, 1982. **13**(2): p. 173-179.
100. Purnell, P., J. Lesko, and J. Cain, *Accelerated ageing rationales for GRC and their application to GRP*, in *DURCOSYS*. 2005: Virginia Tech, Blacksburg, VA.
101. Purnell, P., N.R. Short, and C.L. Page, *A static fatigue model for the durability of glass fibre reinforced cement*. *Journal of Materials Science*, 2001. **36**: p. 5385-5390.
102. Majumdar, A.J. and V. Laws, *Glass fibre reinforced cement*. 1991, Oxford: BSP Professional Books.
103. Purnell, P., *PhD Thesis*. 1998, Aston University, UK.
104. Hillig, W.B. and R.J. Charles. *Surfaces, stress-dependent surface reactions, and strength*. 1964.
105. Ritter Jr, J.E. and C.L. Sherburne, *Dynamic and static fatigue of silicate glasses*. 1971. **54**(12): p. 601-5.
106. Cain, J.J., et al., *The Effect of Hygrothermal Aging on Cylindrical E-glass/Epoxy Composites*, in *Southeastern Conference on Theoretical and Applied Mechanics XXIII*. 2005: Mayaguez, Puerto Rico.
107. Beddows, J., P. Purnell, and J.T. Mottram. *Application of GRC Accelerated Ageing Rationales to Pultruded Structural GRP*. in *Ninth International Conference on Fibre Reinforced Composites (FRC2002)*. 2002. University of Newcastle upon Tyne.
108. Helbling, C., et al., *Issues of variability and durability under synergistic exposure conditions related to advanced polymer composites in the civil infrastructure*. *Composites Part A: Applied Science and Manufacturing*, 2006. **37**(8): p. 1102-1110.
109. West, J.K. and L.L. Hench, *Silica fracture Part II A ring opening model via hydrolysis*. *Journal of Materials Science*, 1994. **29**: p. 5808-5816.
110. West, J.K. and L.L. Hench, *The effect of environment on silica fracture: vacuum, carbon monoxide, water and nitrogen*. *Philosophical Magazine A*, 1998. **77**(1): p. 85-113.

111. West, J.K. and S. Wallace, *Interactions of water with trisiloxane rings. II. Theoretical analysis*. Journal of Non-Crystalline Solids, 1993. **152**: p. 109-117.
112. Michalske, T.A. and B.B. C., *Slow Fracture Model Based on Strained Silicate Structures*. Journal of Applied Physics, 1984. **56**(10).
113. Dewar, M.J.S., et al., *AM1: A new general purpose quantum mechanical molecular model*. Journal of the American Chemical Society, 1985. **107**(13): p. 3902-9.
114. Walsh, T.R., M. Wilson, and A.P. Sutton, *Hydrolysis of the amorphous silica surface. II. Calculation of activation barriers and mechanisms*. Journal of Chemical Physics, 2000. **113**(20): p. 9191-9201.
115. Purnell, P. and J. Beddows, *Durability and simulated ageing of new matrix glass fibre reinforced concrete*. Cement and Concrete Composites, 2005. **27**: p. 875-884.
116. Orlowsky, J. and M. Raupach, *Modelling the loss in strength of AR-glass fibres in textile-reinforced concrete*. Materials and Structures, 2006. **39**: p. 635-643.
117. Helbling, C. and V.M. Karbhari. *Hygrothermal Degradation of E-glass/Vinyl ester Composites Under Sustained Load*. in *4th International SAMPE Symposium*. 2003. La Jolla, CA, USA.
118. Chu, W. and V.M. Karbhari, *Effect of Water Sorption on Performance of Pultruded E-Glass/Vinylester Composites*. Journal of Materials in Civil Engineering, 2005.